UNIVERSITY OF CALIFORNIA, SAN DIEGO

hIPSC-Derived Neurons with Familial Alzheimer's Disease Mutations Exhibit Altered Endocytosis, Transcytosis, and Axonal Transport

A dissertation submitted in partial satisfaction

of the requirements for the degree

Doctor of Philosophy

in

Biomedical Sciences

by

Sol M. Reyna

Committee in charge:

Professor Lawrence S.B. Goldstein, Chair
Professor Marilyn G. Farquhar
Professor Edward H. Koo
Professor Alysson R. Muotri
Professor Gene W. Yeo

2015

The Dissertation of Sol M. Reyna is approved, and it is acceptable in quality and form for publication on microfilm and electronically:

Chair

University of California, San Diego

2015

DEDICATION

Para mi familia.

EPIGRAPH

Siempre imagine que el paraíso sería algún tipo de biblioteca.

El futuro no es lo que va pasar, sino lo que vamos a hacer.

-Jorge Luis Borges

TABLE OF CONTENTS

LIST OF FIGURES

LIST OF TABLES

ACKNOWLEDGEMENTS

First and foremost, I'd like to thank Dr. Larry Goldstein for his support, expertise, and advice throughout my graduate studies. His encouragement and wisdom were instrumental and I cannot thank him enough. I am especially grateful for his consistent reminders to focus on the primary questions of my research and his (sometimes successful) attempts to help me avoid "mission creep". Larry has given me a degree of scientific freedom and independence that I had only hoped to experience. Thank you for your mentorship and for this extraordinary opportunity to pursue my scientific passions in the lab. In addition to Larry, I have to thank the members of my thesis committee: Marilyn Farquhar, Alysson Muotri, Gene Yeo, and Eddie Koo. I am deeply humbled and grateful to have learned from all of you. Thank you for listening to my (long-winded) presentations with patience and for your invaluable advice.

My experience in the Goldstein lab has been an incredible one and I am extremely aware that my success and happiness during graduate school is entirely due to the amazing people who work there. I cannot hope to accurately put into writing the depth of my gratitude, admiration, and affection for them all. Nevertheless, I would like to specifically acknowledge Dr. Grace Woodruff who joined the lab as a graduate student at the same time as I and has been a close friend, colleague, and collaborator throughout the long years. Grace, the collaboration with you has been one of the most important and meaningful

projects of my life and I am beyond grateful that we were able to work together on it. I don't think I would have made it through grad school without our FACS room meetings. I would also like to thank Dr. Angels Almenar for the supervision, advice, mentoring, and (not always) scientific conversations in our bay. I am constantly astonished by your inexhaustible patience, curiosity, and scientific accumen. Thank you for being my teacher.

To my labmates –John, Nidhi, Tami, Paulina, Lauren, Dan, Cheryl, Jess Young, Rik, Rodrigo, and, our adopted member, Jackie Ward– I could not have picked a better team. You are all fantastic people and my life has been made all the better for knowing you. To my students, Nina Kloss and Mariah Dunlap, you were just fantastic. I am still amazed you were able to understand my (meandering, think-out-loud) instructions and excel. I am so happy we were able to work together and I am so excited to see you grow and continue to pursue your own scientific passions.

My thesis work would not have been possible without the extraordinary accomplishments of previous students in the lab including Mason Israel, Emily Niederst, and Lukasz Spzankowski. Thank you for helping me when I was a fresh-faced, naïve first year.

And though it might seem impossible, there is life outside of lab and I want to thank my extraordinary friends for their support. Thanks to Karas, Joe,

Stephanie, Jenny, Kate, Corina, Kathryn, Emily, Jason, and Kevin. You are my lifeline.

Most importantly, I would like to thank my family for their love, support, and, above all, patience as I pursued my PhD. Papa y Mama, me enseñaron a ver el mundo con curiosidad y asombro, y yo se que todo lo bueno mío viene de ustedes. Minina, Jean-Marie, abuela Clara, y abuelo Luís, los quiero y extraño todos los días. Gracias por hacerme acordar de lo importante en la vida (familia, amor, y felicidad) y por tu consejo durante los anos. A mis primos, tíos, tías, y el resto de la familia, esto no podría ser posible sin ustedes. Que sigan queriendo, creciendo, y riendo. Finally, I want to thank my brother, Matias, who has been my sounding board and partner in crime for years. I am so excited to see how much you've grown and to watch you become an earnest, kind, and good man. I hope you always find joy in your pursuits and that you embrace all of your passions.

Chapter 1, in part, is a reprint of the following published manuscript. Goldstein, L.S.B., Reyna, S., and Woodruff, G. (2014). Probing the Secrets of Alzheimer's Disease Using Human-induced Pluripotent Stem Cell Technology. Neurotherapeutics 12, 121–125. The dissertation author was an author on this review.

Chapter 2 and 3 contain parts of a manuscript currently being prepared for submission. Reyna, S.M.* and Woodruff, G.*, Santos dos Chaves, R., Dunlap, M., Goldstein, L.S.B.. “Reduced Endocytosis and Transcytosis of APP and Lipoproteins Owing to Accumulation of β-CTF Fragments in Familial Alzheimer’s Disease Mutations.” The dissertation author was a co-primary investigator and author of this paper.

Chapter 4 and 5 contain parts of a manuscript currently being prepared for submission. Reyna, S.M.*, Woodruff, G., Weissmiller, A., Dunlap, M., Kloss, N., Goldstein, L.S.B. “Altered Axonal Transport of APP and Lysotracker Vesicles in $PS1^{\Delta E9}$ hIPSC-Derived Neurons.” The dissertation author was the primary investigator and author of this paper.

VITA

2009	Bachelor of Science in Biology, Brown University, Providence, RI
2015	Doctor of Philosophy in Biomedical Sciences, University of California, San Diego

Reyna, S.M.* and Woodruff, G.*, Santos dos Chaves, R., Dunlap, M., Goldstein, L.S.B.. Reduced Endocytosis and Transcytosis of APP and Lipoproteins Owing to Accumulation of β-CTF Fragments in Familial Alzheimer's Disease Mutations. (*in preparation*)

Reyna, S.M., Woodruff, G., dos Santos Chaves, R., Weissmiller, A.M., Dunlap, M., Kloss, N., Goldstein, L.S.B. Altered Axonal Transport of APP and Lysotracker Vesicles in $PS1^{\Delta E9}$ hIPSC-Derived Neurons. (*in preparation*)

Selfridge, A., Hyun, N., Chiang, C.-C., **Reyna, S.M.**, Weissmiller, A.M., Shi, L.Z., Preece, D., Mobley, W.C., and Berns, M.W. (2015). Rat embryonic hippocampus and induced pluripotent stem cell derived cultured neurons recover from laser-induced subaxotomy. Neurophotonics 2, 015006.

Niederst, E., **Reyna, S.**, and Goldstein, L.S.B. (2015). Axonal Amyloid Precursor Protein and its Fragments Undergo Somatodendritic Endocytosis and Processing. Mol. Biol. Cell.

Goldsein, L.S.B., **Reyna, S.M.**, and Woodruff, G. (2014). Probing the Secrets of Alzheimer's Disease Using Human-induced Pluripotent Stem Cell Technology. Neurotherapeutics 12, 121–125.

Weissmiller, A.M., Natera-Naranjo, O., **Reyna, S.M.**, Pearn, M.L., Zhao, X., Nguyen, P., Cheng, S., Goldstein, L.S.B., et al. (2015). A γ-Secretase Inhibitor, but Not a γ-Secretase Modulator, Induced Defects in BDNF Axonal Trafficking and Signaling: Evidence for a Role for APP. PLoS One *10*, e0118379.

Israel, M. a., Yuan, S.H., Bardy, C., **Reyna, S.M**., Mu, Y., Herrera, C., Hefferan, M.P., Van Gorp, S., Nazor, K.L., Boscolo, F.S., et al. (2012). Probing sporadic and familial Alzheimer's disease using induced pluripotent stem cells. Nature 482, 216–220.

ABSTRACT OF THE DISSERTATION

hIPSC-Derived Neurons with Familial Alzheimer's Disease Mutations Exhibit Altered Endocytosis, Transcytosis, and Axonal Transport

by

Sol M. Reyna

Doctor of Philosophy in Biomedical Sciences

University of California, San Diego, 2015

Professor Lawrence S.B. Goldstein, Chair

Alzheimer's Disease (AD) is a devastating neurodegenerative disease that currently affects more than 26 million people worldwide and is projected to triple

in prevalence by 2015. As such it represents an enormous economic, medical, scientific, and emotional burden on society. Despite extensive efforts, there is no cure and current treatments are only effective at ameloriating symptoms without delaying the progression of disease. Part of the challenge may stem from the use of model systems that incompletely recapitulate human disease. The recently discovered technology of human induced pluripotent stem cells (hIPSCS) has reinvigorated investigators and brought hope to the fields of AD. The power of hIPSC technology is the ability to capture the genomes of indivuals with complex genetic diseases in a pluripotent cell with the ability to become any one of the body. By driving hIPSC down a neuronal lineage, we can grow human neurons and model AD in a dish in the relevant cell type.

A hallmark of the polarized structure of a neuron is it long thin axon where a wide variety of cargo essential for proper neuronal viability must be transported correctly to and from the axon terminal. Perturbations of this complex neuronal process can have drastic consequences and, in fact, many neurological diseases are associated with defects in neuronals novel, neuron-specific sorting defects in hIPSC-derived neurons with familial AD mutations. Specifically, we see that toxic, intracellular accumulations of β-CTFs,proteolytic products of the amyloid precursor protein (APP), mediate decreased endocytosis and transcytosis of APP itself and lipoproteins. That this is a common phenotype of many fAD

mutations suggests that impaired axonal delivery of lipoproteins compromises synaptic maintenance in fAD.

In a specific fAD mutation, $PS1^{\Delta E9}$, we analyzed the complex axonal transport behavior of a number of AD-relevant cargo including APP, BACE1, Rab5a, mitochondria, and lysosomes. We report that $PS1^{\Delta E9}$ mutant neurons have enhanced anterograde transport of APP, possibly because of increased phosphorylated JIP1, while having no differences in Rab5a, BACE1, or mitochondrial transport behavior. Importantly, these transport changes accompanied by decreased density of axonal acidic vesicles and implicates impaired clearance of toxic axonal cargo in AD pathogenesis.

1. Introduction

Abstract

Our understanding of Alzheimer's disease (AD) is still incomplete and, as a result, we lack effective therapies. Reprogramming to generate human-induced pluripotent stem cells (hIPSC) provides a new approach to study human neurons that carry the genomes of people with familial or sporadic AD. Differentiation of hIPSCs to human neurons is already providing new insights into AD and molecular pathways that may provide new targets for effective therapy. These pathways include typical amyloid response pathways, as well as pathways leading from altered behavior of amyloid precursor protein to the elevated phosphorylation of tau protein, altered endocytosis, and even impaired cholesterol regulation. Although this type of investigation of AD using hIPSC-derived models is still relatively new, a number of informative and provocative reports have appeared in the literature thus far, with more soon to come. Current hIPSC-derived models of AD have capitalized on strongly genetic versions of familial AD (fAD), which represent less than 5% of all AD cases. To date, fAD mutations have only been identified in three genes: amyloid precursor protein (APP), presenilin (PS) 1, and PS2. In this thesis work, we further characterize hIPSC-derived neurons with fAD mutations, focusing on the $PS1^{\Delta E9}$ mutation, by looking at AD-relevant cellular pathways including 1) endocytosis, 2) recycling, 3) axonal transcytosis, 4) lysosomal function, and 5) axonal transport.

1.1 Background on hIPSC-Derived Models of AD

Alzheimer's Disease (AD) is a common, progressive neurodegenerative disease that affects more than 26 million people worldwide including 11% of those over 65 years of age and 32% of those over 85 (Fargo and Bleiler, 2014). As such, it represents a major public health, scientific, and medical challenge. The literature around this disease is enormous, currently including > 100,000 papers, based on a recent Pubmed search. The current major hypothesis in the field is the amyloid cascade model, which posits that oligomeric amyloid-beta (Aβ) fragments accumulate abnormally in patients with AD and drive neurotoxic events leading to neurodegeneration. While considerable evidence exists for the amyloid cascade model, experimental therapies built on this hypothesis have thus far been unsuccessful, and key details about how amyloid is neurotoxic either alone or in combination with other insults remain unclear (Golde et al., 2011).

One possible reason for our current situation may be that most mechanistic work thus far has relied either upon nonhuman animal models of AD or on experiments with human cells that are not actually neurons or glia. At present, no animal model appears to develop true AD and animal models often lack the range of phenotypes found in typical human AD. In fact, generating any of the Alzheimer's-type pathology found in humans generally requires expression of one or more human genes in a mouse genetic background. That human genes are required at all for the development of typical pathology raises doubt about the

scientific interpretation of the lesions mimicked by expression of human familial AD (fAD) genes and mutations in a mouse background.

Additionally, it is concerning that even when human genes are expressed in a mouse genetic background, not all human pathological features of AD are represented. For instance, second-generation AD mouse models develop Aβ plaques but fail to develop the characteristic neurofibrillary tangles (Balducci and Forloni, 2011; Braidy et al., 2012; Goldstein et al., 2014). Finally, no animal model truly mimics the most common form of AD, which is sporadic AD (sAD). sAD is known to be influenced by genetics (estimates indicate that as much as 60% of sAD is genetically-encoded (Ashford and Mortimer, 2002)), and numerous genetic risk factors have been identified from genome-wide association studies (GWAS) largely in non-coding regions (Bertram and Tanzi, 2009). If epigenetics and DNA regulation are driving risk factors for sAD, other animal models will be at best incomplete mimics of human behavior and at worse lead science down distracting and unrelated pathways.

One new opportunity that may provide insights into AD comes from recent advances in stem cell technology. In particular, reprogramming technology, which allows cells from patients with fAD or sAD to be reprogrammed to a pluripotent state to create human induced pluripotent stem cells (hIPSCs), is beginning to be of great value (Takahashi et al., 2007a). The power of hIPSC technology is the ability to capture the genome of a human in a cell that can become any one of the body. Thus, strongly genetic mutations responsible for

devastating neurological diseases can be immortalized, studied, and even corrected with new genome editing technologies. Importantly, hIPSCs, by definition, are pluripotent and can give rise to cell types from all three germ layers. Of particular interest to our lab is the capacity of hIPSC to differentiate down an ectoderm lineage and become a variety of cell types, such as neurons, astrocytes, oligodendrocytes, and other brain-derived cells. As these diverse cells carry the genomes of patients with AD, they can be used to test mechanisms of disease, to screen for potential drugs, and to evaluate functional roles of genetic variation observed in large GWAS studies. Furthermore, hIPSC technology allows investigators to identify and validate new pathways in the context of euploid human material in the absence of overexpression of key genes, which can bring its own artifacts.

Although this type of investigation of AD using hIPSC-derived models is still relatively new, a number of informative and provocative reports have appeared in the literature thus far, with more soon to come. Generally speaking, current hIPSC-derived models of AD have capitalized on strongly genetic versions of fAD. fAD represents less than 5% of all AD cases. To date, fAD mutations have only been identified in three genes: amyloid precursor protein (APP), presenilin (PS) 1, and PS2 (Tanzi and Bertram, 2005). These are autosomal dominant, highly penetrant mutations that result in early-onset AD in people as young as 30 years old (Leifer, 2003). hIPSC-based studies of AD have largely focused on demonstrating that hIPSC-derived neurons with fAD mutations

exhibit the characteristic and expected changes in APP processing, namely: elevated Aβ levels, altered Aβ42/40 ratios, increased APP CTFs, and alterations in phosphorylated Tau.

In this thesis work, we further characterize hIPSC-derived neurons with fAD mutations, focusing on the $PS1^{\Delta E9}$ mutation, by looking at AD-relevant cellular pathways including 1) endocytosis, 2) recycling, 3) axonal transcytosis, 4) lysosomal function, and 5) axonal transport.

1.2 PS1 and PS2 Mutations

Mutations in PS1 are the most common cause of fAD and over 100 pathogeic mutations have been reported all along the gene (Tanzi and Bertram, 2005). PS1 is a multipass transmembrane protein with multiple biological functions and forms the catalytic core of γ-secretase, which cleaves type 1 transmembrane proteins such as APP, Notch and cadherins (Edbauer et al., 2003). When APP is cleaved by γ-secretase down the amyloidogenic route, increased levels of intracellular APP CTFs (including toxic βCTFs) and extracellular secreted Aβ are generated. The amyloid cascade hypothesis of AD posits that elevated levels of Aβ drive neuropathology, but this hypothesis was modified with the identification of PS1 mutations that increase the proportion of the minor species of Aβ relative to the major one: Aβ42 vs Aβ40(Scheuner et al., 1996). Exactly how PS1 mutations drive fAD remains controversial in part because studies of PS1 mutations have largely relied on experimental

manipulations that overexpress PS1 and PS1 mutants in mouse and/or non-neuronal systems (Bentahir et al., 2006; Chávez‐Gutiérrez et al., 2012; Kumar-Singh et al., 2006). That being said, a number of common neuropathological features have emerged and its thought that PS1 and PS2 mutations function by altering intracellular sorting pathways, impairing lysosomal acidification and/or calcium levels, and/or modulating protein processing (Coen et al., 2012; Lee et al., 2010; Neely and Green, 2011; Nixon and Mcbrayer, 2013; Tarabal et al., 2001).

A number of papers have reported analysis of presenilin (PS) mutations. Mutations analyzed include $PS1^{A246E}$, $PS1^{A79V}$, and $PS2^{N141I}$ from patient material (Mertens et al., 2013; Sproul et al., 2014; Yagi et al., 2011). Previously in our lab, isogenic lines with the $PS1^{\Delta E9}$ mutation were generated by using TAL-effector nucleases (TALENs) to introduce the $PS1^{\Delta E9}$ mutation in the background of our celebrity scientist's, Craig Venter's, hIPSC line (Israel et al., 2012; Woodruff et al., 2013). The $PS1^{\Delta E9}$ mutation is a single point mutation that causes in-frame skipping of exon 9 and ablates the endoproteolytic site of PS1. Importantly, the Aβ42: Aβ40 ratio is increased in the $PS1^{\Delta E9}$ mutation as well as all of the other PS mutations currently in the literature. One study also reports significant gene expression changes in $PS1^{A246E}$ mutations (Sproul et al., 2014). Despite arguments in the literature that PS1 mutations are loss-of-function, Woodruff et al. 2013 carefully examined the various allelic combinations of $PS1^{null}$ and $PS1^{\Delta E9}$ mutant-bearing neurons and concluded that null mutations and fAD mutations

differed with respect to Aβ42 production and nicastrin maturation, and therefore that fAD PS1 mutations were not equivalent to null mutations.

1.3 APP Mutations

Several studies of hIPSC-derived human neurons carrying fAD APP mutations have appeared. The fAD APP mutations are present in 1 of the 2 genomic copies of APP, and are in the context of a “normal” euploid genome found in afflicted patients. Importantly, these mutations are in a normal APP gene in the absence of overexpression of amyloid precursor protein (APP) and with apparently normal genomic control of expression levels. Such studies have begun to provide new clues about early changes in neuronal physiology and function in response to mutations causing fAD.

One important study analyzed neurons made from hIPSC lines carrying fAD APPE693delta and fAD APPV717L mutations (Kondo et al., 2013). This work included an extensive analysis of Aβ production from these lines and found that APPE693delta made less total Aβ while APPV717L increased the Aβ42:Aβ40 ratio with the increased ratio due to an increase in Aβ42 and no change in Aβ40. They noted that APPE693delta cells accumulated Aβ oligomers inside the cell and exhibited signs of cellular stress that could be reversed by treatment with docosahexaenoic acid (DHA), a drug previously reported to attenuate endoplasmic reticulum stress or reactive oxygen species generation.

A second study (Israel et al., 2012), from our laboratory, analyzed a hereditary APP duplication (APPDp), which causes early-onset fAD. We took advantage of the ability to purify neurons by fluorescence-activated cell sorting and observed that the APPDp neurons produced and secreted more Aβ40, exhibited elevated signs of elevated glycogen synthase kinase 3β activity, and exhibited elevated phosphorylation of tau protein at threonine 231, a proposed pathological site in tau protein. Strikingly, the elevated phosphorylation of tau protein was inhibited by the application of β-secretase but not γ-secretase inhibitors, suggesting that in this human neuronal system, aberrant phosphorylation of tau protein is driven, at least in part, by the β-C-terminal fragment fragment of APP. We also observed an elevated frequency of enlarged endosomes similar to many previous reports of enlarged endosomes in non-neuronal cells caused by elevated expression of APP and by investigators studying postmortem brain material from Down syndrome fetuses, which carry an extra copy of APP by virtue of being trisomic for chromosome 21 (Cataldo et al., 2000, 2008). In an analogous study (Shi et al., 2012), Down syndrome neurons were differentiated to a cortical fate and analyzed for production and deposition of Aβ. The researchers found elevated production of both Aβ40 and Aβ42 in neurons derived from both Down syndrome embryonic stem and induced pluripotent stem cells. Taken together with the results from the PS fAD hIPSC studies, it becomes apparent that a common feature of fAD hIPSC-derived

neurons is elevated secretion of Aβ levels or Aβ42:40 ratios and, presumably, elevated intracellular APP CTF levels as well.

1.4 APP Processing and Toxicity of Fragments

Despite the known cytotoxicity of β-CTFs, and their equimolar relationship to Aβ, studies of this immediate precursor to Aβ are incomplete. In large part, understanding the disease-relevant roles of β-CTFs is limited by the use of model systems that incompletely recapitulate AD (Balducci and Forloni, 2011; Braidy et al., 2012; Goldstein et al., 2014). For this reason, we sought to use a human system that expressed endogenous levels of human fAD mutations in Presenilin 1 (PS1) and APP that cause increased levels of β-CTFs. Beyond the consensus that APP and PS1 fAD mutations alter APP processing, increasing Aβ42:40 ratio and β-CTF levels, there is little agreement in the field about how these mutations initiate pathogenic events that eventually lead to neurodegeneration. Previous work suggested that β-CTF accumulation might cause defects in lipoprotein internalization, but how general this defect might be and what cellular pathways might be dysregulated are not yet understood (Tamboli et al., 2011; Walter and van Echten-Deckert, 2013). There is also evidence for a toxic effect of elevated βCTF on protein sorting and axonal transport (Jin et al., 2002; Lu et al., 2000; Toyn and Ahlijanian, 2014; Weissmiller et al., 2015). For instance, mutations or treatments that increase βCTFs have been shown to drive axonal swellings in fAD APP^{SWE} mice (Tg-swAPP PrP) (Stokin et al., 2005, 2008), result in reduced

retrograde BDNF signaling (Weissmiller et al., 2015), and lead to organelle jams in axons (Gunawardena et al., 2013).

Further evidence that elevated APP CTFs could be pathological comes from the prominent drug failures of the γ-secretase inhibitors, Semagecestat and Avagacestat, both of which were terminated because of side effects, including worsened cognitive outcomes. This may be because γ-secretase inhibition, while reducing Aβ, also increases the levels of APP β-CTFs, which are known to have toxic effects and can severely impair neuronal function (Jin et al., 2002; Lu et al., 2000; Toyn and Ahlijanian, 2014; Weissmiller et al., 2015). Better drug candidates may be the class of β-secretase (BACE) inhibitors that seek to shift processing of APP to the α-secretase pathway and inhibit production of β-CTFs (C-terminal fragments) and Aβ. BACE as a clinical target is also attractive because mutations that enhance BACE activity (APP Swedish KM670/671NL) are strongly pathogenic, while the protective APP mutation A673T reduces BACE processing, consequently reducing Aβ and β-CTF production and lowering AD risk (Jonsson et al., 2012; Stamford and Strickland, 2013; Vassar et al., 2014).

Another intriguing possibility is that APP, through its C-terminal domain, acts as a cholesterol sensing protein (Beel et al., 2010; Song et al., 2013). There is ample evidence linking elevated cholesterol levels with increased association of APP and β-CTFs to lipid rafts thus favoring amyloidogenic processing of APP (Beel et al., 2010; Bodovitz and Klein, 1996; Guardia-Laguarta et al., 2010; Grimm et al., 2008; Kojro et al., 2001; Simons et al., 1998; Wahrle et al., 2002).

The finding that β-CTFs favors binding to cholesterol over homodimerization suggests that elevated levels of β-CTFs can drive retention of cholesterol in membrane-bound structures mimicking a cholesterol enriched state (Beel et al., 2010). This state could drive a negative feedback loop whereby high levels of APP or the proteolytic products of amyloidogenic APP processing, Aβ, β-CTFs, and AICD, downregulate intracellular cholesterol uptake, biosynthesis, and turnover (Pierrot et al., 2013). As we move forward, studying the effects of the proteolytic products of APP beyond Aβ will shed light on possible therapeutics and help us identify better drug candidates.

1.5 Endocytosis, Recycling, and Transcytosis in AD

Alterations in intracellular sorting and distribution of proteins are associated with a number of neurological diseases, including Alzheimer's Disease (Von Bartheld, 2004; Cataldo et al., 2000; Ginsberg et al., 2010; Karch and Goate, 2014; Lee et al., 2010; Maxfield, 2014). Additionally, unbiased screens have consistently identified regulators of endocytic trafficking as major risk factors for AD and endosome abnormalities are the earliest known disease-specific alterations in AD (Cataldo et al., 2000; Ginsberg et al., 2010; Treusch et al., 2011). Enlarged early endosomes have been reported in models of Down syndrome (DS) and APP duplications where an extra copy of APP drives a cascade of β-CTF-dependent endocytic dysfunction (Cataldo et al., 2000, 2008; Israel et al., 2012; Kim et al., 2015; Laifenfeld et al., 2007). Further support for a

role of altered endocytosis in AD is repeated data indicating that endosomes are highly active sites of APP processing. To produce Aβ, APP undergoes sequential cleavage by β-secretase (BACE1) and then γ-secretase along the endolysosomal route. BACE1 is localized primarily to the trans-Golgi network (TGN) and endosomes, but it's pH optimum for activity is acidic so it's thought that APP cleavage occurs predominantly in early and late secretory compartments (Dingwall, 2001; Hook et al., 2002). Increased association of APP and BACE1 in cholesterol-rich membrane domains, or lipid rafts, is thought to drive amyloidogenic processing of APP and enhanced Aβ secretion at the expense of surface, α-secretase-dependent, non-amyloidogenic, processing of APP (Reviewed in Beel et al., 2010). Thus, determining how sorting pathways drive altered localization and sorting of APP and its secretases is critically important for understanding AD pathogenesis.

Generally speaking, APP is thought to be synthesized in the ER and modified in the TGN. A small fraction of APP (~10%) reaches the plasma membrane through the secretory pathway where it can be internalized and targeted to the lysosome for degradation following classical degradative pathways or an even smaller proportion of APP can return to the cell surface through a recycling pathway (Marquez-Sterling et al., 1997). Evidence that impairments in the degradative pathway are important for AD pathogenesis abound with multiple reports linking APP and PS mutations to late endosome and lysosomal dysfunction. PS deficiency and mutations have been linked to

impaired acidification of lysosomes (Lee et al., 2010), calcium dysregulation (Coen et al., 2012; Nixon and Mcbrayer, 2013; Shen et al., 2012), and altered acidic vesicle distribution (Bezprozvanny, 2012). Furthermore, impairments in retrograde transport of lysosomes have been linked to impaired autophagosome/lysosomal maturation (Maday et al., 2012), delayed BACE1 degradation and, consequently, enhanced amyloidogenic processing of APP (Ye and Cai, 2014).

In the case of recycling-dependent sorting of APP, it's likely the classical recycling Rab GTPases Rab4 or Rab11 are playing an active role (Stein and Sussman, 1986; Verdi et al., 1999), though we are more inclined to believe that Rab11 is predominantly responsible for recycling of APP. First, Rab11 was identified as a regulator of β-amyloid production (Udayar et al., 2013), BACE1 colocalizes with Rab11 (Buggia-Prévot et al., 2014), increased colocalization of APP and Rab11 is associated with elevated Aβ production (Kyriazis et al., 2008). Though several important insights on the role of endocytosis in regulating APP processing and sorting has been done in non-polarized cell models, there is little known about the regulation of endocytic-dependent APP processing in the polarized cells of interest: neurons.

Neurons exhibit a highly polarized structure composed of a long, thin primary process called the axon and short, thick secondary processes called dendrites. In addition to "normal" endocytic sorting pathways seen in non-polarized cells, neurons are capable of transcytosis. The definition of transyctosis

refers to receptor-mediated ligand internalization at one side of the cell followed by release at the other end, with and without subsequent protein recycling (Kelly, 1993; Mostov and Simister, 1985). Numerous proteins are known to undergo transcytosis in neurons whether in anterograde (away from the soma toward the synapse) or retrograde direction (from the synapse to the soma) including including APP (Niederst et al., 2015), BACE1 (Buggia-Prévot et al., 2014), TrkA (Ascaño et al., 2009), L1/NgCAM (Wisco et al., 2003; Yap et al., 2008) and LDL/cholesterol (Karten et al., 2003). Of particular interest is the mechanistic similarities in soma-to-axon transcytosis of BACE1 and TrkA in Rab11-positive endosomes given the importance of BACE1-mediated APP processing in AD pathogenesis and the fact that TrkA-positive basal forebrain cholinergic neurons (BFCNs) are lost early in AD (Cattaneo and Calissano, 2012).

1.6 Axonal Transport in AD

A hallmark of the polarized structure of a neuron is its long thin axon where a wide variety of cargo essential for proper neuronal viability must be transported correctly to and from the axon terminal (Grafstein and Forman, 1980). Perturbations of this complex neuronal process can have drastic effects and, in fact, a number of neurological diseases are associated with transport defects, including AD (Chevalier-Larsen and Holzbaur, 2006; Stokin and Goldstein, 2006a, 2006b). Broadly speaking, axonal transport is driven by molecular motors that move on polarized microtubules in two directions.

Anterograde transport, toward the synapse, is mediated by a variety of plus-end directed kinesins (Goldstein and Yang, 2000; Hirokawa and Takemura, 2005). Conventional kinesin is a heterotetrametric protein composed of two heavy chains (KHC or KIF5) and light chain (KLC) subunits. The subunits can complex in various combinations to mediate the transport of a variety of cargo including lysosomes, mitochondria, endosomes, and even neurofilaments and tubulin (Gindhart et al., 1998). For example, kinesin-1C complexed to homodimers KLC has been shown to be the predominant molecular motor involved in fast axonal transport (FAT) of APP (Brunholz et al., 2012; Ferreira et al., 1992; Szodorai et al., 2009; Yamazaki et al., 1995). KIF1b has been shown to colocalize with mitochondria (Nangaku et al., 1994) and its absence is associated with abnormal perinuclear clustering of mitochondria (Tanaka et al., 1998), while KIF1a may be involved in axonal delivery of select synaptic vesicles (Okada et al., 1995). While studies of β-secretase (BACE1) (one of the secretases involved in APP processing) anterograde transport are few, there are indications that BACE1 anterograde delivery is regulated by a kinesin-1-dependent mechanism (Kamal et al., 2000; Steuble et al., 2012). In addition, transport of lysosomes and autophagosomes have been shown to depend on KLC1, kinesin-1B, and kinesin-2 (Rosa-Ferreira and Munro, 2011). The molecular motor for Rab5, which is associated with early endosomes, has long been elusive, but a recent studies indicate that kinesin-3 is likely the processive motor driving Rab5 motility (Huckaba et al., 2011; Schuster et al., 2011).

Minus-end transport away from the synapse and toward the cell body is termed retrograde axonal transport and is mediated by the cytoplasmic motor protein dynein. While there are 5 kinesins exhibiting different cargo specificity and variations in tissue expression, it is thought that dynein is the predominant retrograde motor. Dynein is composed of six subunits: dynein heavy chain (DHC), intermediate chain (DIC), light-intermediate chain (DLIC), and 3 dynein light chains (DLC). Each subunit of dynein is capable of multiple protein-protein interactions and, in addition, dynein requires an 11-subunit protein complex called dynactin for proper processive movement and helps dynein bind to more proteins (King and Schroer, 2000; Pfister et al., 2006; Schroer, 2004). Some of the axonally transported cargo that require dynein include APP, lysosomes, mitochondria, Rab5, and BACE1.

There is strong evidence that axonal transport defects are important in AD including observations of defects in neurotrophic signaling independent of Aβ (Salehi et al., 2006), axonal traffic jams (Stokin et al., 2005), microtubule destabilization as a result of abnormally phosphorylated Tau (Baas and Qiang, 2005; Mandelkow et al., 2004; Noble et al., 2013), and reduced motor levels in frontal cortex of AD patients (Morel et al., 2012). Furthermore, impaired axonal transport of mitochondria (Reddy, 2011), autophagosomes (Lee et al., 2010; Neely and Green, 2011; Sanchez-Varo et al., 2012), lysosomes (Ye and Cai, 2014), early endosomes (Kim et al., 2015), BDNF (Weissmiller et al., 2015), and APP (Brunholz et al., 2012; Gandy et al., 2007; Gunawardena et al., 2013; Reis

et al., 2012; Stokin et al., 2005, 2008; Szodorai et al., 2009; Vagnoni et al., 2012) are implicated in AD. Hidden in the data is the implication that elevation of APP βCTFs might be the relevant factor driving impairments in axonal transport possibly because of differential affinity to motors. Thus, there is developing interest in using pharmaceutical compounds that can modulate motor activity and function to rescue AD transport defects. hIPSC-derived neurons can provide a human system to conduct drug screens for compounds involved in regulating axonal transport mechanisms.

1.7 Final Thoughts

Although the use of hIPSC technology is still in its infancy, early reports thus far have raised the possibility that this system may provide unique advantages for the discovery of factors that cause AD and how these factors respond to genetic or pharmacologic manipulation. One obvious possibility is that the generation of neurons carrying various fAD mutations or sAD genomes will provide a uniquely human neuronal system for the evaluation of potential therapeutic interventions. Early work has been valuable at understanding pathways in fAD neurons.

A unique opportunity of the hIPSC system is the ability to probe how complex human genomic architectures predispose patients to AD and how they influence the behavior of various, participating cell types. In this regard, the reports that some genomes found in patients with sAD also generate ***in vitro***

culture phenotypes similar to those found in fAD mutations provides a striking example of how this may proceed. Thus, there is enormous promise in the utility of a human neuronal culture system to predict how individual genetic and cellular phenotypic variation contributes to response to pharmacological intervention at clinically relevant levels. Finally, the genetic technologies available with hIPSC may allow the deciphering of how complex genomic architectures found in individual humans act together to generate susceptibility and variation in response to the environmental factors that may also contribute to, or pharmacologically modify, AD phenotypes in patients.

1.8 Acknowledgements

Chapter 1, in part, is a reprint of the following published manuscript. Goldstein, L.S.B., Reyna, S., and Woodruff, G. (2014). Probing the Secrets of Alzheimer's Disease Using Human-induced Pluripotent Stem Cell Technology. *Neurotherapeutics* 12, 121–125. The dissertation author was an author on this review.

2. Semi-Automated, Quantitative Approaches to Fluorescent Image Analysis

Abstract

Alterations in intracellular sorting and distribution of proteins are associated with a number of neurological diseases, including Alzheimer's Disease. Fluorescent microscopy is widely used to analyze endosomal dynamics, protein trafficking, and sorting machinery in cells. Quantitative methods to analyze fluorescent images, however, are prone to experimenter bias and are often time-consuming and labor-intensive. To facilitate analysis of large data sets, a series of semi-automated, quantitative scripts were developed. This chapter is a detailed description of the most commonly used image analysis programs developed as part of this thesis work. Of particular note is the development of an automated segmentation program to identify neuronal soma and automatically measure their intensity, count puncta, and colocalization of multiple channels. More specialized programs were generated to measure lysosomal pH and calcium. Because neurons have highly polarized structures, robust quantification of axonal puncta intensities and densities is necessary. To that end, a series of programs were generated to measure puncta density, puncta intensities, and percent colocalization in defined axonal regions of interest. By using semi-automated, quantitative programs, robust analysis of large data sets can be done rapidly and with minimal experimenter effort.

2.1 Introduction

Alterations in intracellular sorting and distribution of proteins are associated with a number of neurological diseases, including Alzheimer's Disease(Von Bartheld, 2004; Cataldo et al., 2000; Ginsberg et al., 2010; Karch and Goate, 2014; Lee et al., 2010; Maxfield, 2014). In fact, unbiased screens have consistently identified regulators of endocytic trafficking as major risk factors for AD (Ginsberg et al., 2010; Treusch et al., 2011). Fluorescent microscopy is widely used to analyze endosomal dynamics, protein trafficking, and sorting machinery in cells. Quantitative methods to analyze fluorescent images, however, are prone to experimenter bias and are often time-consuming and labor-intensive. ImageJ, for example, is frequently used to quantify immunohistochemical labeling, localization of fluorescent fusion proteins, spectral-imaging from multi-label tissue sections, and images collected by confocal microscopy (Hartig, 2013). While a number of ImageJ plugins exist to help facilitate quantification, many of them can only be used on one image at a time. Additionally, current methods largely involve the experimenter manually choosing individual regions of interest (ROIs) corresponding to individual cells and can introduce confirmation bias.

Currently, several labs have sought to validate human induced pluripotent stem cell (hIPSC)-derived neuronal models of Alzheimer's Disease (AD) by looking at strongly genetic forms of familial AD (fAD) (Reviewed in Cao et al., 2014; Goldstein et al., 2014). For the most part, fAD studies of AD have

recapitulated the results seen in mouse systems overexpressing mutated forms of the presenilin (PS) genes and amyloid precursor protein (APP). Namely, enhanced amyloidogenic processing of APP including increased Aβ levels, increased Aβ42:40 ratio, enlarged early endosomes, and occasionally increased phosphorylated Tau (Spires-Jones and Hyman, 2014). In the few studies looking at sporadic AD (sAD), there seems to be a larger degree of variability such that only one of two hIPSC-derived neuronal samples exhibited the expected AD-associated phenotypes (Israel et al., 2012; Kondo et al., 2013; Young et al., 2015)

As the field moves forward and seeks to study more complex phenotypes, quantitative methods will have to take into account the variability exhibited in sAD samples and the expectation of weak phenotypes even in fAD samples. Given the established role of endocytic sorting in driving AD phenotypes, fluorescent microscopy and quantification of small puncta will be necessary. To that end, a series of computer-assisted ImageJ and Matlab programs were developed to automate ROI detection, count puncta, and measure colocalization in both soma and axons. Additionally, a few more specialized programs were developed to quantify lysosomal pH and calcium signaling in neural progenitor cells (NPCs) and neurons. The goal from these programs was to minimize experimenter handling of the images, to batch large data sets, and to maximize data output. Importantly, by using computer-assisted analysis, every data set was subject to

the same selection criteria and this allowed for robust quantification of small phenotypic differences (Goldstein et al., 2014; Young and Goldstein, 2012).

2.2 Results

2.2.1 ImageJ Method for Automated Detection of Soma

Previous publications from our lab indicated that hIPSC-derived lines exhibit phenotypic variability between clones derived from the same patient and/or between differentiations (Israel et al., 2012; Woodruff et al., 2013; Young et al., 2015). In particular, microscopy-based assays exhibited a lot of variation and were difficult to consistently replicate. As mentioned in the introduction, at least part of this was likely due to experimenter bias in selecting cell soma and underpowered data sets. Because it was extremely time-consuming to manually select the hundreds of soma needed to accurately power a fluorescent study, an ImageJ program to automatically identify cell soma was written.

First, neurons were stained with the established somatodendritic marker, Map2, to allow for delineation of soma borders. Because most primary antibodies are derived in mouse or rabbit, we chose a chicken anti-Map2 primary antibody and used the Dylight 405 donkey anti-chicken IgY secondary antibody (Jackson ImmunoResearch, 703-475-155). This way, the quantitative 488, 568, and 647 channels were left open for staining with other primary antibodies. To facilitate handling of large imaging data sets, multi-channel images were kept in an Lsm5 file format. This is a lossless file format that keeps metadata information,

including pixel scale information and acquisition settings. Because channels are stored as separate slices in an Lsm5 file, a small script was used to split, rename, and organize images into subfolders. The script **Split Channels** inputs Lsm5 files and then renames the channels as “C1-“ plus original file name. The important part of this script is that it generates a separate folder of Map2 labeled images.

This folder consisting of images labeled with the blue Map2 channel is the parent directory used to delineate and identify soma borders **(Figure 2-1A, first inset)**. At this point, built-in ImageJ commands were programmed into the **SomatoDendrite_ROI** script to automatically identify soma and make ROIs zip files. Essentially, images are thresholded by intensity to create a black and white binary image (**Figure 2-1A, second inset**). Because cell borders can look like large merged objects, the built-in ImageJ command **Watershed** was used to separate merged objects using flooding simulations as described by Vincent and Soille, 1991. From there, the built-in ImageJ plugin **Analyze Particles**, which identifies white objects from a black and white mask image based on size, was used to identify soma. Soma sizes were limited to 50-200 um^2, which was a size range that included most neuronal soma while excluding small circular structures corresponding to dead cells and large, flat structures likely corresponding to glial or neural progenitor cell contaminants.

The script generates a number of output files including a folder of the binary mask images used to identify neuronal soma and a folder of zip files

corresponding to the soma ROIs identified with **Analyze Particles** in each image. Using this script, hundreds of neuronal soma can be automatically identified from a large series of images. (See Appendix)

2.2.2 ImageJ Methods for Intensity, Puncta, and Colocalization Analysis

The ROI zip files can then be used to quantify a number of quantitative microscopy parameters such as soma intensity, puncta count, and colocalization of two channels. To quantify fluorescent soma intensity, a parent directory corresponding to the quantitative channel in question and a ROI directory corresponding to the ROI zip files generated with **SomatoDendriteROI** is inputted into the **MeasureIntensityinROI** script. An output text file is generated for each image with individual soma data including soma area, mean soma intensity, standard deviation of soma intensity, and min and max intensity values **(Figure 2-1D)**. In a similar manner, puncta counts can also be automatically generated, when appropriate. Puncta images are inputted into the **PunctainROIAnalysis** script and processed for to binary images with puncta outlined. The processing includes the built-in ImageJ Subtract Background command, which removes smooth continuous background using a rolling ball algorithm. This “cleans up” hazy fluorescence attributed to imaging artifacts or, as with Rab stains, diffuse cytoplasmic staining. Images are then converted to 8-bit, thresholded, and watershed to separate merged puncta. The thresholding

step can be manually adjusted to account for staining patterns of different proteins. An example of the binary mask image is depicted in **Figure 2-1B.**

The script then uses the binary image in combination with the Analyze Particles command to identify puncta 0.1-20 um^2 in size within each soma, identified with **SomatoDendrite_ROI**. For some applications, knowing the individual puncta intensity is necessary, thus the program also includes a step where it takes the puncta ROIs and measures the intensity of each individual puncta in the original, unprocessed channel image. The program outputs a number of files including a copy of each image's black and white mask, a zip file containing the puncta ROIs, and two summary text files. The Puncta_Summary text file contains soma puncta counts, total area of puncta per soma ROI, average size of puncta per soma, and total percent area of puncta per soma ROI **(Figure 2-1C).** Puncta_Results text file includes individual puncta data including size, intensity values, and xy-coordinates **(Figure 2-1C)**. From this program, automated quantification of puncta counts in hundreds of neuronal soma and analysis of thousands of puncta intensities and sizes can be done automatically and with minimal user handling.

For some experiments, it was necessary to measure colocalization of two different dyes or stains. To quantify colocalization, a modified version of the ROI segmentation program was used. **Overlap_counts_in_ROI** uses the binary masks created from **PunctainROIAnalysis** and the soma ROIs generated from **SomatoDendriteROI** to measure overlap between two channels binary images.

ImageJ has a feature called Image Calculator that performs arithmetic and logical operations between two binary images. One of the mathematical operations is the “AND” feature, which finds the locations where two input images intersect (i.e. img = img1∧img2) (**Figure 2-2A**). The program then counts the number of overlapping puncta within each individual ROI (**Figure 2-2B**). Colocalization percentages can be determined by taking the number of overlapping puncta over the total number of Ch1 puncta or the total number of Ch2 puncta. Additional data include total area, average size, and percent area of the ROI for the overlapped puncta.

2.2.3 Lysosomal pH and Calcium Measurements

There have been numerous reports concerning the role of PS1 and PS2 in regulation of lysosomal pH and calcium levels (reviewed in Bezprozvanny, 2012; Nixon and Mcbrayer, 2013). Because we are interested in studying the phenotypic effects of fAD mutations in hIPSC-derived neurons, we decided to develop a microscopy-based platform to study lysosomal pH and calcium. There are a number of fluorescent probes that can be used to qualitatively evaluate lysosomal pH (reviewed in Wolfe et al., 2013). Unfortunately, we did not have a microscope capable of visualizing Lysosensor Yellow/Blue-Dextran, which is excited with a 384 nm wavelength. Though we were able to measure lysosomal pH by plate reader with this dye (see **Figure 3-8A**), we were concerned that the resolution of a plate reader was not powerful enough to detect small differences

in hIPSC-derived neural progenitor cells and neurons. Therefore, we chose to employ Invitrogen's Fluorescein and Tetramethylrhodamine dual conjugated Dextran (D-1951). This ratiometric probe contains the pH-insensitive fluorophore, Tetramethylrhodamine, which is excited by the 568nm laser, and the pH-sensitive fluorophore, fluorescein, which is excited by the 488nm laser. This probe takes advantage of the pH sensitivity of fluorescein, which is known to quench at low acidities with an optimal pH range of 5-8 (Geisow, 1984; Ohkuma and Poole, 1978).

In order to label lysosomes, we took advantage of the properties of Dextrans. Dextrans are hydrophilic polysaccharides synthesized by *Leuconostoc* bacteria that serve as valuable, fluid-phase markers for the cellular uptake and internalization of exogenous materials by endocytosis. To label lysosomes with dextrans, cells are incubated for 4-6 hours in dextran (to allow for sufficiently bright labeling of the endocytic compartments), followed by at least a 12-hour chase. This chasing period ensures the dextran conjugates have enough time to accumulate in lysosomes. As evidence in **Figure 2-3A,** by using this protocol greater than 95% of, in this case, alexa-488 dextran puncta colocalize with the established lysosomal dye, Lysotracker DND-99.

To measure lysosomal pH, cells were incubated in this manner with Dextran Fluorescein-TetramethylRhodamine (Fl-TMR). All lysosomal pH measurements had to be done with live cells so it was critical to maximize speed of image acquisition and minimize the amount of time that cells were kept

outside. Cells were plated in glass-bottom, black 96-well plates and kept at 37°C with 5% CO_2 to simulate incubator conditions. Images were acquired on a confocal microscope with a water-based 40x objective with digital zoom. A second 96-well plate with only control cells was used to generate a standard pH curve. Essentially, media was removed from individual wells and 100µl of pH standard buffers were added, as previously described with modifications (Diwu et al., 1999; Lee et al., 2010). pH buffers ranged from 3.6 to 7.0 and were spaced at 0.2 pH intervals. Lysosomal pH visibly changed immediately, with fluorescein quenching at low pHs and increasing dramatically in intensity at high pHs (as expected) (**Figure 2-3D**). At least three images per well were acquired, capturing red, green, and bright field channels simultaneously.

For quantification, an image segmentation program was used called **pHAnalysis_Fluorescein_TMR** (See **Appendix**). Since TMR is a pH-insensitive dye, a Mask and ROIs corresponding to dextran-positive lysosomes were identified based on TMR staining (**Figure 2-3B**). At this point, intensities in lysosomal ROIs were measured in the green and red channels. For quantification, the ratio of fluorescein to TMR was calculated for each individual lysosome and the mean of those values per image was considered a biological replicate. The mean of the mean of the wells was then plotted on an S-curve in Prism using the pH standard curve. A separate 96-well plate with experimental wells was used second and captured the same way. All images were captured within 15 minutes to minimize alkanization of the lysosomes. Values from

experimental wells were then plotted on the calculated S-curve to determine final pH values. Ammonium chloride (NH_4Cl) was used as a positive control that deacidifies the lysosome (Hart, 1991). Using this method, $PS1^{wt/wt}$ lysosomes had an average pH of ~5.3, and NH_4Cl treated lysosomes had an average pH of ~6.8 (**Figure 2-3C**). Using this method, thousands of lysosomes can be rapidly quantified for pH in an unbiased and rapid assay.

To measure lysosomal calcium a different approach was used, rather than dextran. Standard calcium indicators in the literature are the Fluo and Fura dyes, available through Life Technologies. Fluo-4 is a newer version of the original Fluo-3 dye, developed by Roger Tsien and colleagues in 1989 (Akwasaki Minta, 1989). The AM dye is a cell permeant compound that binds to cytosolice free Ca^{2+} and fluoresces more brightly with increasing concentrations of Ca^{2+}. Fluo-4 AM is excited by standard 488 lasers and emits in the green channel. Fura Red, a Fura-2 analog, is an intracellular calcium indicator with unique properties. It's often used a ratiometric indicator of Ca^{2+}-free and Ca^{2+}-bound intracellular calcium pools. When excited at 450-500 nm, it emits at long wavelengths, ~633 nm, and actually *decreases* in intensity as calcium levels increase. By simultaneously labeling cells with Fluo-4 and Fura Red, investigators are able to determine relative intracellular Ca^{2+} levels with a ratiometric assay. Essentially, cells are incubated for 30-60 min (longer incubations are necessary to fully label neurons as opposed to neural progenitor cells or glia) and excited with the 488 laser. Light from emission wavelengths at ~500 and ~650 are simultaneously

acquired and the intensity ratio of 500/650 is a measure of relative calcium intensity.

In this manner, relative basal Ca^{2+} levels can be determined be generating ROIs around cell bodies and measuring intensity (**Figure 2-4A**). Additionally, Ca^{2+} from intracellular structures can be indirectly measured as a fold change from baseline after treatment with select drug compounds. For instance, lysosomal calcium can be measured by exposing cells to 600μM of GPN (glycyl-L-phenylalanine 2-naphthylamide), a Cathepsin C substrate that induces osmotic lysis of lysosomes, and endoplasmic reticulum (ER) Ca^{2+} can be measured by exposing neurons to 4μM of ionomycin, an ionophore that induces pore formation from Ca^{2+} permeable membranes resulting in complete emptying of ER Ca^{2+} store, as previously described (Akwasaki Minta, 1989; Lloyd-Evans et al., 2008; Shen et al., 2012).

To ensure consistency, cells are plated in 24 well imaging plates with an imaging volume of 400μl of phenol-free NPC-B. The imaging time is set to 180 cycles (or approximately 3 min) and 100μl of NPC-B is added at cycle 10 to estimate background intensity from addition of media alone. At cycle 60, 100μl of 600μM GPN is added, making the final concentration of GPN a consistent 100μM. As evidence by **Figure 2-4**, addition of NPC-B at cycle 10 has minimal effects on calcium intensity but GPN addition at cycle 60 clearly increases the Fluo-4/Fura Red ratio to approximately 1.2 times the basal levels. Finally, to saturate calcium signal, 200μl of 4μM ionomycin is added at cycle 120, which

leads to rapid increases in the Ca^{2+} ratio. Overall, the approach allows investigators to measure lysosomal Ca^{2+} and infer ER Ca^{2+}. To facilitate quantification, an ImageJ program in combination with an Excel template was used to rapidly analyze data.

Because cells can move after exogenous addition of media, ROIs were generated from the **MaximumIntensityProjection** of the movie stack. Thus, even is a cell moves 5-10um, for example, the ROI will cover the entire area where a cell was located (**Figure 2-4A** "Max" inset). The **Calcium** program (see **Appendix**), measures mean cell intensity in the Fluo-4 channel and Fura Red channels per cell per slice of time. By pasting Fluo4 text file into cell **A1** in the template of each Excel file and pasting the Fura Red text file into cell **A182**, the template can automatically determine average fold difference including SEM and n for all cells in a movie (cells **E553:G732**) and can even bin together 10 time points to generate a smaller data set (cells **U553:W588**). To compare multiple movies, a separate "Summary" sheet exists. Simply name each sheet with a unique identifier and then manually write the names of the sheet into the indicated space in the "Summary" sheet. Results will be updated automatically. Again, the combined utility of an ImageJ program and Excel template provides consistent and reproducible measurements of Ca^{2+} levels in real-time with minimal experimenter effort. An example trace of the results from multiple experiments across >50 cells and 3 experiments is depicted in **Figure 2-4B**.

2.2.4 Matlab Methods for Axonal Puncta Quantification

For some applications, quantification of axonal puncta counts is necessary. While the ImageJ programs developed above could theoretically be adapted for axonal analysis, they would not take into account the complex case of partially overlapping, diffraction-limited spots. When the resolution limit exceeds the distance separating two labeled-proteins, the superposition of the channel images creates a single local maximum. In fact, current automatic detection and localization methods fail to take into account the limitations of diffraction-limited data (Anthony and Granick, 2009; Bornfleth et al., 1999; Cheezum et al., 2001; van den Doel et al., 1998; Goulian and Simon, 2000; Jaqaman et al., 2008; Kubitscheck et al., 2000). From previous work in the lab, we had a Matlab-based program that made use of a Gaussian fitting algorithm to identify punctate features in an axon (Jaqaman et al., 2008; Reis et al., 2012; Szpankowski et al., 2012; Thomann et al., 2002)**.** Briefly, the algorithm scans an unprocessed, undeconvolved image and marks intensity maxima positions, while accounting for local background. The program then iteratively fits one or multiple Gaussian functions onto each local maxima “seed” and estimates the point source location for each acquired Gaussian amplitude (Jaqaman et al., 2008). An example of the Gaussian Fitted file is depicted in the second inset of **Figure 2-5A** where the point source of detected maxima are indicated by pink dots.

A script was previously developed to quantify individual puncta intensities and colocalization of multiple channels in an axon of a single image (Encalada et

al., 2011). Given the large number of images and axons that we needed to evaluate for precise quantification of axonal dynamics in hIPSC-derived neurons, individually evaluating single images would have been prohibitively time-consuming. Thus, the previous programs were adapted to batch process multiple images at once. First, a new script to make and store axonal ROIs was developed. Gaussian fitted images are saved in sequential order as tif files (Ex. IMG_001.tif). The root name or **FNAME** (ex. IMG_) is identified in **Sol_MakeROIs_v1** and the first image number (**NS**) and last image number (**NE**) are defined in three digit format. Finally, an output file name is chosen by the user (ex. ROI.mat). By starting the program, individual images appear in order and the user must manually identify axons using the built-in polygon ROI feature in matlab (**Figure 2-5A, ROI**). After all image ROIs are identified, the program closes and generates an output Mat file with the ROI information stored. ROIs are stored as a binary file format in RESULTS and, coordinates of the polygon vertices are stored in x and y (**Figure 2-5B**). (See Appendix for script of **Sol_MakeROIs_v1** and **Sol_MakeROIs_Program**)

From the stored ROI file, many features could be automatically analyzed and adjusted easily without having to manually select axonal ROIs every time. As an additional bonus, the generation of polygon ROIs provided a surrogate measure of axonal length. By using a series of Matlab commands to convert the polygon vertices x-y coordinates to a vector format, the maximum distance or perimeter of the polygon can be determined. Since the polygon surrounds the

axon twice, an estimate of the axon length can be determined by halving the perimeter distance determined by the trace feature. Thus:

```
for RPT=1:length(RESULT);
   fprintf('Processing IMG %d of %d\n',RPT,length(RESULT))
%%%%%%% AXON LENGTH %%%%%%%%%
      D1 = [x{RPT},y{RPT}];
      S = squareform(pdist(D1));
      d = length(S);
      S = S(1:d-1,2:d);
      AXL = (trace(S)/2000)*PXLSCL;
```

Where **trace(S)** is the polygon perimeter and **AXL** is the final axon length, corrected by the pixel scale (**PXLSCL**). (See Appendix, **Sol_THREE_Density**)

Importantly, by obtaining the axonal distance, density measurements for each quantified channel can be determined. Thus the number of features that exceed a pre-determined threshold value (**ONETHRES**, **TWOTHRES**, **THREETHRES**) are counted and then normalized to axon length to determine count per micron or axonal puncta density. An automated program to count densities of up to three channels in a given data set was written and is available in the Appendix, **Sol_THREE_Density**. An example of the output text file is seen in **Figure 2-5C, Density Output.**

To measure colocalization of proteins labeled with different fluorophores, a cutoff for colocalization was set to 300nm as previously reported(Encalada et al., 2011; Szpankowski et al., 2012). This was sufficient to identify unique features without overcounting features in close proximity. Again, the previous program was time-consuming in that it could only analyze one image at a time so the

program was adjusted to batch process multiple images at once. The ROI.mat file, corresponding to the axon ROIs, is loaded into the program, and up to three channels can be quantified for colocalization. The program is not qualitatively different from the previously published one, but allows for batch analysis of many axon images at once. An example output file is depicted in **Figure 2-5D** where the “seed” channel is Ch1. Essentially, channel 1 images act as the “seed” and then colocalization of Ch2 and Ch3 on Ch1 are measured. Ch1 puncta that overlap with Ch2 or Ch3 within 300nm will be counted with a 1. If not overlap is detected, a 0 is indicated. If both channels overlap, a 1 is indicated in the BOTH column. Amplitudes of all Ch1 puncta and overlapped Ch2 and Ch3 amplitudes are depicted in the last three columns. A summary text file with percent overlap values for each axonal ROI is also generated (not shown).

The combination of the Matlab programs allows for robust analysis of axonal puncta density, puncta intensities, and percent colocalization of many axonal proteins in a high-throughput and efficient manner. By saving the ROI files, robust manipulation of the data sets can be done rapidly and with minimal experimenter effort.

2.3 Discussion

Overall, this chapter is a detailed description of the most commonly used image analysis programs developed as part of this thesis work. The biggest benefit to the programs is the automated detection and analysis of soma ROIs

and puncta ROIs. To date, most experimenters use hand-drawn selection of soma ROIs and manually count puncta within cells. This method of image analysis is not only labor intensive, but can introduce confirmation bias and mask effects. With the advent of iPSC modeling of sporadic genetic diseases, imaging methods have to be robust enough to detect small differences in large data sets.

2.4 Acknowledgements

Chapter 2 contains parts of a manuscript currently being prepared for submission. Reyna, S.M.* and Woodruff, G.*, Santos dos Chaves, R., Dunlap, M., Goldstein, L.S.B.. “Reduced Endocytosis and Transcytosis of APP and Lipoproteins Owing to Accumulation of β-CTF Fragments in Familial Alzheimer’s Disease Mutations.” The dissertation author was a co-primary investigator and author of this paper.

A

SomatoDendrite_ROI

Map2 B/W Mask ROIs

B

PunctaInROIAnalysis

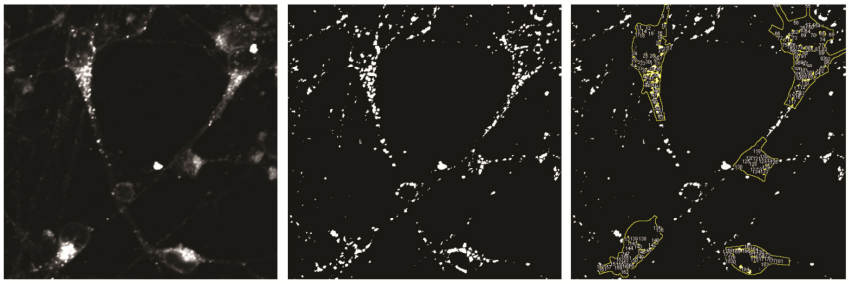

Puncta Stain (LDL) B/W Puncta Mask Puncta ROIs

C

Text File Name: Puncta_Summary

Slice	Count	TotalArea	AverageSize	%Area
Rd_IB7_A1_001.tif	2	2.7574	1.3787	0.9185
Rd_IB7_A1_001.tif	6	3.9637	0.6606	1.1429
Rd_IB7_A1_001.tif	4	1.7234	0.4308	0.9268
Rd_IB7_A1_001.tif	2	3.1882	1.5941	2.4899
Rd_IB7_A1_002.tif	22	28.1768	1.2808	6.7920
Rd_IB7_A1_003.tif	12	13.0544	1.0879	6.9591
Rd_IB7_A1_003.tif	13	12.6236	0.9710	4.6222

Text File Name: Puncta_Results

PunctaID	Size	Intensity	StDev	Min	Max	x	y
Rd_IB7_A1_001.tif:0001-0225	2.4127	32039.4464	18490.6674	8287	65535	25.4158	46.7803
Rd_IB7_A1_001.tif:0002-0227	0.3447	15470.8750	3919.3119	10840	21773	28.5663	47.2473
Rd_IB7_A1_001.tif:0003-0156	0.3447	16818.8750	4360.1810	9800	22600	59.7013	32.4582
Rd_IB7_A1_001.tif:0004-0176	0.7324	23555	2108.9892	19190	27079	57.6730	36.6233
Rd_IB7_A1_001.tif:0005-0185	0.7324	19023.4118	2176.7977	15592	22683	43.1433	38.3937
Rd_IB7_A1_001.tif:0006-0197	1.2494	22825.4483	2106.1480	17677	27271	48.0087	40.9586
Rd_IB7_A1_001.tif:0007-0206	0.1293	17189	1666.7102	16083	19106	50.4041	42.7933

D

Text File Name: Rd_IB7_A_001.tif_ROIIntensity

Soma ID	Area	Mean	StDev	Min	Max
Rd_IB7_A_001.tif:2963-0034	121.7980	4515.0534	4429.0481	16	21038
Rd_IB7_A_001.tif:2964-0054	267.8953	3695.6052	5601.8429	20	65535
Rd_IB7_A_001.tif:2965-0192	105.0815	4434.5158	4664.2077	9	43447
Rd_IB7_A_001.tif:2966-0244	168.3285	3207.6783	3304.9807	15	19479
Rd_IB7_A_001.tif:2967-0331	189.0088	3559.1828	3033.5720	17	21541
Rd_IB7_A_001.tif:2968-0437	127.7005	3752.1167	3586.7898	17	21636

Figure 2-1 Automated Detection and Analysis of Map2-Positive Soma

A) Purified hIPSC-derived neurons are stained with the somatodendritic marker Map2 and thresholded using intensity to generate a binary mask image. ROIs are automatically identified by the script SomatoDendrite_ROI. B) Further analysis can be done on a parallel quantification channel to count puncta and quantify puncta area. An example of puncta staining for LDL is depicted in the first field. Automatic ImageJ thresholding allows for robust detection of many puncta within the soma ROIs identified in 2.1.A. C) Example text files of the puncta counts per soma (Puncta_Summary) as well as individual puncta data including size and intensity (Puncta_Results). D) An example text file of soma intensity measurements obtained from the MeasureIntensityinROI script.

A

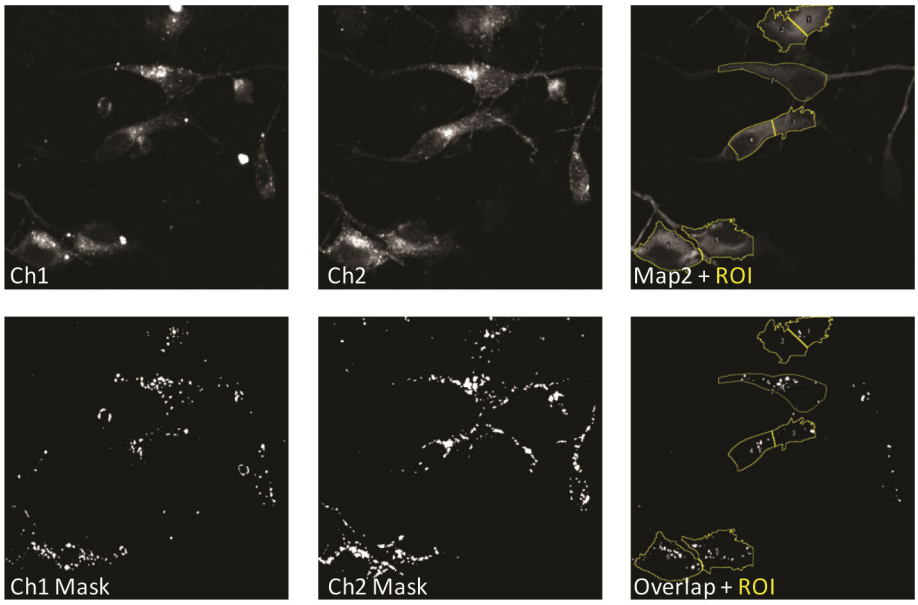

B

Slice	Count	Total Area	Average Size	%Area
C1_C2	4	1.8095	0.4524	1.4862
C1_C2	0	0	NaN	0
C1_C2	1	0.2154	0.2154	0.1961
C1_C2	6	3.4467	0.5745	2.5723
C1_C2	15	8.4444	0.563	3.2585
C1_C2	20	12.4081	0.6204	4.6776
C1_C2	18	10.6417	0.5912	4.8834

Figure 2-2 Quantification of 2-Channel Colocalization in Soma ROI
A) Example of a three color staining experiment where Ch1 and Ch2 are puncta images. The corresponding Map2 image is also depicted with soma ROIs outlined in yellow. Ch1 and Ch2 are thresholded as in Figure 2-1 and mask images are inputted into the Overlap_Counts_in_ROI script. Using the ImageCalculator function in ImageJ, overlapped puncta can be identified. B) An example output file of the counted puncta that overlapped used to quantify percent colocalization.

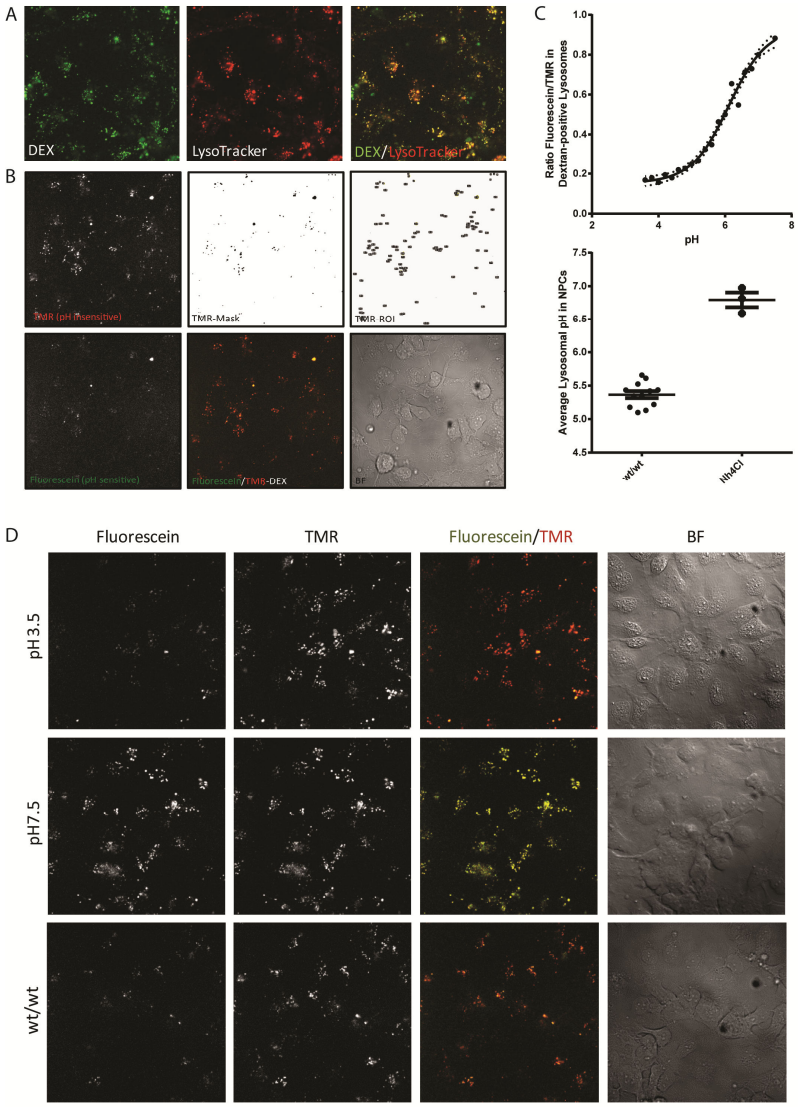

Figure 2-3 Ratiometric Fl/TMR Dextran to Measure Lysosomal pH in Cultured NPCs
A) Following a >12 hour chase, the majority of internalized Fl-Dextran overlaps with the established lysosomal marker for live cells, Lysotracker DND-99. B) An example of a field of cells labeled with the dual conjugated Fl/TMR Dextran where the TMR channel is pH insensitive and the fluorescein (Fl) channel is pH sensitive. The TMR channel is thresholded to identify lysosomal puncta and ROIs are automatically generated. C) Each individual puncta has an intensity ratio of Fl/TMR that can be plotted on a standard curve using pH buffers. Experimental lysosomal pH from wt/wt cells is depicted below the standard curve as well as a positive control of NH4Cl that dramatically increases lysosomal pH by deacidifying the lysosomes. D) Example images of untreated wt/wt cells or with pH calibrated buffers of 3.5 and 7.5 added. Note the dramatic increase in fluorescein fluorescence with pH 7.5 buffer.

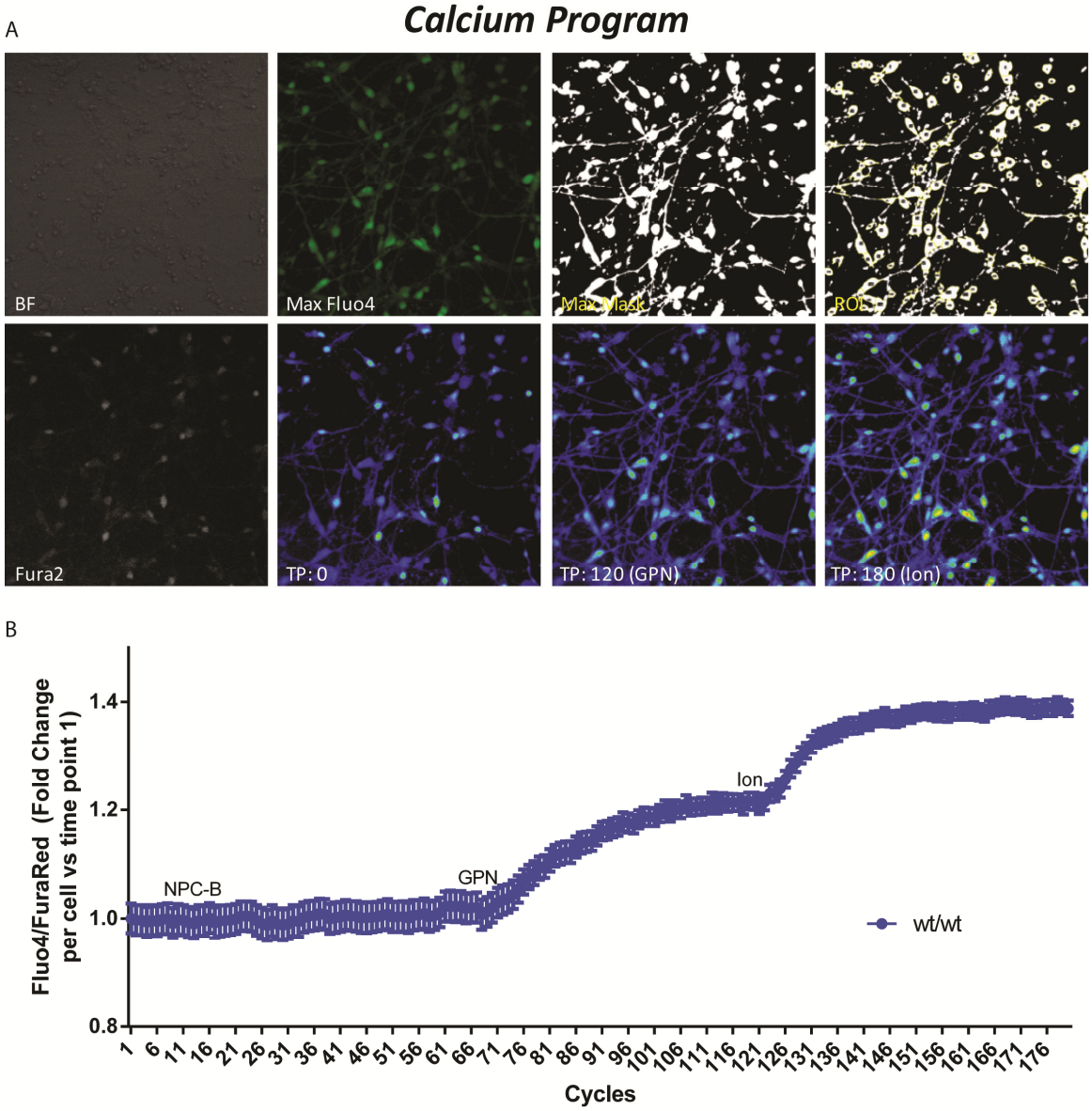

Figure 2-4 Automated Quantification of Calcium Dynamics in hIPSC-Derived Neurons
A) Neurons are labeled simultaneously with Fluo4 (Green) and Fura Red (white). The maximum Intensity Projection of all Fluo4 labeled neurons is generated (Max Fluo4) to identify soma ROI. Again, a masked image from the Maximum Intensity Projection is generated to identify Soma ROI. From there, mean intensity of individual soma can be obtained. To measure lysosomal calcium, cells are exposed to GPN at cycle 120, leading to osmotic lysis of the lysosomes and an increase in Fluo4 intensity relative to Fura Red. At the conclusion of the experiment, ionomycin is added to measure ER calcium and to ensure that the calcium signal is not maxed out after GPN treatment. B) An example trace from the combined results of three separate experiments representing >50 neurons.

A

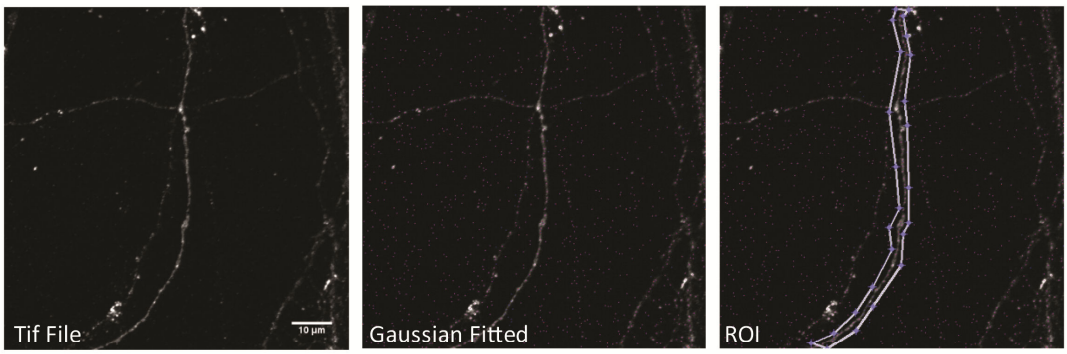

B ROI Output Matlab File

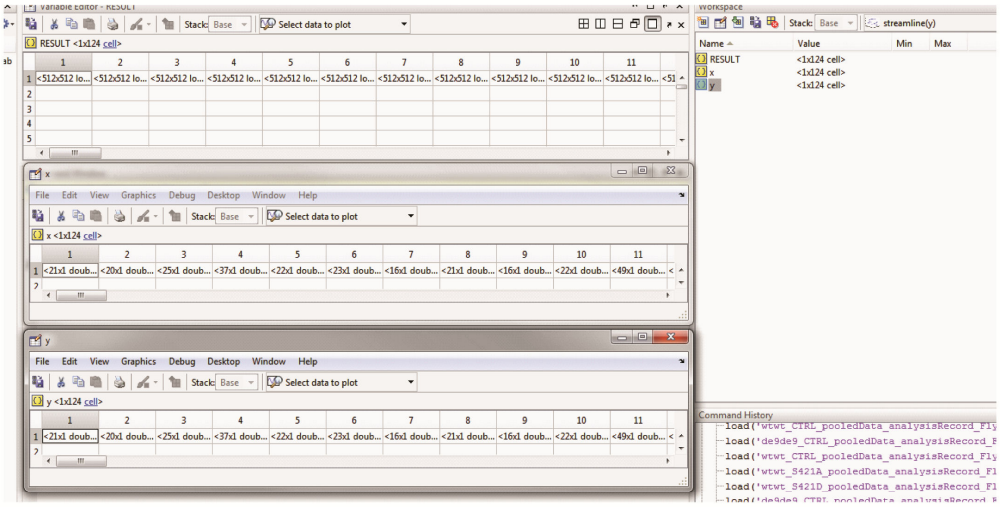

C Density Output

GROUP	Axon ID	Ch1	Ch2	Ch3	AXL
Axons	1	0.65	0.71	0.85	86.35
Axons	2	0.48	0.49	0.7	114.37
Axons	3	0.58	0.31	0.74	98.56
Axons	4	0.21	0.22	0.32	143.5
Axons	5	0.28	0.43	0.59	94.29
Axons	6	0.41	0.3	0.56	107.13
Axons	7	0.57	0.42	0.74	85.98
Axons	8	0.5	0.46	0.66	95.82
Axons	9	0.29	0.37	0.59	87.07
Axons	10	0.32	0.36	0.62	98.67
Axons	11	0.4	0.4	0.58	279.28
Axons	12	0.24	0.41	0.52	169.6
Axons	13	0.2	0.46	0.44	90.02
Axons	14	0.57	0.43	0.74	100.76

D Colocalization Output

GROUP	Axon ID	ADATA(X)	ADATA(Y)	Ch2 CNT	Ch3 CNT	BOTH	NONE	Ch1 AMP	Ch2 AMP	Ch3 AMP
Axons	1	157.9625	475.0117	0	1	0	0	551.7109	0	551.7109
Axons	1	161.987	462.6054	0	0	0	1	224.8808	0	0
Axons	1	162.0666	468.2559	1	1	1	0	2643.993	320.074	2643.993
Axons	1	162.5615	482.2167	0	0	0	1	241.9687	0	0
Axons	1	166.0654	476.4086	0	0	0	1	234.3368	0	0
Axons	1	154.9401	498.9135	0	1	0	0	656.5549	0	656.5549
Axons	1	162.229	489.5568	0	1	0	0	1276.52	0	1276.52
Axons	1	170.1823	461.4273	0	1	0	0	422.7935	0	422.7935
Axons	1	174.1207	449.1832	0	1	0	0	787.7641	0	787.7641
Axons	1	175.9207	454.9743	0	1	0	0	927.5229	0	927.5229
Axons	1	178.7254	446.2226	0	1	0	0	291.421	0	291.421
Axons	1	178.6725	382.0147	0	1	0	0	508.9482	0	508.9482
Axons	1	179.276	401.7947	0	1	0	0	257.5277	0	257.5277
Axons	1	178.872	406.99	0	0	0	1	176.0127	0	0

Figure 2-5 A Semi-Automated Approach to Quantify Axonal Puncta

A) An example of a neuronal axon stained with APP and the Gaussian-fitted puncta identified using a previously established Matlab program. An axonal ROI is manually generated to identify axons. B) A Matlab file is generated with the axonal ROI stored in three sub-folders (RESULT, x, and y). C and D) Using the Gaussian-fitted files generated from scriptdetectgeneral and the axonal ROI file generated from Sol_Make_ROIs_v1, axonal puncta density (C), puncta intensity (D), and colocalization (D) can be rapidly quantified.

3. Reduced Endocytosis and Transcytosis of APP and Lipoproteins Owing to Accumulation of β-CTF Fragments in Familial Alzheimer's Disease Mutations

Abstract

We used human isogenic iPSC-derived neurons to investigate early Alzheimer's Disease phenotypes caused by familial Alzheimers Disease (fAD) mutations. Analysis of these neurons revealed that fAD mutant neurons had decreased endocytic recycling and transcytosis of APP and lipoproteins; this reduction could be rescued by treatment with a β-secretase inhibitor. Our data suggest that accumulation of β-CTFs slows vesicle budding from an endocytic recycling compartment marked by the transcytotic GTPase Rab11. Strikingly, decreased lipoprotein endocytosis and transcytosis to the axon is common to many fAD mutations and suggests that impaired axonal delivery of lipoproteins compromises synaptic maintenance in fAD.

3.1 Introduction

Alzheimer's Disease (AD) is a progressive neurodegenerative disease that affects more than 30 million people worldwide including 11% of those over 65 years of age and 32% of those over 85 (Fargo and Bleiler, 2014). The disease is characterized by progressive cerebral dysfunction, memory loss, and neuronal impairment leading to cell death. To date, there are no disease-modifying treatments that can cure or reduce the progression of AD. Genetically, AD is segmented into two populations: sporadic AD (sAD) where the underlying cause is not known and rare, autosomal-dominant mutations of familial AD (fAD) (Gatz et al., 2006). The common pathological features of the sAD and fAD patients are the accumulation of senile plaques composed of aggregated amyloid-β (Aβ) and neurofibrillary tangles (NFT), composed of hyper-phosphorylated tau (Spires-Jones and Hyman, 2014). The majority of clinical trials have focused largely on the amyloid cascade hypothesis of AD, which posits that extracellular Aβ fragments and intracellular tau accumulate abnormally in AD and drive cellular stress, neurotoxicity, and ultimately neurodegeneration. While considerable evidence exists to support the amyloid cascade model, clinical trials that rely on this model have been unsuccessful. In part, the high failure rate (99.6%) may be because the majority of clinical trials seek to reduce Aβ burden in the brain without considering the effects of candidate drugs on other amyloid precursor protein (APP) fragments and other AD-relevant pathways (Toyn and Ahlijanian, 2014).

APP is proteolytically cleaved in sequential steps by α-secretase and γ-secretase along the non-amyloidogenic pathway, and by β-secretase (BACE1) and γ-secretase along the amyloidogenic route. Prominent drug failures include the γ-secretase inhibitors, Semagecestat and Avagacestat, both of which were terminated because of side effects, including worsened cognitive outcomes. This may be because γ-secretase inhibition, while reducing Aβ, also increases the levels of APP β-CTFs, which are known to have toxic effects and can severely impair neuronal function (Jin et al., 2002; Lu et al., 2000; Toyn and Ahlijanian, 2014; Weissmiller et al., 2015). Better drug candidates may be the class of BACE inhibitors that seek to shift processing of APP to the α-secretase pathway and inhibit production of β-CTFs (C-terminal fragments) and Aβ. BACE as a clinical target is also attractive because mutations that enhance BACE activity (APP Swedish KM670/671NL) are strongly pathogenic, while the protective APP mutation A673T reduces BACE processing, consequently reducing Aβ and β-CTF production and lowering AD risk (Jonsson et al., 2012; Stamford and Strickland, 2013; Vassar et al., 2014).

Despite the known cytotoxicity of β-CTFs and their equimolar relationship to Aβ, studies of this immediate precursor to Aβ are incomplete. In large part, understanding the disease-relevant roles of β-CTFs is limited by the use of model systems that incompletely recapitulate AD (Balducci and Forloni, 2011; Braidy et al., 2012; Goldstein et al., 2014). For this reason, we sought to use a human system that expressed endogenous levels of human fAD mutations in Presenilin

1 (PS1) and APP that cause increased levels of β-CTFs. Beyond the consensus that APP and PS1 fAD mutations alter APP processing, increasing Aβ42/40 ratio and β-CTF levels, there is little agreement in the field about how these mutations initiate pathogenic events that eventually lead to neurodegeneration. Previous work suggested that β-CTF accumulation might cause defects in lipoprotein internalization, but how general this defect might be and what cellular pathways might be dysregulated are not yet understood (Tamboli et al., 2011; Walter and van Echten-Deckert, 2013).

We tested whether isogenic iPSC-derived neurons with fAD mutations display early cellular phenotypes beyond the known effects on APP processing, including altered endocytosis and sorting of cargo (Von Bartheld, 2004; Cataldo et al., 2000; Ginsberg et al., 2010; Karch and Goate, 2014; Lee et al., 2010; Maxfield, 2014). We found that fAD mutant neurons alter subcellular distribution of APP and internalized lipoprotein, leading to elevated levels of APP in the soma and reduced levels in the axons. The redistribution of APP is accompanied by the concurrent accumulation of a Rab11 compartment in the soma and reduced axonal staining, suggesting that the reduction in axonal APP and lipoproteins can be partly explained by reduced Rab11-dependent soma-to-axon transcytosis (Ascaño et al., 2009; Von Bartheld, 2004; Buggia-Prévot et al., 2014). Knockdown of Rab11 causes similar phenotypes, which are also rescued by treatment with a β-Secretase inhibitor. In keeping with these data, these alterations are not accompanied by changes in lysosomal pH or bulk

endocytosis. Our study thus reveals that a common defect among fAD mutations is βCTF accumulation-induced impairment of neuronal transcytosis of Rab11-cargoes such as APP and lipoproteins.

3.2 Methods

3.2.1 Cell Culture

Isogenic iPSCs and NPCs were derived as previously described (Israel et al., 2012; Woodruff et al., 2013; Yuan et al., 2011). Purified neurons were generated by differentiating NPCs for 3 weeks in medium containing DMEM:F12 + Glutamax, .5x N2 (Life Technologies), .5x B27 (Life Technologies), and 1x Pen/Strep on plates coated with 20ug/mL poly-ornithine and 5ug/mL laminin (both from Sigma). Media was replaced twice per week. After the 3-week differentiation, neurons were purified by fluorescence activated cell sorting (FACS, BD Biosciences). Cells were stained with CD184, CD44, CD24 (all from BD Bioscience) and cells that were CD184-, CD44- and CD24+ were selected and plated on poly-ornithine/laminin coated plates. Purified neurons were cultured in the same medium as above with the addiiton of 0.5mM dbcCAMP (Sigma), 20ng/mL brain-derived neurotrophic factor, and 20ng/mL glial cell line-derived neurotrophic factor (both from Peprotech). Cells that were grown in microfluidic compartments were differentiated for 3 weeks and then dissociated and the mixed culture was plated in compartments with medium and growth

factors as above. Transcytosis experiments were performed after cells had been in microfluidic compartments for 7-10 days.

3.2.2 Statistical Methods

Statistics were performed using GraphPad Prism. Normality for each data set was assessed using D'Agostino-Pearson test. When data were normally distributed, a two-way ANOVA with a post hoc Tukey test was used to compare genotypes. Most immunofluorescence data were non-normally distributed and a nonparametric Kruskal-Wallis test with Dunn's multiple comparison was used to compare genotype medians.

3.2.3 Immunofluorescence

Purified neurons were grown in 384-well imaging plates at a density of 25,000 cells per well for 7-9 days post-sort. For most experiments, neurons were fixed in 4% paraformaldehyde and PBS for 30 min at 37°C, permeabilized with 0.1% Triton X-100, and blocked in blocking media (10% donkey serum, 3% BSA, 0.1% Triton X-100 in PBS) (Szpankowski et al., 2012). For surface labeling experiments, neurons were not permeabilized and Triton X-100 was excluded from the experiment. For compartment experiments, Polydimethylsiloxane (PDMS) microfluidic devices were plasma bonded directly onto 22x50 VWR glass coverslips (Niederst et al., 2015). Dissociated differentiated NPCs were seeded at a density of 1-3 million cells per compartment and grown for 7-10 days (until

axons passed through the channels). At this point, compartments were fixed as above and imaged in PBS. Antibodies used for immunofluorescence experiments were rabbit anti-Rab11 (1:1000, Life Technologies 71-5300), rabbit anti-APP Y188 (1:200, Abcam ab32136), mouse anti-APP 22C11 (1:100, EMD Millipore, MAB348), mouse anti-TrkB (1:100, BD 610101), mouse anti-EEA1 (1:100, BD 610457), mouse anti-Lamp-2/CD107b (1:200, BD 555803), mouse anti-NF-H (1:1000, Biolegend SMI-31r), and chicken anti-Map2 (1:500, ab5392). Secondary antibodies were Alexa Fluor donkey anti-mouse and anti-rabbit IgG (Invitrogen) and Dylight 405 donkey anti-chicken IgY from (Jackson ImmunoResearch, 703-475-155) and were used at 1:200. Images were acquired on a Zeiss confocal microscope.

3.2.4 Automated Image Analysis

In order to perform unbiased, quantitative analysis of fluorescent images, a series of ImageJ scripts were developed. In all soma immunofluorescence experiments, neurons were labeled with chicken anti-Map2 and stained with the secondary antibody Dylight 405 donkey anti-chicken IgY from (Jackson ImmunoResearch, 703-475-155). The blue Map2 channel served to delineate and identify soma borders (**Figure 2-1A**)**.** The SomatoDendrite_ROI script used thresholding to generate black and white mask images, which was then used to identify soma bodies 50-200 um^2 in size. Zip files corresponding to the soma ROIs from each image were then used to quantify fluorescent intensity in

unthresholded images from the other channels with MeasureIntensityinROI script (**Figure 2-1B**)**.** To quantify neuronal puncta, a separate script, PunctaInROIAnalysis, was developed that used the thresholding and Analyze Particles features of ImageJ to automatically segment and count puncta in the ROIs generated from SomatoDendrite_ROI (**Figure 2-1C and D**). Example output text files can be seen for PunctaInROIAnalysis (C) and MeasureIntensityInROI (D) scripts.

3.2.5 Endocytosis, Recycling, and Transcytosis

For constitutive uptake endocytosis assays, neurons were incubated with LDL-Bodipy (20 ug/ml, Invitrogen L3483), Dextran-tetramethylrhodamine (TMR) (250 ug/ml, Invitrogen D1817), or Transferrin-647 (25 ug/ml, Invitrogen T-23366) at 37°C for indicated times, fixed, and imaged. For recycling assays, neurons were treated with Transferrin-647 at 37°C and allowed to internalize for 20 minutes. Neurons were washed twice in warm media and then chased for the indicated amount of time. For all fixed endocytosis assays, a custom ImageJ program was used to identify Map2-positive soma and automatically generate region of interests (ROI) corresponding to soma. Mean intensity and puncta count per soma were then determined and averaged across images and experiments. All endocytosis assays were repeated at least three times.

For transcyctosis experiments, dNPCs were grown in compartments and treated on the soma side with LDL-Bodipy (20 ug/ml), LDL-DiI (12.5 ug/ml), or

mouse anti-22C11 (1:100) for 4 hours with axons in fluidic isolation. Axonal puncta analysis was done as previously described with modifications (Szpankowski et al., 2012) (See **Figure 2-5**) **.** Briefly, axons were imaged at 100x and a custom Guassian-fitting colocalization package in MATLAB (MathWorks) was used to calculate axonal density, mean puncta intensity, and percent colocalization per axon.

3.2.6 Lysosomal pH Measurements

To measure lysosomal pH by microscopy, NPCs or dNPCs were grown in 96 well imaging plates and incubated with Dextran, fluorescein and tetramethylrhodamine (Fl/TMR) (250 ug/ml, Invitrogen D1951) or Lysosensor Yellow/Blue Dextran (Invitrogen, L-22460) for 2-6 hours. Cells were then washed twice with warm media and dextran was chased into the lysosomes for >12 hours. Red/green or Yellow/Blue wavelengths were captured simultaneously in live cells. Cells incubated with dextran Fl/TMR were imaged on a confocal microscope in warm media. Imaging time was limited to half an hour per plate. A custom ImageJ program identified all red puncta greater than 0.2 um in size (lysosomes, pH-insensitive dye) and then the ratio of green/red mean intensity per puncta was determined. Cells incubated with Lysosensor Yellow/Blue Dextran were imaged on a plate reader. Cells were excited at 352 nm and simultaneously measured for Yellow and Blue fluorescence. To generate a standard curve, wild-type cells were treated with pH-calibrated buffers and the

average green/red or yellow/blue ratio per image was fit to a standard curve (See **Figure 2-3**). (Diwu et al., 1999; Lee et al., 2010)

3.2.7 Surface Biotinylation Assay

NPCs were grown in 6 well plates and differentiated down a neuronal lineage as described in the Cell Culture methods. At 5 weeks, neuronal media was changed to warm fresh media or media supplanted with 12.5 ug/ml of unlabeled LDL for 4 hours. At the end of the incubation, differentiated NPCs were washed twice with ice-cold PBS and then incubated at 4C with 2mM EZ-Link™ Sulfo-NHS-SS-Biotin (Life Technologies) in PBS for 30 minutes. Cells were then lysed in equal volumes of RIPA buffer. For pulldown experiments, 200 ug of harvested protein at 0.5 ug/ul was incubated with 50 ul of pre-washed Pierce Streptavidin Magnetic Beads (Life Technologies, 88817) overnight at 4C. The next day, a sample of input was saved for bookkeeping and beads were washed to remove residual, unbound proteins and biotinylated proteins were released from the streptavidin beads by boiling samples in loading buffer at 100C. Westerns were run with 5% of input, 5% of supernatant, and 50% of pull down. Quantification of recycling was determined based on input signal. (Pull down/Input)

3.3 Results

3.3.1 The PS1$^{\Delta E9}$ Mutation Increases APP in the Soma of Human Neurons and Decreases APP in Axons

PS1 has been reported to have a role in APP trafficking in primary neurons and in non-neuronal cell types (Burns et al., 2003; Cai et al., 2003; Gandy et al., 2007; Zhang et al., 2006). PS1 knockout has been reported to increase cell surface APP (Leem et al., 2002), while PS1 FAD mutations have been shown to delay APP arrival at the cell surface (Cai et al., 2003; Gandy et al., 2007). To determine whether the PS1$^{\Delta E9}$ mutation affects APP localization in human neurons, we generated purified neurons from isogenic iPSC cell lines of controls and lines heterozygous and homozygous for the PS1$^{\Delta E9}$ mutation (Woodruff et al., 2013). We stained with an APP antibody, which has minimal staining in an APP knockout background in both mice (Guo et al., 2012; Weissmiller et al., 2015) and human iPSC-derived neurons (**Figure 3-1**). We found that PS1$^{wt/\Delta E9}$ and PS1$^{\Delta E9/\Delta E9}$ neurons exhibited increased APP staining in the cell body (**Figure 3-2A**), including increased APP puncta and APP puncta intensity (**Figure 3-2B**). To determine whether APP was also increased on the surface of PS1$^{\Delta E9}$ neurons, we stained unpermeabilized purified neurons with an N-terminal APP antibody that recognizes the extracellular portion of APP (22C11) (**Figure 3-2C**). We observed increased surface APP in the soma of PS1$^{\Delta E9}$ neurons (**Figure 3-2C**).

We previously published that PS1$^{\Delta E9}$ neurons do not exhibit changes in total levels of full-length APP though there are increases in the APP CTFs

(Woodruff et al., 2013). The increase in soma APP suggests that APP CTFs are accumulating in the soma of purified neurons and/or that APP is missorted possibly at the expense of axonal APP. We therefore assessed APP staining in the axons of $PS1^{\Delta E9}$ neurons. To ensure that we were quantifying staining in axons and not dendritic processes, we made use of microfluidic compartments, which separate axons from the bulk somatodendritic population (See **Figure 4-2A**) (Niederst et al., 2015; Selfridge et al., 2015; Taylor et al., 2006). As shown in **Figure 4-2B**, differentiated neural progenitor cells (NPCs) grown in microfluidic devices extend long processes into the axonal space that do not stain for the somatodendritic marker Map2 and that do stain for the axonal marker neurofilament-H (SMI31 clone). We observed that $PS1^{\Delta E9}$ axons grown in microfluidic devices have decreased axonal APP puncta with diminished APP puncta intensity (**Figure 3-2D**); this decrease is sensitive to $PS1^{\Delta E9}$ gene dose. To test whether the phenotypic differences that we observed in $PS1^{\Delta E9}$ neurons might be due to differences in neuronal subtypes in our cultures we stained neurons of each genotype with the neuronal subtype markers GABA, GAD65/67 and vGlut (**Figure 3-3A**). We found no significant differences in the proportion of cells that stained positive for GABA, GAD65/67 or vGlut between different genotypes (**Figure 3-3B**), which suggests that APP localization differences and other phenotypes we observed were not due to a difference in neuronal subtype.

3.3.2 Rab11 Distribution is Altered in $PS1^{\Delta E9}$ Neurons

There are at least two pathways by which APP can be delivered to the axon. The first is by direct delivery from the trans Golgi network (TGN) and the second is by an indirect pathway where APP first arrives at the cell surface of the somatodendritic compartment, then undergoes endocytosis and sorting to the axon. The indirect pathway is a process known as transcytosis and multiple cargo, including APP (Niederst et al., 2015), TrkA (Ascaño et al., 2009) and L1/NgCAM (Anderson et al., 2005; Yap et al., 2008) (among other proteins, trophic factors, tracers, and pathogens (Von Bartheld, 2004)) have been demonstrated to be sorted along this pathway in neurons.

One endocytic regulator that functions at the intersection of the TGN and transcytotic pathways is the Rab GTPase Rab11 (Welz et al., 2014). Rab11 has a well-established role in mediating recycling of many receptors including transferrin receptor (Ullrich et al., 1996), and LDL receptors (Sakane et al., 2010; Takahashi et al., 2007). In addition to its role in recycling, Rab11 has also been shown to mediate transcytosis in epithelial cells and neurons. Specifically, in neurons, TrkA receptors undergo Rab11-dependent transcytosis to the axon (Ascaño et al., 2009; Lazo et al., 2013). Rab11 may also be involved in trafficking of BACE1 to the axon (Buggia-Prévot et al., 2014), colocalizes with APP in axons (Niederst et al., 2015), and was recently identified in an unbiased RabGTPase screen as a regulator of Aβ and sAPPβ production (Udayar et al., 2013). Intriguingly, presenilins have also been reported to interact directly with Rab11 through their hydrophilic loop (Dumanchin et al., 1999).

To determine if Rab11 could be playing a role in the reduction of axonal APP, we stained neurons with a Rab11 antibody and measured Rab11 in the somatodendritic and axonal compartments. The Rab11 staining was reminiscent of the altered APP distribution such that $PS1^{\Delta E9/\Delta E9}$ neurons exhibited increased soma Rab11 intensity, Rab11 puncta, and Rab11 puncta area **(Figure 3-4A)**. In axons, both the $PS1^{wt/\Delta E9}$ and $PS1^{\Delta E9/\Delta E9}$ genotypes had decreased Rab11 puncta density and puncta intensity **(Figure 3-4B)**. In support of a role in Rab11-dependent trafficking of APP to the axon, shRNA-mediated knockdown of Rab11 on the soma-side of neurons grown in microfluidic devices resulted in a dramatic reduction in APP axonal staining (data not shown)**.** In keeping with a transcytotic route of APP to the axon, somatodendritic inhibition of endocytosis with the dynamin-inhibitor, Dynasore led to reduced APP and Rab11 density in axons (**Figure 3-4C**). These findings are consistent with a previous study from our lab using a different Rab11 antibody (Niederst et al., 2015).

We also tested the early endosome effector, EEA1, and the lysosomal marker, Lamp2, even though they are not thought to traffic substantially to axons (Wilson et al., 2000). In fact, though differences in EEA1 and Lamp2 size and puncta counts were previously reported in PS1 mutations (Lee et al., 2010; Neely and Green, 2011; Tarabal et al., 2001), in our $PS1^{\Delta E9}$ iPSC-derived neurons the stains were not dramatically different (though there were a tendency toward larger puncta) suggesting that they are not playing an active role in sorting APP to the axon (data not shown).

3.3.3 The PS1$^{\Delta E9}$ Mutation Decreases Endocytosis and Transcytosis of APP and LDL

Since we observed alterations in the subcellular distribution of both APP and Rab11 in PS1$^{\Delta E9}$ neurons, we investigated whether endocytosis, recycling and/or transcytosis could account for the APP localization changes. To assess endocytosis of APP we treated purified neurons with an N-terminal APP antibody (22C11) and allowed cells to internalize antibody for 30 minutes, 120 minutes or 140 minutes and fixed cells at each of those timepoints. We then stained with a secondary antibody and quantified the amount of APP endocytosis at each timepoint (**Figure 3-5A**). We observed a decrease in APP puncta in the PS1$^{\Delta E9/\Delta E9}$ genotype starting at 30 minutes compared to PS1$^{wt/wt}$ and this decrease was more prominent at both the 2 and 4 hour timepoints (**Figure 3-5A**). The PS1$^{wt/\Delta E9}$ genotype also exhibited decreased APP puncta compared to PS1$^{wt/wt}$ at the 2 and 4 hour timepoints. To assess whether this endocytosis defect was specific to APP or common to other Rab11-dependent cargo, we also measured uptake of fluorescently labeled LDL at 30 minutes, 1 hour, 2 hours and 4 hours (**Figure 3-5B**). Similar to what was observed with APP, LDL puncta intensity and LDL puncta density were reduced in PS1$^{wt/\Delta E9}$ and PS1$^{\Delta E9/\Delta E9}$ neurons at 2 hours and 4 hours (**Figure 3-5B**). To test if the differences observed were due to a non-specific defect in endocytosis, we also quantified uptake of fluorescently labeled dextran as a marker of bulk endocytosis. We did not

observe any significant differences in dextran endocytosis at any timepoint (**Figure 3-5E**).

We measured transcytosis of APP and LDL by growing neurons in microfluidic compartments. The axon side of the compartment was kept in fluidic isolation from the soma side and APP antibody or labeled LDL was added only to the soma side. Transcytotic delivery of cargo from the axon to the soma is a relatively slow process since internalized cargo has to travel long distances (on the order of millimeters in cultured neurons). When we measured transcytosed LDL after 2 hours of continuous uptake in axons of differentiated NPCs grown in compartments, we saw minimal, if any, fluorescent labeling (data not shown). Therefore, we restricted our analysis to the 4 hour time point for transcytosis experiments. At 4 hours, cells were fixed and we quantified the amount of anterogradely transcytosed APP by using an anti-mouse secondary antibody; fluorescent LDL was measured directly (**Figure 3-5C, D**). We observed that both the $PS1^{wt/\Delta E9}$ and $PS1^{\Delta E9/\Delta E9}$ genotypes exhibited decreased APP axonal density and APP intensity after 4 hours of transcytosis (**Figure 3-5C**). Similarly, LDL axonal density and intensity were also decreased in $PS1^{wt/\Delta E9}$ and $PS1^{\Delta E9/\Delta E9}$ axons after 4 hours (**Figure 3-5D**).

These results suggest that the reduction in axonal APP in $PS1^{\Delta E9}$ neurons is due to a decrease in a transcytosis pathway.

3.3.4 Rab11 Mediates Transcytosis of APP and LDL

To further investigate the role of Rab11 in endocytosis of LDL and transcytosis of APP and LDL, we used shRNA-mediated knockdown of Rab11 in wildtype neurons (**Figure 3-6B**). Knockdown of Rab11 in $PS1^{wt/wt}$ neurons almost completely abolished LDL endocytosis in the somatodendtric region (**Figure 3-6A**) and transcytosed LDL was undetectable under RAB11 knockdown conditions (Figure 4D). Similarly, Rab11 knockdown also decreased axonal APP (**Figure 3-6D**). To further characterize the transcytotic vesicle carrying LDL, we costained with combinations APP, Kinesin light chain (KLC) and LRP1. After 4 hours of LDL transcytosis, LDL vesicles colocalize with LRP1, APP, KLC and Rab11. Further support for a Rab11-dependent route in sorting APP comes from immunofluorescence experiments where axons with transcytosed APP (22C11) were co-stained with Rab11. 34.68% of Rab11 overlapped with transcytosed APP in $PS1^{wt/wt}$ axons and about 23.39% of transcytosed APP overlapped with Rab11 in $PS1^{wt/wt}$ axons (data not shown).

The absence of a lipoprotein endocytic defect at early time-points suggested that transcription, levels, degradation, or recycling of the LDL receptor may be driving the reduction in transcyctosis. While there are many potential LDL receptors, LRP1 was an attractive candidate because of its high expression in brain and neuronal samples (Zhang et al., 2014)**.** To determine if transcription or degradation of LRP1 was affected in $PS1^{\Delta E9}$ mutations, we treated purified human neurons with unlabeled LDL and harvested neurons for mRNA and protein. We did not observe differences in APP or LRP1 mRNA or protein levels

(Figure 3-7A, B) at baseline or after LDL treatment, suggesting that transcription, levels, or degradation of LRP1 are not playing a role in the reduced endocytosis of APP and LDL. Though PS1 has been hypothesized to drive reduced degradation of proteins because of alterations in lysosomal pH (Nixon and Mcbrayer, 2013; Nixon and Yang, 2011), we did not observe changes in lysosomal pH in the $PS1^{\Delta E9}$ mutations as assessed by the two ratiometric pH probes LysoSensor Yellow/Blue Dextran and fluorescein-tetramethylrhodamine Dextran (**Figure 3-8A**).

In addition, degradation of full-length APP is not different in $PS1^{\Delta E9/\Delta E9}$ neurons treated with cycloheximide (**Figure 3-8B**) or when lysosome degradation is blocked with chloroquine. Activation of autophagy pathways as measured by chloroquine-induced changes in LC3 II/I ratio is also not altered in $PS1^{\Delta E9/\Delta E9}$ differentiated NPCs (**Figure 3-8B**). Interestingly, LRP1 protein levels are not reduced by cycloheximide treatment in the time points analyzed, suggesting LRP1 requires an external source of cholesterol to initiate degradation of the receptor (**Figure 3-8C**).

To determine if the amount of lipoprotein receptors at the somatodendritic surface are driving endocytosis defects, we measured LDL receptor number at baseline and after 4 hours of LDL treatment using two different methods. First, we incubated purified neurons under cold conditions with labeled LDL at 0 and 4 hours, and fixed and imaged the neurons without permeabilization (**Figure 3-7C and D**). Under these conditions, we did not observe differences in surface LDL

puncta counts in homozygous $PS1^{\Delta E9/\Delta E9}$ neurons compared to $PS1^{wt/wt}$ neurons. Since LDL could be binding non-specifically to the cell surface, we evaluated specific receptor populations by biotinylating the surface of neurons with a cleavable biotin (Sulfo-NHS-LS-Biotin, Pierce) and used streptavidin beads to pull down surface proteins before and after LDL treatment. Probing for LRP1 demonstrated that the surface levels of LRP1 receptor is not different at baseline but is decreased in $PS1^{\Delta E9/\Delta E9}$ differentiated NPCs after LDL treatment (**Figure 3-7E and F**). This indicates that LRP1 recycling back to the surface after LDL treatment is reduced in $PS1^{\Delta E9/\Delta E9}$ differentiated NPCs.

3.3.5 LDL Endocytosis Defects in PS1ΔE9 Neurons are Rescued by β-secretase Inhibition

PS1 is the catalytic core of the γ-secretase complex which cleaves the β-CTF fragment of APP that is generated by β-secretase cleavage of full-length APP. We previously demonstrated that the $PS1^{\Delta E9}$ mutation impairs γ-secretase activity and APP CTFs accumulate in $PS1^{\Delta E9}$ neurons (Woodruff et al., 2013). A previous study also demonstrated that γ-secretase inhibition in MEFs reduces LDL endocytosis (Tamboli et al., 2011). To determine if γ-secretase activity or if the β-CTF fragment might be responsible for the impaired LDL endocytosis in human neurons, we treated $PS1^{wt/wt}$ neurons with β- and γ-secretase inhibitors and measured LDL endocytosis (**Figure 3-9A**). Since the most robust difference in LDL internalization was seen at 4 hours, we restricted our data analysis to this

last time point. γ-secretase inhibition severely decreased LDL endocytosis at 4 hours while β-secretase inhibitor had no significant effect (**Figure 3-9A**). Treatment with both β- and γ-secretase inhibitors caused a marked accumulation of α-CTFs while ablating β-CTFs (**Figure 3-9D**), but had no effect on LDL endocytosis at 4 hours (**Figure 3-9A**). These results suggest that the β-CTF fragment of APP is responsible for impairing LDL endocytosis in ΔE9 neurons. To further test this possibility, we treated $PS1^{\Delta E9}$ neurons with a β-secretase inhibitor and measured LDL endocytosis (**Figure 3-9B**). We observed that upon treatment with a β-secretase inhibitor, $PS1^{\Delta E9/\Delta E9}$ neurons were rescued in the ability to endocytose LDL (**Figure 3-9B**). Treatment of $PS1^{\Delta E9/\Delta E9}$ neurons with both β- and γ-secretase inhibitors also rescued the LDL endocytosis defect (**Figure 3-9B**), which suggests that accumulation of only the β-CTF is responsible for impaired LDL endocytosis (**Figure 3-9D**)**.** Example images of the drug treatments analyzed are depicted in (**Figure 3-9C**).

3.3.6 LDL Endocytosis Defects are Common to Other FAD Mutations

Accumulation of APP β-CTFs is a phenotype shared by many APP and PS1 FAD mutations (Chang and Suh, 2005; Sinha and Lieberburg, 1999). To assess whether other PS1 mutations might share a common phenotype of impaired LDL endocytosis and transyctosis, we generated additional isogenic cell lines harboring either the $PS1^{A246E/null}$ mutation mutations (Table 1) (Sherrington et al., 1995). In $PS1^{A246E/null}$ mutant neurons we observed significantly decreased

LDL endocytosis after 4 hours; this defect was rescued to near wild-type levels when neurons were treated with a β-secretase inhibitor **(Figure 3-10A** and **B)**. This finding demonstrates that the reduction in LDL endocytosis is not specific to the $PS1^{\Delta E9}$ mutation but may be a common feature of many PS1 mutations.

Since the combination of drugs we used are not specific to APP and can have a variety of other targets, we also tested if βCTFs alone are sufficient to drive reduced endocytosis of LDL by overexpressing GFP or βCTF-EGFP (C99-EGFP) in neurons (Rodrigues et al., 2012). After 48 hours of transfection, we incubated cultured neurons with labeled LDL for 4 hours and fixed cells for analysis. βCTF-EGFP transfected neurons had reduced LDL uptake compared to GFP-transfected alone at 4 hours **(Figure 3-10C)**.

In contrast, neurons that are haploinsufficient for PS1 ($PS1^{wt/null}$) do not have a defect in LDL internalization (not shown). This argues against a role for simple presenilin reduction of function in driving the observed LDL defect and supports the hypothesis that βCTF accumulation is the primary player. In further support of a βCTF-dependent effect on lipoprotein internalization, isogenic lines with $APP^{wt/V717F}$ and $APP^{V717F/V717F}$ mutations, which accumulate βCTFs **(Figure 3-10D)**, also drive reduced LDL endocytosis at 4 hours.

To assess whether other FAD mutations might share a common phenotype of impaired LDL endocytosis, we generated additional isogenic cell lines harboring either the APP V717F (APP^{V717F}) or APP Swedish (APP^{swe}) mutations (Sherrington et al., 1995). In neurons heterozygous and homozygous

for the APP^{V717F} mutation, there was significantly reduced LDL endocytosis after 4 hours (**Figure 3-11A**) and this defect was rescued by β-secretase inhibition (**Figure 3-11A**). Similar to both the $PS1^{\Delta E9}$ and APP^{V717F} mutations, neurons homozygous for the APP^{swe} mutation also exhibited decreased LDL endocytosis (**Figure 3-11B**). In contrast to the other FAD mutations, β-secretase inhibition in the APP^{swe} neurons did not rescue the LDL endocytosis defect. However, mutant APP Swedish protein has previously been reported to decrease the potency of β-secretase inhibitors (Yamakawa et al., 2009), which could explain why in our study β-secretase inhibition did not rescue the APP^{swe} neurons. These findings demonstrate that the reduction in LDL endocytosis is not specific to the $PS1^{\Delta E9}$ mutation but is a phenotype common to other FAD mutations.

3.4 Discussion

Here we demonstrate that in human neurons with endogenous expression of fAD mutations increased β-CTF alters the subcellular localization of APP, the distribution of Rab11, and decrease endocytosis and transcytosis of APP and LDL through a common mechanism. The β-CTF induces reduced LDL endocytosis and transcytosis at least in part by impairing recycling of LRP1. These defects are rescued by β-Secretase inhibition. Our results show that impaired LDL endocytosis is present in multiple forms of FAD. The observation that the major risk factor for sAD is E4 allele of APOE, the major brain cholesterol carrier, raises the possibility that lipoprotein transcytosis defects could be a

common defect present in multiple fAD and sAD forms. Epidemiologic evidence implicating cholesterol as a major player in AD also dovetails with these molecular and cellular findings (reviewed in Fonseca et al., 2010; Wolozin, 2004).

We demonstrate that β-CTFs cause impaired LDL uptake by reducing recycling of LDL receptors back to the cell surface. One possible mechanism is that β-CTFs bind to LRP1 (Kounnas et al., 1995; Pietrzik et al., 2002), and retain LRP1 in a Rab11 containing compartment until the β-CTF is cleaved by γ-secretase. This idea would explain why γ-secretase inhibition impairs LDL uptake and why that defect can be rescued by β-Secretase inhibition. Another intriguing possibility is that APP, through its C-terminal domain, acts as a cholesterol sensing protein (Beel et al., 2010; Song et al., 2013). There is ample evidence linking elevated cholesterol levels with increased association of APP and β-CTFs to lipid rafts thus favoring amyloidogenic processing of APP (Beel et al., 2010; Bodovitz and Klein, 1996; Guardia-Laguarta et al., 2010; Grimm et al., 2008; Kojro et al., 2001; Simons et al., 1998; Wahrle et al., 2002). The finding that β-CTFs favors binding to cholesterol over homodimerization suggests that elevated levels of β-CTFs can drive retention of cholesterol in membrane-bound structures mimicking a cholesterol enriched state (Beel et al., 2010). This state could drive a negative feedback loop whereby high levels of APP or the proteolytic products of amyloidogenic APP processing, Aβ, β-CTFs, and AICD, downregulate intracellular cholesterol uptake, biosynthesis, and turnover.(Pierrot et al., 2013).

Neurons are dependent on uptake of extracellular cholesterol from lipoprotein particles to perform functions such as axon elongation and synapse formation and maintenance (Barres and Smith, 2001; Lane-Donovan et al., 2014; Mauch et al., 2001; Nägler et al., 2001; Pfrieger, 2003; Pierrot et al., 2013). In fact, glia-derived cholesterol was reported to enhance synaptogenesis of adult rat CNS (Mauch et al., 2001; Nägler et al., 2001) suggesting that a defect in endocytosis and transcytosis of extracellularly-derived cholesterol could have long-term functional consequences leading to impaired neurotransmitter release and synaptic function. Therefore the defects in LDL endocytosis and transcytosis described here for multiple fAD mutations could contribute to a wide array of phenotypes that have been associated with AD. For instance, the most consistently identified risk factor for sAD is the e4 allele of APOE, which confers the strongest risk for developing SAD (reviewed in Bertram et al., 2010). Though many studies of APOE function have focused on its potential role in mediating Aβ clearance, APOE has also been identified as the major lipoprotein carrier in the brain and the e4 allele is less efficient in transporting brain cholesterol (Liu et al., 2012). Interestingly, post-mortem studies comparing sAD patients to age-matched controls found that brain cholesterol levels are reduced in the areas of learning and memory, the hippocampus and cortex (Svennerholm and Gottfries, 1994).

Our finding that the reduction in LDL endocytosis and transyctosis is common to multiple fAD mutations that increase β-CTFs suggests that therapies

should be focused on reducing these toxic APP fragments in addition to amyloid-β and/or modulating cholesterol homeostasis. Furthermore, the common impairment in axonal delivery of cholesterol has far-reaching consequences for maintenance of proper synaptic function and could explain why AD neurons exhibit multiple axonal defects associated with neurodegeneration.

3.5 Acknowledgements

Chapter 3 contains parts of a manuscript currently being prepared for submission. Reyna, S.M.* and Woodruff, G.*, Santos dos Chaves, R., Dunlap, M., Goldstein, L.S.B. “Reduced Endocytosis and Transcytosis of APP and Lipoproteins Owing to Accumulation of β-CTF Fragments in Familial Alzheimer’s Disease Mutations.” The dissertation author was a co-primary investigator and author of this paper.

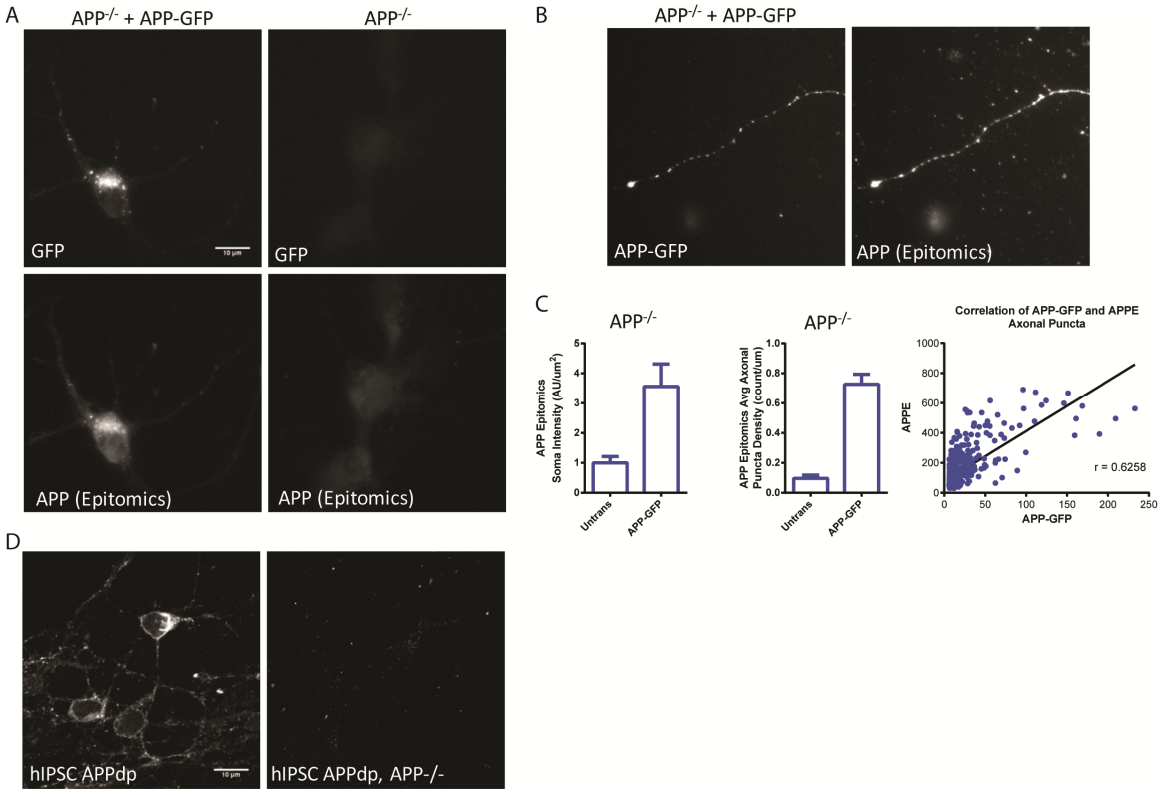

Figure 3-1 APP Epitomics Antibody is Specific to APP
A) APP$^{-/-}$ mouse neurons were stained with the APP Epitomics Y188 antibody with and without overexpression of an APP-GFP plasmid. Note the almost complete absence of APP staining in the untransfected cells and the extremely similar staining pattern of the APP-GFP and APP Epitomics stains. B) An example of axonal APP staining in APP$^{-/-}$ cells overexpressing APP-GFP and stained for APP Epitomics. Again, note the strongly similar distribution pattern. C) Quantification of APP Epitomics soma intensity from A and axonal APP Epitomics density in APP$^{-/-}$ untransfected and APP-GFP transfected cells. The third inset shows the strong correlation of axonal puncta APP-GFP and APP Epitomics intensities. D) APP Epitomics staining in hIPSC-derived neurons from an APP duplication patient and in a corresponding isogenic APP$^{-/-}$ clone.

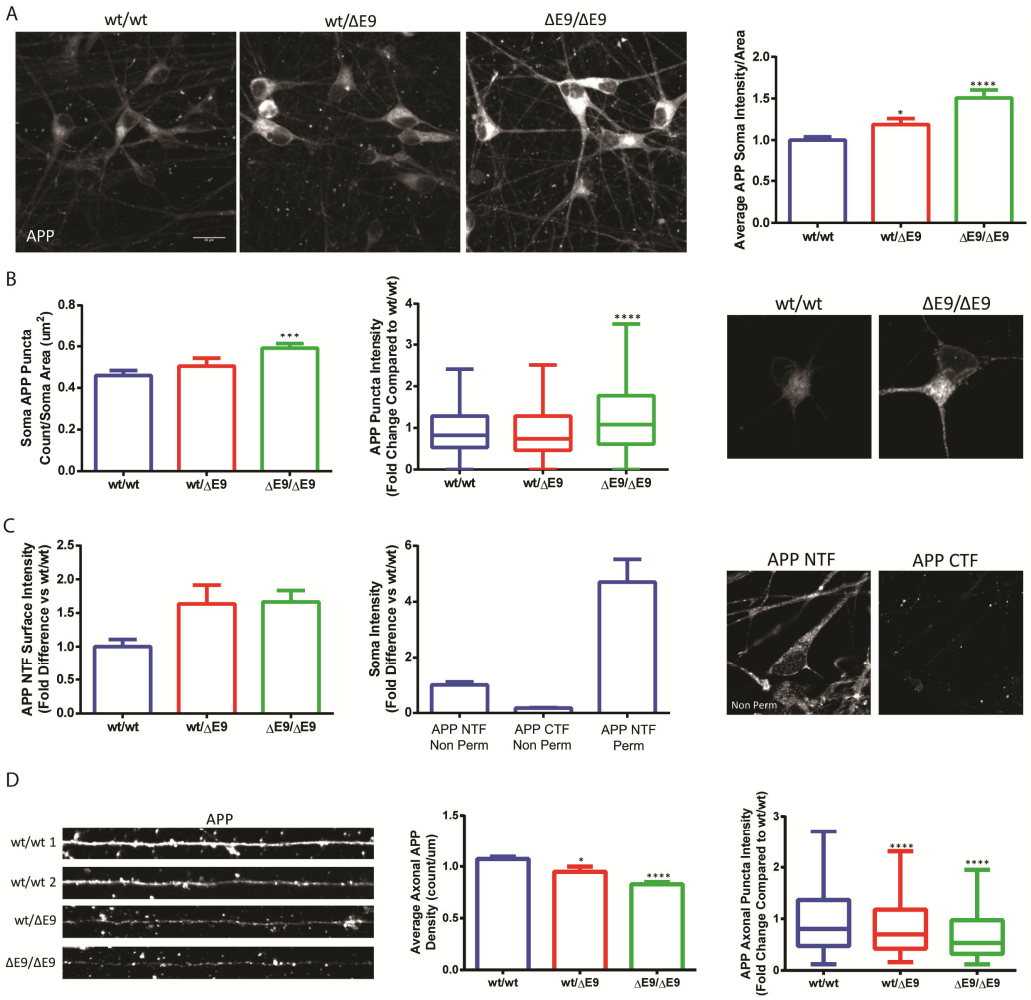

Figure 3-2 PS1$^{\Delta E9}$ hIPSC-derived neurons exhibit altered sub-cellular distribution of APP
Purified iPSC-derived neurons were stained with a C-terminal APP antibody (Epitomics) and imaged for analysis. A) PS1$^{\Delta E9}$ neurons have a gene-dose dependent increase in soma APP intensity. Data represent a total of 5 immunofluorescence experiments from 5 differentiations. (Soma counts: wt/wt: 113; wt/ΔE9: 59; ΔE9/ΔE9: 109) B) High magnification analysis of APP puncta indicate that the increase in soma intensity is a combination of increased puncta counts and individual puncta intensity. Data represent 3 immunofluorescence experiments and over 4000 puncta per genotype. C) To evaluate surface APP, an antibody targeting the N-terminus of APP was used to probe unpermeabalized purified neurons. Surface intensity of APP is increased in PS1$^{wt/\Delta E9}$and PS1$^{\Delta E9/\Delta E9}$ neurons compared to PS1$^{wt/wt}$. As a permeabilization control, PS1$^{wt/wt}$ neurons were also stained with an antibody targeting the intracellular C-terminus of APP. PS1$^{wt/wt}$ neurons exhibited minimal CTF staining in unpermeabilized cells and dramatically increased NTF staining when permeabilized. D) To evaluate axonal APP levels, axons from differentiated NPCs grown in microfluidic devices were stained with APP CTF antibody and imaged. Average density and individual puncta intensities were decreased in a gene-dose dependent manner in PS1$^{\Delta E9}$ axons. Data represent the pooled values of 3 immunofluorescence experiments and 2 NPC lines per genotype. wt/wt: 160 axons, 14238 puncta; wt/ΔE9: 36 axons, 2902 puncta; ΔE9/ΔE9: 161 axons, 10273 puncta.

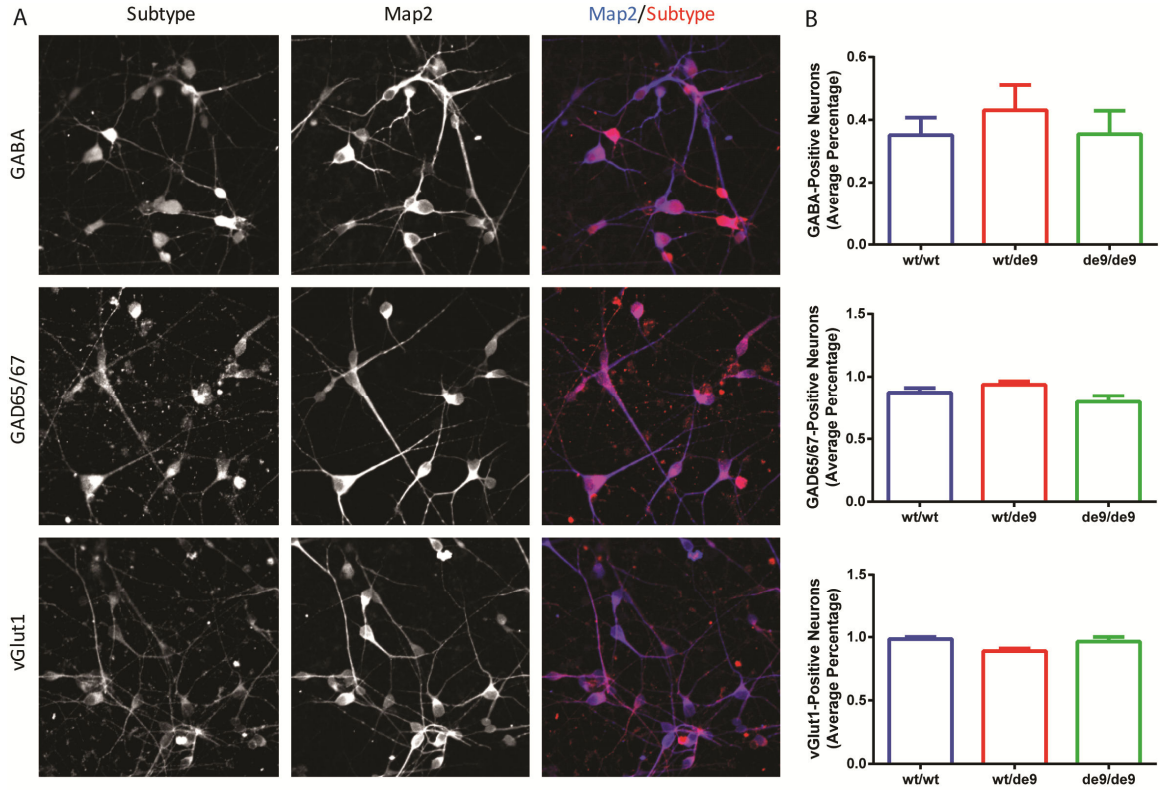

Figure 3-3 Neuronal Subtype Quantification in hIPSC-Derived PS1 Genotypes
A) Examples of purified neurons stained with Map2 and GABA, GAD65/67, or vGlut1. B) Quantification of neuronal subtype percentages. Data represent the average of 2 NPC lines per genotype, 2 differentiations, and multiple wells per differentiation.

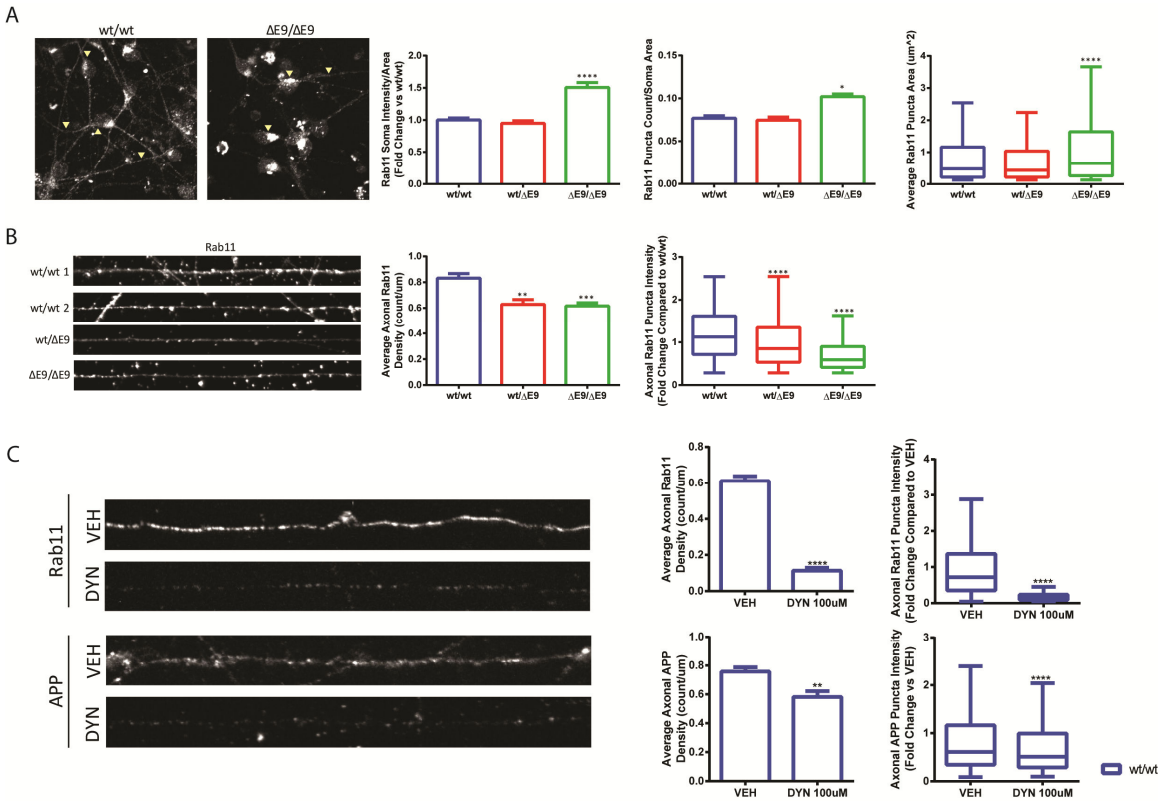

Figure 3-4 PS1$^{\Delta E9/\Delta E9}$ neurons exhibit altered Rab11 distribution

Purified iPS-derived neurons were grown in 384 well imaging plates for 1 week after sorting and stained for Rab11a. A) While PS1$^{wt/wt}$ neurons exhibited distinct punctate pattern of Rab11 staining in soma, PS1$^{\Delta E9/\Delta E9}$ neurons had a marked accumulation of Rab11 in soma (arrows). Quantification of staining showed that soma Rab11 intensity, puncta count, and puncta area were all significantly increased in PS1$^{\Delta E9/\Delta E9}$ neurons (wt/wt: 87 neurons, 1099 puncta; wt/ΔE9: 79 neurons, 961 puncta; ΔE9/ΔE9: 62 neurons, 902 puncta). B) For quantification of Rab11 in axons, a purified population of axons was obtained by growing differentiated NPCs in microfluidic devices and stained for axonal Rab11a. Quantification of Rab11a staining in axons showed that Rab11 density and puncta intensity were reduced in a dose-dependent manner. (wt/wt: 57 images, 7373 puncta; wt/ΔE9: 33 images, 5312 puncta; ΔE9/ΔE9: 41 images, 5144 puncta). C) To estimate the percentage of Rab11 and APP in axons derived from transcytosis, PS1$^{wt/wt}$ were treated with the dynamin inhibitor 100uM Dynasore for 24 hours and subsequently stained for Rab11 and APP CTF. Inhibition of soma endocytosis resulted in almost complete ablation of axonal Rab11 density (first inset) and approximately a 20% decrease in APP density (second inset).

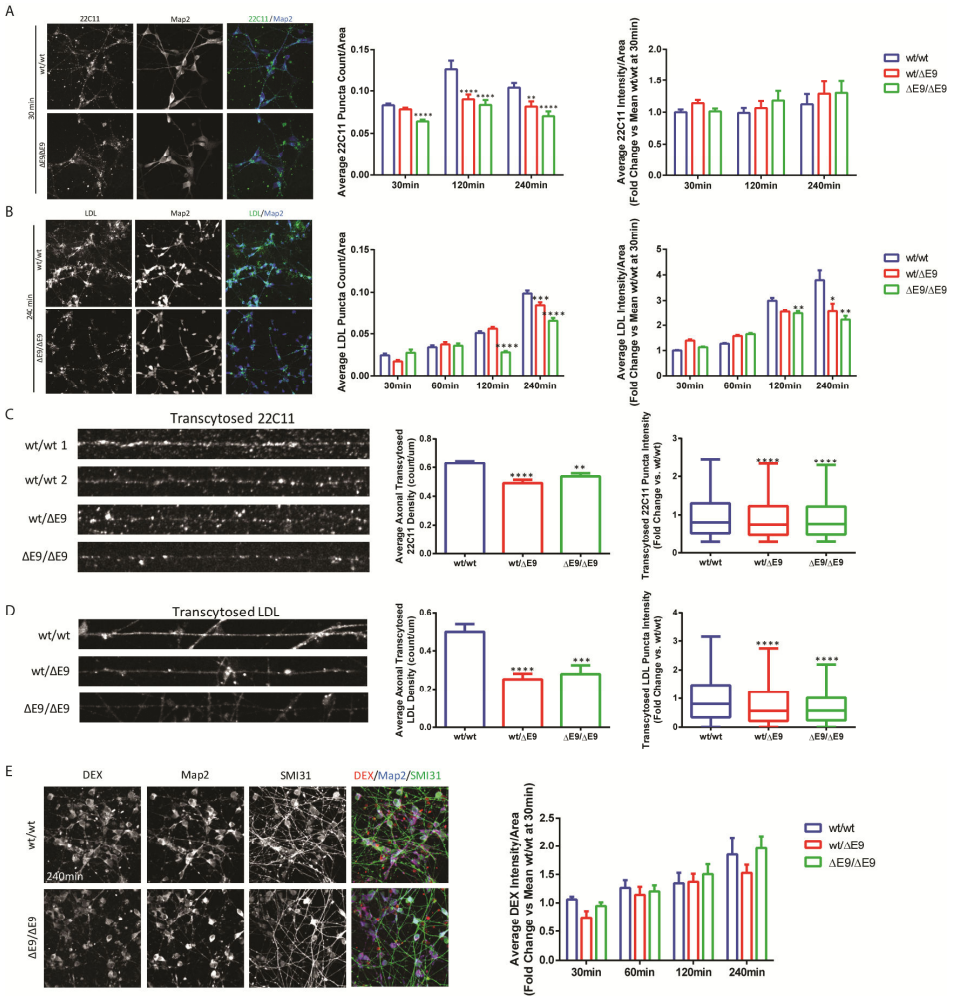

Figure 3-5 PS1 ΔE9 Neurons have Reduced Endocytosis and Transcytosis of APP and LDL
A) Example images of internalization of APP 22C11 antibody at 30 minutes in $PS1^{wt/wt}$ and $PS1^{\Delta E9/\Delta E9}$ neurons. Bar graphs depict average APP puncta count and average intensity normalized to cell area at time 30min, 120min, and 240min. B) Example images of LDL-Bodipy labeling at 240min in $PS1^{wt/wt}$ and $PS1^{\Delta E9/\Delta E9}$ neurons, with intensity adjusted so that puncta are clearly visible in the $PS1^{\Delta E9/\Delta E9}$ neurons. Graphs depict quantification of LDL puncta count and intensity normalized to cell area at 30min, 60min, 120min, and 240min of LDL uptake. As evidenced, $PS1^{wt/\Delta E9}$ and $PS1^{\Delta E9/\Delta E9}$ neurons have reduced APP and LDL soma endocytosis, with the LDL effect appearing most prominently at 240min. C and D) differentiated NPCs were grown in microfluidic devices and then allowed to internalized either APP antibody (C) or LDL-Bodipy (D) on the soma side with the axons in fluidic isolation. Then axons that passed through the channels were imaged and puncta densities and intensities were evaluated. E) Example images and a graph of intensity quantification are depicted for endocytosis of the fluid phase fixable marker, Dextran-TetramethylRhodamine. Dextran was added to purified neurons and allowed to internalize for 30min, 60min, 120min, and 240min. Bulk endocytosis was not different in $PS1^{\Delta E9/\Delta E9}$ neurons.

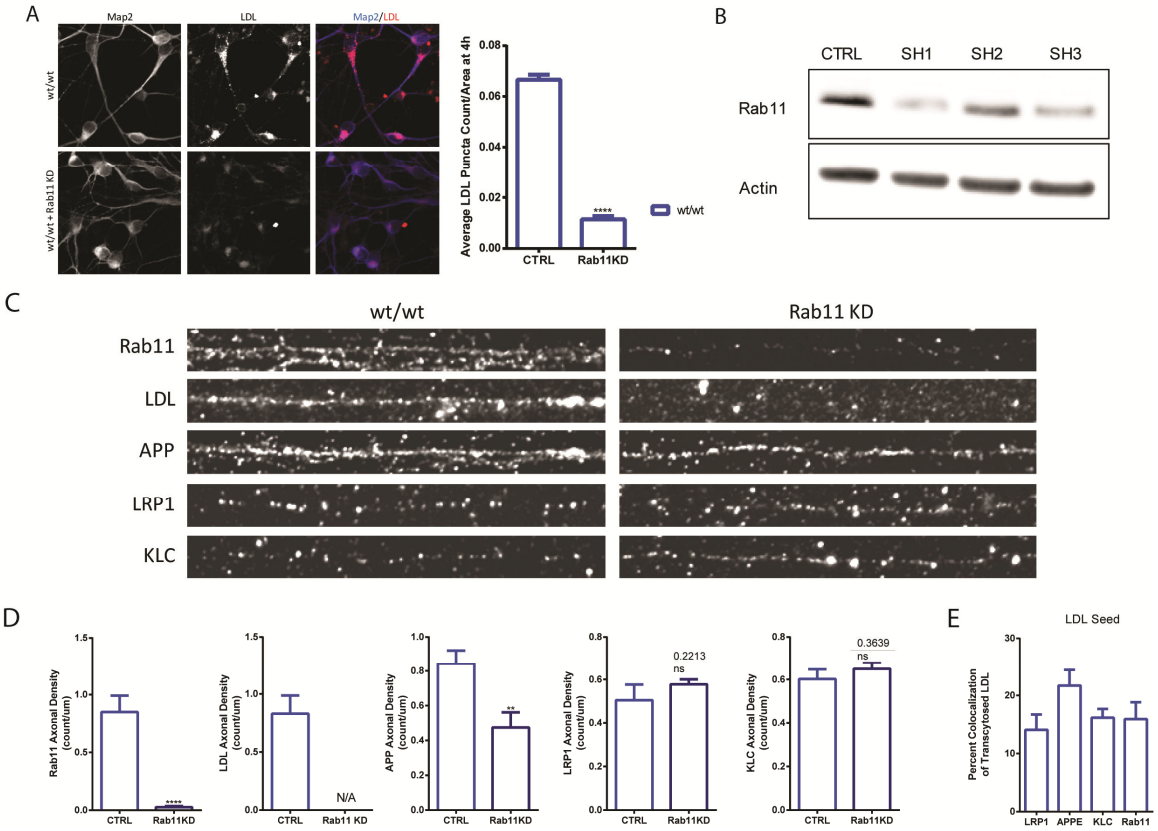

Figure 3-6 Rab11 Mediates Transcytosis of LDL

A) Wildtype neurons were transduced with lentivirus containing control (ctrl) or Rab11 shRNA and then treated with LDL for 4 hours. B) Western blot of cells transduced with control (CTRL) or one of 3 different Rab11 shRNAs. C) $PS1^{wt/wt}$ axons and $PS1^{wt/wt}$ axons with Rab11 knockdown and co-stains. D) Vesicle densities of Rab11, LDL, APP, LRP1 and KLC1 under control and Rab11 knockdown conditions. E) LDL vesicle colocalization with LRP1, APP, KLC and Rab11.

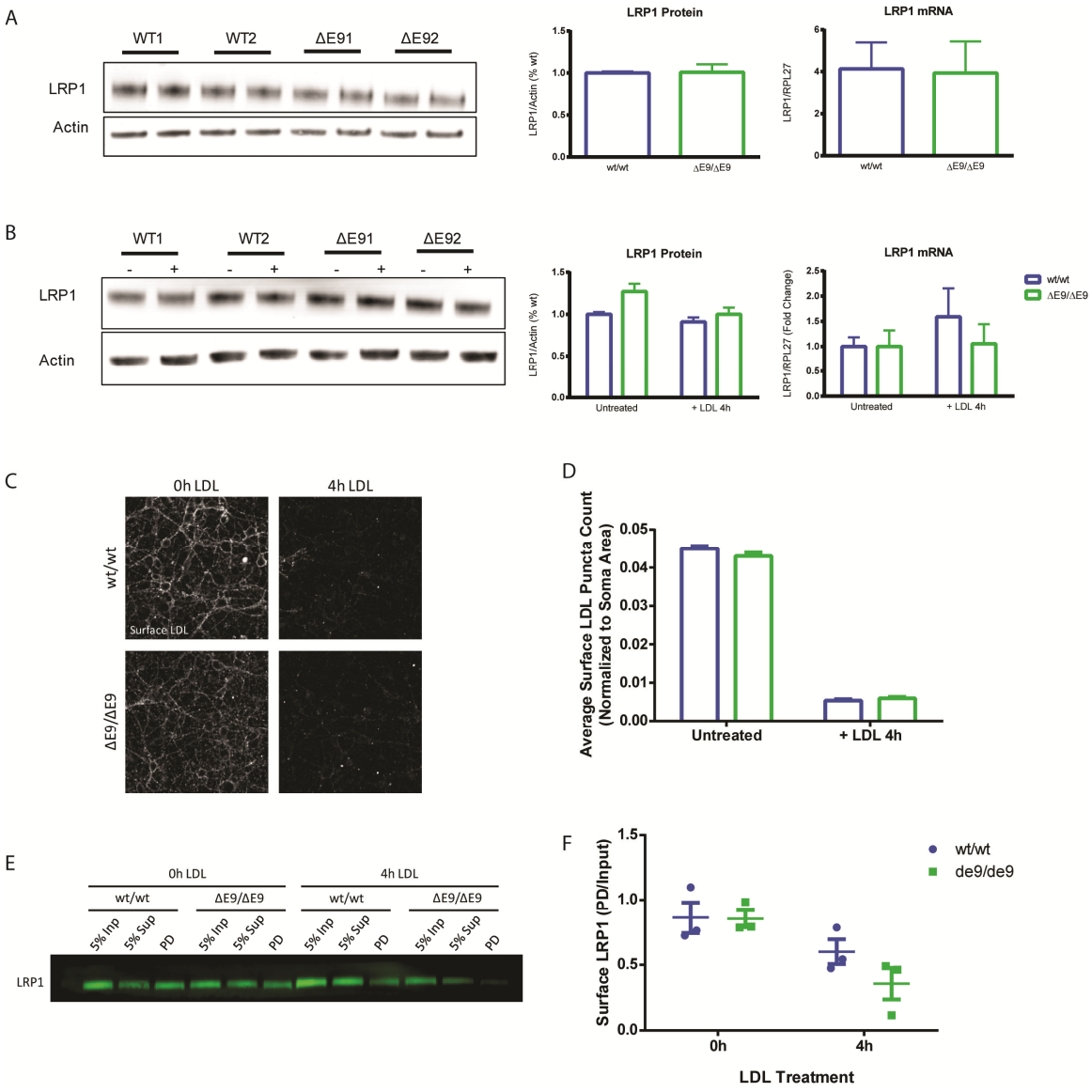

Figure 3-7 LRP1 Surface Recycling is Reduced in PS1$^{\Delta E9/\Delta E9}$ After 4h LDL Treatment.
A) Purified neurons were harvested and LRP1 protein and mRNA levels were measured. PS1$^{\Delta E9}$ LRP1 levels were not different at baseline. B) LRP1 protein and mRNA levels were measured after purified neurons were treated with LDL for 4 hours. PS1$^{\Delta E9}$ LRP1 levels were not different after 4h LDL treatment. C) To measure surface LDL labeling and recycilng, purified neurons were left untreated or treated with 12.5ug/ml of unlabeled LDL for 4h. At the end of 4h, purified neurons were incubated with LDL-DiI for 30 minutes at 4C to label surface LDL receptors. Neurons were then fixed and puncta counts were evaluated in unpermeabilized cells. Surface LDL levels were not different in PS1$^{\Delta E9}$ neurons. D) Differentiated NPCs were treated with a cell impermeant Biotin for 30 minutes at 4C with and without pre-treatment with 4h LDL. Streptavidin beads were then used to pull down biotinylated surface proteins and run on a gel. For comparison, 5% of input and 5% of supernatant are depicted. As evidenced, PS1$^{\Delta E9/\Delta E9}$ LRP1 surface levels were not different at baseline, but were markedly diminished compared to PS1$^{wt/wt}$ after 4 hours LDL treatment, indicating diminished LDL-induced recycling of LRP1 back to the surface.

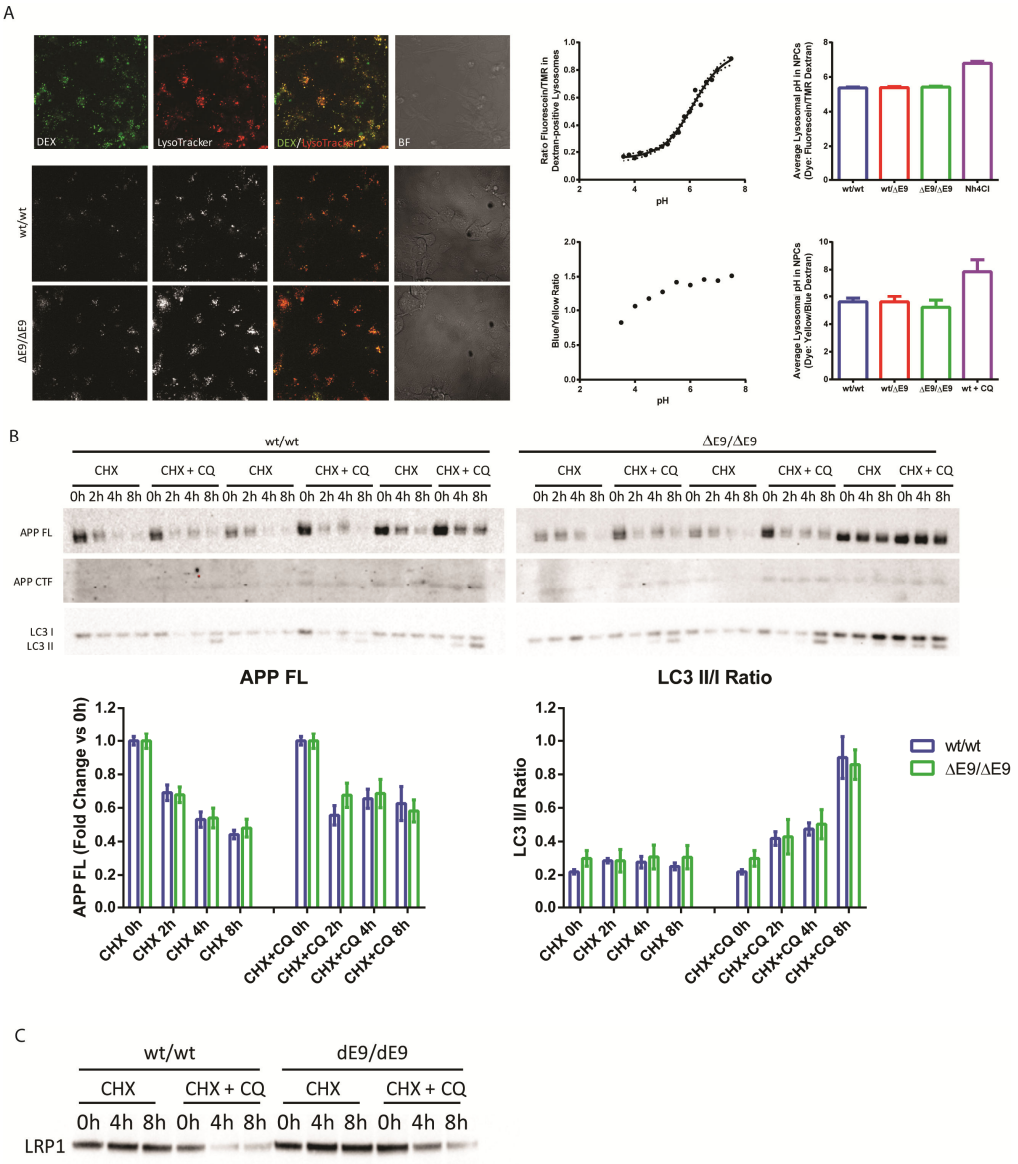

Figure 3-8 PS1$^{\Delta E9}$ Mutations do not have Altered Lysosomal pH, Protein Degradation, or Autophagy Activation

A) PS1$^{\Delta E9}$ NPCs were incubated with Fl/TMR Dextran or Lysosensor Yellow/Blue Dextran to label lysosomes. Example images of Fl/TMR Dextran are shown. Lysosomal pH was measured using these ratiometric probes and plotting the experimental values on a standard curve (shown in graphs). Data represent multiple NPC lines per genotype, multiple experiments, and many wells. B) NPCs were differentiated for 5 weeks and then treated with cycloheximide (CHX) with and without chloroquine (CQ) for the indicated times. Samples were harvested and run on a Western and probed for APP and LC3. As evidenced, neither APP degradation or LC3 II/I ratio (a measure of autophagy activation) were different in PS1$^{\Delta E9}$ dNPCs. C) LRP1 is not degraded in the time points analyzed.

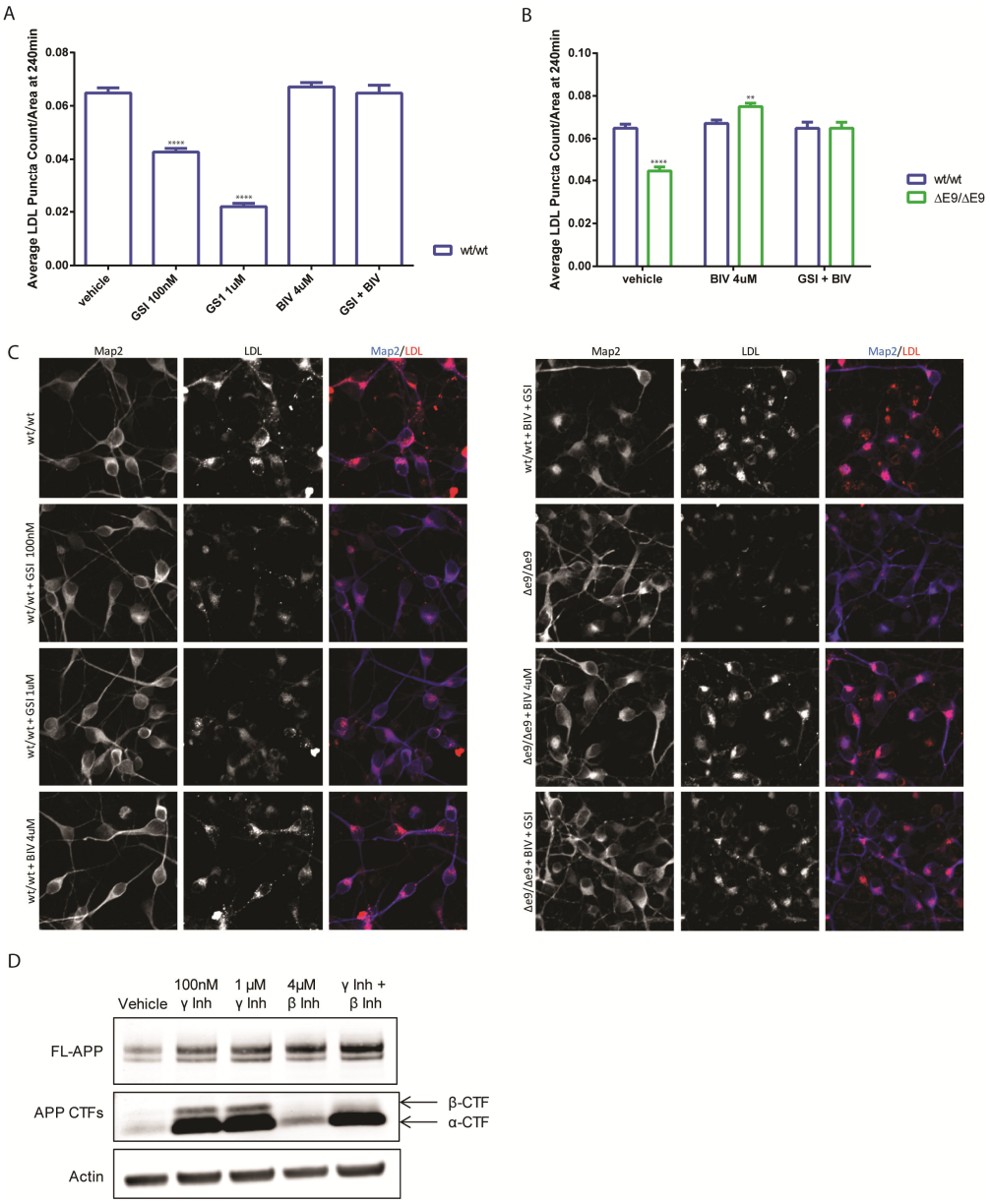

Figure 3-9 β-CTF Levels Inversely Affect LDL Uptake in Purified Human Neurons
A) Quantification of LDL puncta counts in 4 hour LDL-treated PS1$^{wt/wt}$ neurons. Treatment with a γ-secretase inhibitor (GSI) resulted in a dose-dependent decrease in LDL endocytosis in PS1$^{wt/wt}$ neurons, while treatment with a β-secretase inhibitor (BIV) had no effect. Notably, combining GSI and BIV did not result in reduced internalization of LDL. B) When β-CTF levels were ablated in PS1$^{ΔE9/ΔE9}$ neurons treated with a BIV, the reduction in LDL internalization at 4 hours was rescued to PS1$^{wt/wt}$ levels. Importantly, LDL endocytosis is rescued even in the presence of high levels α-CTFs when β-CTFs are reduced (GSI + BIV). Data represent 2 NPC lines per genotype, multiple wells, 2 separate experiments, and hundreds of neuronal soma. C) Example images for 5A and 5B. D) Example Western blot of neurons treated with the pharmacological modulators used in 3A-C. α-CTFs and β-CTFs are indicated by arrows.

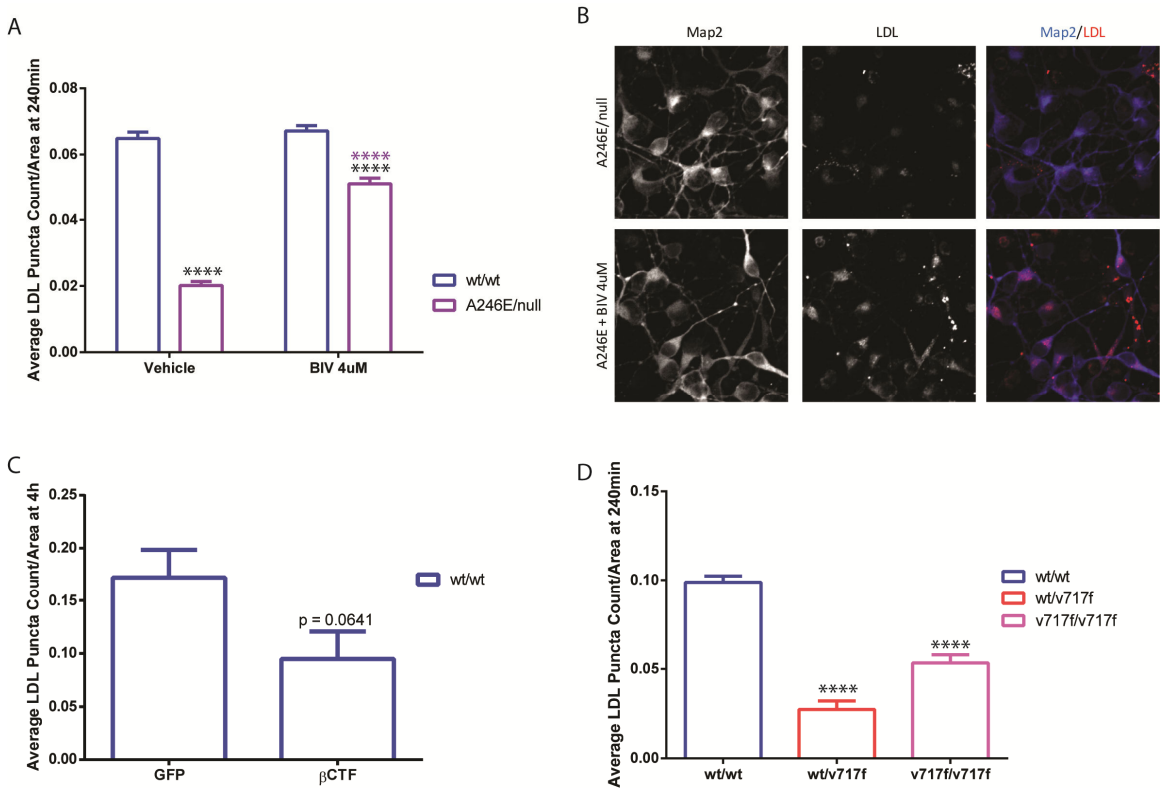

Figure 3-10 LDL Endocytosis is Reduced in hIPSC-Derived Neurons with Increased Levels of βCTF

A) PS1$^{A246E/null}$ mutants show reduced LDL uptake at 4h, which is partially rescued by 4h pre-treatment with 4uM BIV. B) Example LDL uptake images from PS1$^{A246E/null}$ with and without 4uM BIV. C) Purified neurons transfected with βCTF (C99-EGFP) exhibit a trend toward reduced LDL internalization at 4h. (n=1 experiment) D) hIPSC-derived neurons with APP^{V717F} mutations also exhibit reduced LDL endocytosis at 4h.

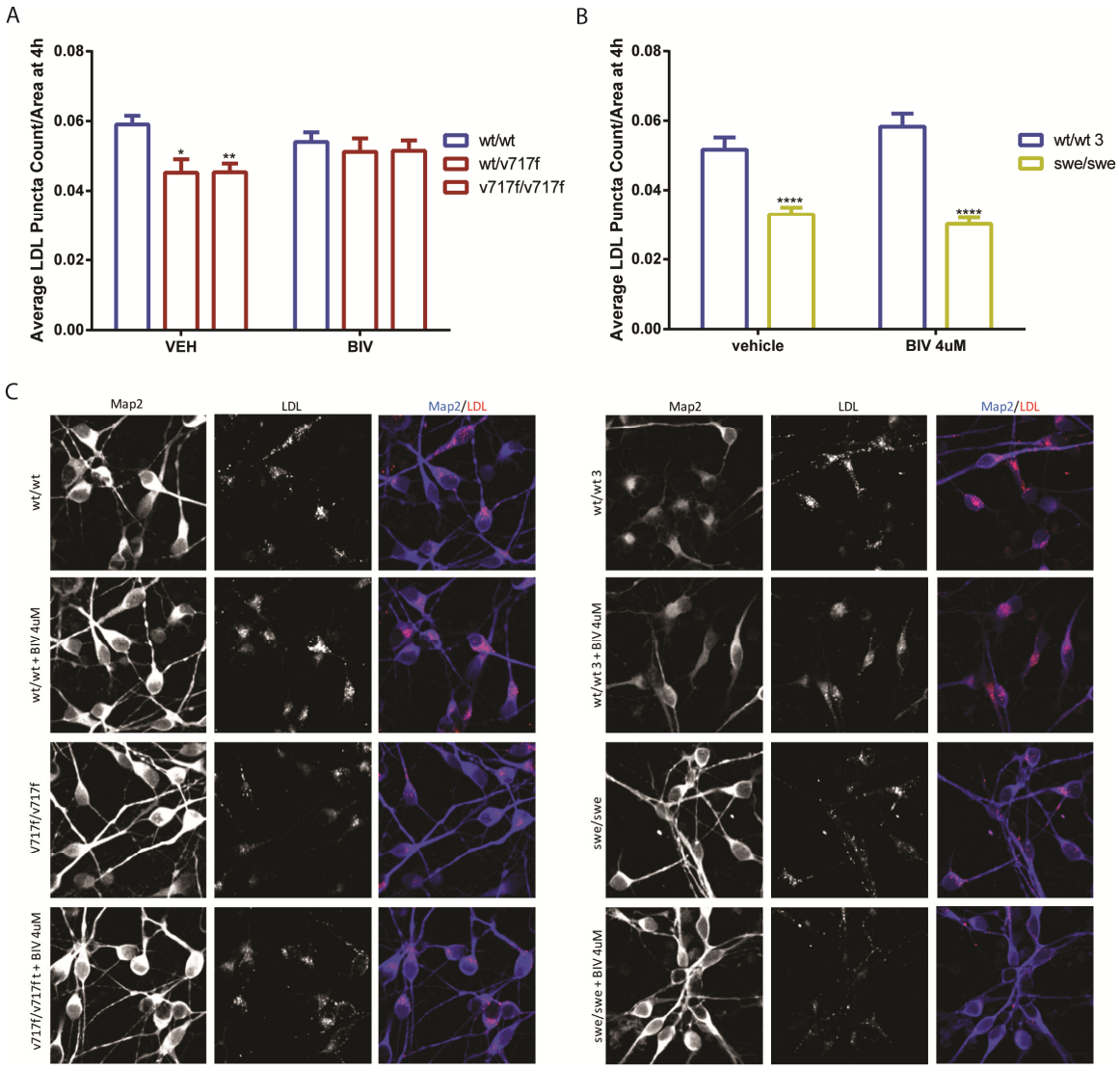

Figure 3-11 LDL Endocytosis is Reduced in APP fAD Mutations at 4 Hours
A) Quantification of LDL puncta count after 4 hours of LDL treatment in $APP^{wt/wt}$ $APP^{wt/V717F}$ and $APP^{V717F/V717F}$ neurons with vehicle and β-secretase inhibitor treatment (BIV). B) Quantification of LDL puncta count after 4 hours of LDL treatment $APP^{wt/wt}$ and $APP^{swe/swe}$ neurons with vehicle or β-secretase inhibitor.

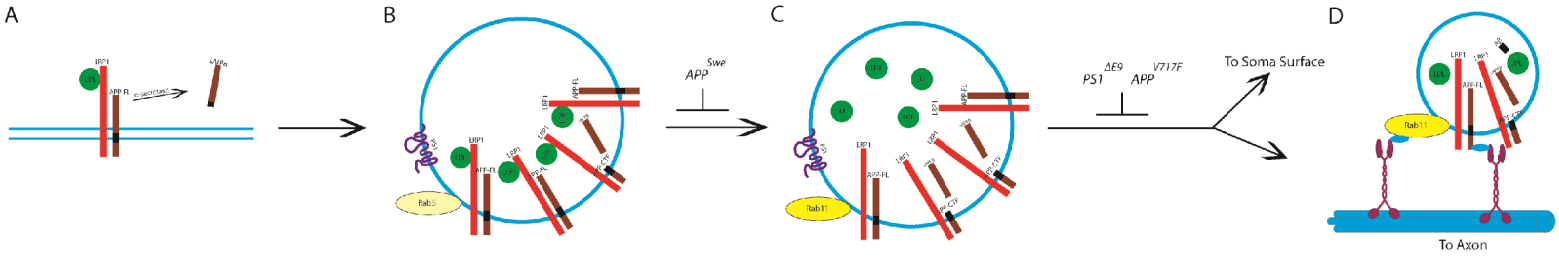

Figure 3-12 Model

A) Neuronal FL-APP at the cell surface can be cleaved by α-secretase or can undergo endocytosis along with other proteins such as LRP1, which is a primary receptor for LDL. B) FL-APP is internalized in Rab5+ sorting endosomes that contain LDL associated with LRP1 and possibly PS1. C) As vesicles become more acidic along the endocytic pathway, LDL dissociates from LRP1 and FL-APP gets cleaved by β-Secretase. A proportion of the cleaved APP population resides in Rab11+ endosomes containing LRP1, β-CTF and LDL. D) When β-CTF gets cleaved by γ-secretase, LRP1 can be recycled back to cell surface and transcytosis of LDL and FL-APP to the axon can occur. FAD mutations increase β-CTFs, which impairs recycling of LRP1 and decreases transcytosis, possibly by directly sequestering LRP1 in a Rab11+ endosome.

4. Elucidating Axonal Transport Dynamics of AD-Relevant Cargo in Wild-Type hIPSC-Derived Neurons

Abstract

A hallmark of the polarized structure of a neuron is it long thin axon where a wide variety of cargo essential for proper neuronal viability must be transported correctly to and from the axon terminal. Perturbations of this complex neuronal process can have drastic effects and, in fact, there is a long-standing proposal in the Alzheimer's Disease (AD) field that impairments in axonal transport are involved in the pathogenesis of disease. Given the infancy of the hIPSC-derived neuronal system, ensuring that axonal transport of cargo is happening normally is necessary. In this chapter, computational methods and results of axonal transport of AD-relevant cargo in wild-type hIPSC-derived neurons is described. Importantly, we report that hIPSC-derived neurons transport cargo similar to other systems. Namely, axonal APP undergoes predominantly anterograde fast axonal tranpsort, axonal Rab5a is predominantly stationary and when motile exhibits primarily reversing movement behavior, and Lysotracker vesicles demonstrate a retrograde direction bias with frequent reversals. BACE1 and mitochondria, however, do not demonstrate a preference for directionality and move at speeds similar to other previously reported studies.

4.1 Introduction

A hallmark of the polarized structure of a neuron is it long thin axon where a wide variety of cargo essential for proper neuronal viability must be transported correctly to and from the axon terminal (Grafstein and Forman, 1980). Perturbations of this complex neuronal process can have drastic effects and, in fact, a number of neurological diseases are associated with transport defects (Chevalier-Larsen and Holzbaur, 2006; Stokin and Goldstein, 2006a, 2006b). Studies of axonal transport in neurological diseases have largely been done in animal models or humanized neuronal cell lines, which in many cases fail to fully recapitulate human disease. In the case of Alzheimer's Disease (AD), for example, some mouse models develop the characteristic Aβ plaques, but do not exhibit typical human features such as neuronal cell death and neurofibrillary tangles (Balducci and Forloni, 2011; Braidy et al., 2012; Goldstein et al., 2014). A further complication is that most mouse models and human neuronal cell lines employ overexpression of tagged proteins to study transport, and most cultured cell models are aneuploid with unknown variations in the number of gene copies. Since even one extra copy of amyloid precursor protein (APP) is sufficient to generate AD (APP duplications and Down's Syndrome with Trisomy 21), control of gene dosage is necessary and a human, euploid cell culture model could be very powerful.

To that end, a number of investigators have sought to capitalize on the genetic power of iPS-derived neurons to study complex human neurological

diseases such as AD, Amyloid trophic lateral sclerosis (ALS), Autism Spectrum Disorders (ASDs), Parkinson's Disease (PD), among others (Goldstein et al., 2014; Hargus et al., 2014; Inoue, 2010; Payne et al., 2015). Among the various papers, there is evidence that the neurons that are generated are compartmentalized appropriately with somatodendritic and axonal compartments, and that the neurons are capable of mounting action potentials. Many of these groups have, to varying degrees, characterized their electrophysiological properties, subtypes, maturity, and synaptic contact formations, but extensive characterization of axonal transport dynamics in iPS-derived neurons is missing. In fact, published axonal transport from iPS-derived neurons is limited to studies of mitochondrial motility using Invitrogen Mitotracker dyes or MitoDsRed (Denton et al., 2014; Saporta et al., 2015). Considering the wide variety of neuronal axonal cargo, further experiments demonstrating that iPS-derived neurons transport cargo effectively and similarly to other experimental models is needed.

Broadly speaking, axonal transport is driven by molecular motors that move on polarized microtubules in two directions. Anterograde transport, toward the synapse, is mediated by a variety of plus-end directed kinesins (Goldstein and Yang, 2000; Hirokawa and Takemura, 2005). Conventional kinesin is a heterotetrametric protein composed of two heavy chains (KHC or KIF5) and light chain (KLC) subunits. The subunits can complex in various combinations to mediate the transport of a variety of cargo including lysosomes, mitochondria, endosomes, and even neurofilaments and tubulin (Gindhart et al., 1998). For

example, kinesin-1C complexed to homodimers KLC has been shown to be the predominant molecular motor involved in fast axonal transport (FAT) of APP (Brunholz et al., 2012; Ferreira et al., 1992; Szodorai et al., 2009; Yamazaki et al., 1995). KIF1b has been shown to colocalize with mitochondria (Nangaku et al., 1994) and its absence is associated with abnormal perinuclear clustering of mitochondria (Tanaka et al., 1998), while KIF1a may be involved in axonal delivery of select synaptic vesicles (Okada et al., 1995). While studies of β-secretase (BACE1) (one of the secretases involved in APP processing) anterograde transport are few, there are indications that BACE1 anterograde delivery is regulated by a kinesin-1-dependent mechanism (Kamal et al., 2000; Steuble et al., 2012). In addition, transport of lysosomes and autophagosomes have been shown to depend on KLC1, kinesin-1B, and kinesin-2 (Rosa-Ferreira and Munro, 2011). The molecular motor for Rab5, which is associated with early endosomes, has long been elusive, but a recent studies indicate that kinesin-3 is likely the processive motor driving Rab5 motility (Huckaba et al., 2011; Schuster et al., 2011).

Minus-end transport away from the synapse and toward the cell body is termed retrograde axonal transport and is mediated by the cytoplasmic motor protein dynein. While there are 5 kinesins exhibiting different cargo specificity and variations in tissue expression, it is thought that dynein is the predominant retrograde motor. Dynein is composed of six subunits: dynein heavy chain (DHC), intermediate chain (DIC), light-intermediate chain (DLIC), and 3 dynein

light chains (DLC). Each subunit of dynein is capable of multiple protein-protein interactions and, in addition, dynein requires an 11-subunit protein complex called dynactin for proper processive movement and helps dynein bind to more proteins (King and Schroer, 2000; Pfister et al., 2006; Schroer, 2004). Some of the axonally transported cargo that require dynein include APP, lysosomes, mitochondria, Rab5, and BACE1.

In this chapter, hIPSC-derived neurons from the Goldstein's lab wild-type line (derived from Craig Venter) were used to study baseline axonal transport dynamics in human neurons. Because our lab is interested in studying AD, we focused our experimental analysis on cargo whose impaired transport has been linked to neuronal dysfunction in AD. Namely, APP, BACE1, Rab5a, acidic organelles (Lysotracker-positive vesicles), and mitochondria.

Ensuring that human iPSC-derived neurons exhibit normal transport properties is necessary to perform proper studies of axonal transport dynamics in a human system. We report that human iPSC-derived neurons are properly polarized, demonstrate appropriate fast axonal transport, and exhibit cargo movement parameters similar to other model systems. Axonal APP undergoes predominantly anterograde FAT, axonal Rab5a is predominantly stationary and when motile exhibits primarily reversing movement behavior, and Lysotracker vesicles demonstrate a retrograde direction bias with frequent reversals. BACE1 and mitochondria, however, do not demonstrate a preference for directionality and move at speeds similar to other previously reported studies.

4.2 Methods

4.2.1 Establishing an Imaging Method to Track Transfected Cargo in hIPSC-Derived Neurons

In order to study the movement behavior of multiple axonally transported cargo, the simplest method was to transfect using traditional liposome-based methods such as Invitrogen's Lipofectamine. Similar to what's been observed with primary neuronal cultures, hIPSC-derived neurons are difficult to transfect and exhibit low transfection efficiency (~1%). Attempts to transfect purified neurons were unsuccessful because Lipofectamine leads to global neuronal death. Therefore, neural progenitor cells (NPCs) were induced to differentiate down a neuronal lineage **(see 3.2.1)** and cultured in 10cm plates for approximately 21 days. At this point, differentiated NPCs (dNPCs) were carefully dissociated and replated onto 35-mm imaging plates, allowed to settle and re-extend their axons. At day 5-7, 800 ng of plasmid constructs was introduced using Lipofectamine reagents. Lipofectamine 2000 was toxic to the neurons and exhibited a transfection efficiency of less than 1%. Because of this, Invitrogen's new Lipofectamine 3000 was utilized instead.

Lipofectamine 3000 was less toxic to the neurons and resulted in 1-5% neuronal transfection efficiency. While this is not conducive for studies of protein expression by Western blot, for imaging studies a relatively low transfection efficiency is ideal to properly identify neuronal axons. Since the replated dNPC culture has a variety of cell types including glia, NPCs, incompletely differentiated

NPCs, and “mystery” cells, strict criteria to identify neuronal axons were employed. Namely, in order to be selected for imaging, the cell had to exhibit morphology consistent with published neuronal data: 1) a small cell body with a single, long, thin primary axon that extended for at least 1-mm and 2) secondary, short, thick dendrites. Using strict criteria, it was easy to identify 8-10 axons from a single 35-mm imaging plate during a 30-min imaging window. Axonal transport movies were acquired at a distance of >500um from the cell body to exclude proximal and distal axonal regions (**Figure 4-1A**).

At this point, movies of cargo were acquired as specified in this chapter’s methods **(see Table 4-1)**. Directionality of cargo (anterograde vs retrograde) was determined by tracing the axon back to the soma. At this point, LapTrack, a previously published MATLAB based custom particle tracking software, was employed to quantify transport behavior (Gunawardena et al., 2013; Power et al., 2012; Reis et al., 2012). Because LapTrack requires that axon movies are straightened and imported with anterograde cargo moving left to right, a series of ImageJ programs were developed to facilitate movie processing and axonal straightening of batches of movies. First, **ZProject_Stacks** (see **Appendix**) was used to generate a folder of maximum intensity projections from another folder of movies (**Figure 4-1B, second inset**). Maximum intensity projection is a volume rendering method that turns a 3-dimensional image (in this case the third dimension is time) into a 2-dimension one by keeping the voxels with maximum intensity in each slice and projecting them onto a single plane. Using this

method, motile cargo appear as long streaks instead of as single puncta. This facilitated detection of axons where cargo moved at least 5 um during the imaging time. Axons that did not meet this criteria were likely unhealthy because of over-expression of the transfected construct and were excluded.

The maximum intensity projections were also used to help in the generation of axonal regions of interest (ROIs) (**Figure 4-1B, third inset**). ROIs were made in ImageJ's ROI Manager and saved an ROI folder as ".roi" files with the first point on the soma side of the axon and the last point at the axon terminus. The number of roi files has to correspond exactly with the number of movies in the Movie folder. Then, the program **StraightenTransfectedAxons** (see **Appendix**) was used to batch generate a series of straightened stack movies of 80 pixel thickness with anterograde cargo moving from left to right. The folder of straightened axons could now be loaded into Matlab's LAPTrack software and processed as previously described. This general approach was used to process and analyze APP, Rab5a, and BACE1 motility in human neurons obtained from hIPSC-derived dNPCs (**Figure 4-1C**).

Kymographs were automatically generated by LAPTrack software and tracks corresponding to vesicle movement were generated. From the saved tracks, a variety of different movement parameters could be determined per movie or per pooled data set. These parameters included means of segmental velocities, duration-weighted velocities, run lengths, pause frequencies, etc. (**see Table 4-2)**. All movement parameters including classification of vesicles as

anterograde, retrograde, reversing, and stationary were calculated as previously described (Reis et al., 2012). Briefly, vesicles were classified as stationary if their maximum deviation distance from the track center was less than 5.5 pixels or approximately 700 nm. Anterograde and retrograde cargo were those tracks that were not stationary and moved away from the cell body (right) or toward the cell body (left), respectively. Anterograde and retrograde cargo may or may not pause along their movement trajectory. Reversing cargo were defined as tracks that underwent at least one reversal with distance greater than 5.5 pixels or approximately 700 nm. Since most publications do not make include reversing cargo as an independent category, to compare with the published literature we report percent directionality of cargo with and without the reversing category. To plot duration-weighted velocities, box plots were generated in Prism with Tukey's distribution whiskers.

4.2.2 Establishing an Imaging Method for LifeTechnologies Trackers in hIPSC-Derived Neurons

In order to quantify motility of acidic organelles and mitochondria, we decided to employ LifeTechnologies's cell-permeable Lysotracker and Mitotracker dyes. Lysotracker and Mitotracker offer many advantages compared to plasmid transfections including the advantage that cell permeable dyes enter every cell at similar efficiencies thus allowing for more precise control of probe levels. Additionally, while plasmid transfections are always overexpressing their

product, which could have its own effects, Mitotracker and Lysotracker do not. Because the cell-permeable trackers enter every cell at similar efficiency, identifying single axons of a mass culture where directionality could be determined was very difficult. Because of this we decided to employ microfluidic devices to isolate axonal projections from a mass culture of dNPCs, as previously described (**Figure 4-2A**) (Niederst et al., 2015; Selfridge et al., 2015; Taylor et al., 2006).

The design employed in this study was developed in-house and produced by soft lithography using the biologically inert polymer polydimethylsiloxane (PDMS). Briefly, dNPCs were dissociated and replated on the soma side (3mm x 23mm x 10mm), and axons were allowed to extend through capillary channels (10μm x 3μm x 450μm) into the axonal space (3mm x 100μm x 39mm) **(Figure 4-2A).** We bonded PDMS microfluidic chambers onto glass imaging slides so that imaging could be done on an inverted microscope, directly in the compartments. It typically took 5-6 days to begin to see axons appear in the axonal space. At this point, we waited another 2-3 days until a sufficient number of axons had extended and were healthy enough to stain with Lystoracker or Mitotracker probes. Importantly, processes that extended into the axonal space were negative for the somatodendritic marker Map2 and positive for the neuronal process marker SMI31. SMI31 reacts with the phosphorylated epitope of phosphorylated neurofilament H and M, and has been shown to accurately stain thick and thin axons as well as dendrites **(Figure 4-2B).**

There are a number of different Lysotracker and Mitotracker options available with varying spectral emission patterns. To label acidic structures, we chose to use Lysotracker Red DND-99 because its fluorescent excitation and emission spectra are easily separated from GFP fluorescent plasmids and probes. In addition, the large, strongly acidic structures labeled with Lysotracker Red DND-99 are well-retained after aldehyde fixation (Invitrogen). To label mitochondria, Mitotracker Green FM was employed because it is non-fluorescent in aqueous solutions and, qualitatively, it photobleached less than other tested Mitotracker dyes. In keeping with published results, Lysotracker and Mitotracker probes require precise control of concentration since too much of the trackers can result in cytoxicity and reduced motility while too little leads to incomplete staining. Following a series of dilution experiments, we settled on 75 nM of Lysotracker Red DND-99 and 100 nM of Mitotracker Green FM. At these concentrations, the trackers were able to effectively label intracellular structures that exhibited proper movement behavior without causing cytotoxicity. Axons were incubated with tracker dyes for 30 min, washed twice with warm media, and imaged on a Nikon microscope with 5% CO2 at 37C.

In order to process videos, a similar protocol as that used for the plasmid-transfected experiments was employed. First, axons with motile trackers were identified by generating maximum intensity projections with **ZProject_Stacks.** The maximum intensity projections were also used to quantify the number of imaged axons that had visibly motile Lysotracker vesicles or mitochondria during

the imaging time (**Figure 4-2C, second inset**). After generating a folder of .roi files corresponding to axons with motile trackers, axons were straightened as above, imported into LAPTrack, and processed for movement behavior.

4.2.3 Evaluating the Size of Mitochondria and APP in hIPSC-Derived Neurons

Mitochondria exhibit dynamic movement behavior including frequent fission and fusion events, and impairments in these cellular processes have been associated with neurodegenerative diseases including AD, ALS, Charcot-Marie-Tooth disease, Hunting's Disease, Hereditary Spastic Paraplegia, Parkinson's Disease, and more (Schon and Przedborski, 2011). In addition to dynamic perturbations in fission/fusion, respiration, and motility, problems with the regulation of mitochondrial size are associated with pathogenesis of disease. Mitotracker Green FM has been used to evaluate mitochondria size (Agnello et al., 2008). In order to automate the quantification of mitochondrial size in the large data sets collected, an ImageJ Size Segmentation program was developed, named "**SizeInKymoAnalysis"**. Straightened movies are loaded into the program processed with the "Subtract Background" command in ImageJ to remove non-specific background fluorescence. In order to maintain the same size length of axon, movies are cropped by the same roi in a ROICrop folder. The same protocol was used to quantify APP-mCherry sizes.

From this cropped movie, a black and white mask is generated by

thresholding the 8-bit file. Mitochondria that are close together can be separated with the Watershed plugin in ImageJ. To identify structures, the Analyze Particles plugin was used, which employs the principles of binary images to find white structures (0) separated by black structures (1). Only structures greater than 0.1µm were analyzed and anything less than that was assumed to be noise or debris. To minimize the number of data points processed and to avoid overcounting structures, mitochondria in only three slices (30, 60, and 90) were analyzed. The final destination folder saves a copy of the black and white mask, a zip file of the mitochondria ROIs analyzed, a Summary text file with mitochondria counts per image (can be used for density analysis), and a Results text file with all the mitochondria size data.

4.3 Results

4.3.1 APP Axonal Transport in hIPSC-Derived Neurons

APP moves with an anterograde bias in hIPSC-derived *wt/wt* neurons with 25.5% stationary, 44.8% reversing, 21.5% anterograde and 8.2% retrograde events (without reversing events, 47.1% anterograde and 27.4% retrograde) **(See Figure 4-1F, Table 4-1)**. Mean anterograde duration-weighted segmental velocities were 1.385 ± 0.041 µm/sec, which were faster than values reported in *Drosophila* segmental nerve axons from our lab using similar imaging parameters (Gunawardena et al., 2013; Reis et al., 2012). Anterograde APP moved predominantly in long, uninterrupted tracks with long run lengths of 10.209 ±

0.382 μm and exhibited few pausing events at a frequency of 0.05 ± 0.002 counts/s (**Table 4-2**). Retrograde APP moved at slower speeds with mean duration-weighted velocity of 0.897 ± 0.023 μm/sec. Retrograde APP also had shorter run lengths of 5.03 ± 0.205 μm and a slightly higher pause frequency of 0.065 ± 0.003 counts/sec. For the most part, the data are consistent with the expected behavior of a kinesin-1-dependent, highly processive cargo with anterograde bias, as has been published for APP previously (see **4.4.1** for details).

APP sizes were analyzed as described in **4.2.3**. APP is transported in two seemingly distinct structures, as previously described: long tubules and single vesicles (Kaether et al., 2000). The length of the tubule is not correlated with speed (our unpublished results and Kaether et al., 2000) and, in fact, large tubules move very rapidly with an anterograde bias. Since the structures could be disease-relevant, we decided to quantify transfected APP size using the size segmentation program. We analyzed 1341 APP structures in *wt/wt* neurons from 2 control NPC lines, 104 movies, and 7 coverslips. The average size of APP structures in *wt/wt* neurons was 0.463 ± 0.011 μm^2 with 46.3% of structures exhibiting a size greater than 1.0 μm^2. A histogram of the APP size distribution is depicted in **Figure 4-3B**.

One additional piece of data that we serendipitously came upon during imaging was the convincing observation that the long tubular structures frequently seen in APP transport studies are actually composed of many vesicles

tethered together (**Figure 4-3C**). In a surprising video, an unusually long, anterograde-moving APP-mCherry vesicle moved into the imaging plane. At 12.0 seconds of imaging, the tubular structure paused and immediately split into 9 clearly distinct puncta, paused for ~2 seconds, and then continued moving in a long train (**Figure 4-3C** kymograph). These structures were originally described by the Dotti research group (Kaether et al., 2000). In the discussion, the authors speculate that the APP tubules may be formed due to a difference in size composition because of mechanical stress that forces them into a tubular shape or because of a difference in rigidity due to alterations in lipid and protein composition. These ideas are inconsistent with the movie depicted here (**Figure 4-3C**) and the observation that fixed axons stained with APP antibodies rarely show truly distinct, tubular APP structures. The apparent discrepancy between APP distribution in fixed samples and transfected axons can be easily explained if the tubular APP structures are simply trains of individual vesicles. When they're motile, it's easier to see them as a tubular structure because they move in unison, but once fixed the space between vesicles moving in a train can be resolved and the tubules look like individual puncta.

Taken together, the transport behavior of APP in hIPSC-derived neurons is consistent with published reports of *in vivo* APP transport and suggests that hIPSC-derived neurons can be used to study transport of cargo in a human background.

4.3.2 BACE1 Axonal Transport in hIPSC-Derived Neurons

In our hands, BACE1-mCherry transport in hIPSC-derived *wt/wt* neurons did not exhibit a directionality bias with 13.9% of vesicles moving anterogradely (35.3% without reversing), 13.2% retrogradely (34.4% without reversing), and 42.6% reversing (**Figure 4-1F**). BACE1 moved with mean anterograde duration-weighted segmental velocity of 0.775 ± 0.022 μm/sec and mean retrograde duration-weighted segmental velocity of 0.789 ± 0.021 μm/sec (**Table 4-2**). The spread of velocity distribution was narrower than APP velocities and was similar for both anterograde and retrograde BACE1 (**Figure 4-1G**). These velocities are in line with previously published reports though again there's a range of values depending on the acquisition parameters used (See **Table 4-1**).

4.3.3 Rab5a Axonal Transport in hIPSC-Derived Neurons

To study early endosome motility in axons, we chose to use transfected Rab5a-mCherry. Since Rab5 transport was not as fast as APP and BACE1, movie frame rate was adjusted to 2Hz to ensure sufficient motile events were captured. In keeping with a previous published report, axonal Rab5 was predominantly stationary (52.3% of vesicles) in the mid-axon and the motile vesicles exhibited short-range movements with few, if any, long-range transport (Deinhardt et al., 2006). Rab5 vesicles moved without a direction bias and with slow duration-weighted segmental velocities of 0.297 ± 0.009 μm/sec for anterograde and 0.297 ± 0.009 μm/sec for retrograde vesicles (**Figure 4-1G**).

4.3.4 Lysotracker Axonal Transport in hIPSC-Derived *wt/wt* Neurons

In *wt/wt* cells, 54.78 ± 0.05 of axons had visibly motile Lysotracker vesicles. This is likely because acidic vesicles are not particularly abundant in axons so at any given time a stretch of axon may be devoid of labeled puncta, but it is unlikely that 50% of axons are actually completely Lysotracker-negative. From the axons with motile Lysotracker, movies were generated and quantified with the LapTrack software. As seen in **Figure 4-2C**, Lysotracker vesicles exhibit frequent reversal and stationary events. The vesicles that moved uni-directionally had a retrograde bias such that 9.6% moved anterogradely and 19.1% moved retrogradely (**Figure 4-2E**). If the reversing population is excluded, the percentage of the anterograde population is 29.6% and that of the retrograde is 43.5%. This is consistent with published reports that indicate acidic vesicles initiate distally in axons and require long-range retrograde transport to acidify and mature (Fu et al., 2014; Maday et al., 2012). Duration-weighted segmental velocities were consistent with a retrograde bias such that anterograde vesicles moved at 0.48 ± 0.048 μm/sec and retrograde vesicles moved with a faster mean of 0.531 ± 0.038 μm/sec (**Figure 4-2F**). There are few reports of Lysotracker DND-99 movement in axons, but the velocities reported here are within the range of ~0.17-~0.95 μm/sec previously reported (Lee et al., 2010; Mar et al., 2014).

4.3.5 Mitotracker Axonal Transport in hIPSC-Derived *wt/wt* Neurons

In *wt/wt* cells, 49.05 ± 0.02 of axons had visibly motile Mitotracker-positive structures (henceforth called mitochondria). As with the Lysotracker experiments, this is likely a result of the imaging conditions and the relatively short distance of axon covered by the camera, though it's possible that a percentage of axons that grow through the channels of the microfluidic chamber are unhealthy/dead and the absence of motile mitochondria is simply an indication of mitochondrial health. Regardless, we were able to find 96 axons with motile mitochondria in the 2 *wt/wt* NPC lines employed for the experiments across three separate imaging experiments. Our detail population analysis indicates that 50.6% of mitochondria were stationary, 8.9% anterograde, 8.6% retrograde, and 31.9% reversing (**Figure 4-2E**). Simple population analysis indicated that the reversing population could be further subdivided such that 23.0% and 26.4% of mitochondria moved anterogradely and retrogradely, respectively. This is in line with reports indicating minimal direction bias of mitochondria in neuronal axons (Sheng, 2014).

Given the dynamic nature of mitochondria, it's no surprise that velocities exhibit large ranges with one publication reporting a range from 0.32-0.91 μm/sec (MacAskill and Kittler, 2010; Morris, 1995). In our hands, anterograde mitochondria moved at 0.207 ± 0.007 μm/sec and retrograde mitochondria moved at 0.257 ± 0.009 μm/sec **(Figure 4-2F**). This is slower than previously published results, possibly because Mitotracker dyes can interfere with proper mitochondrial respiration or because the axons were grown in microfluidic

devices, and the axons are not in contact with health-promoting glia. Further work to distinguish between these possibilities is ongoing.

Finally, we analyzed the size of 5349 mitochondria in *wt/wt* neurons as described in **4.2.3**. Mitochondria exhibit a wide range of sizes with a multi-modal distribution pattern. Bayesian Information Criterion (BIC) analysis was used to fit optimal distribution patterns with model-based clustering (Fraley, 2007). Using BIC, mitochondria in *wt/wt* neurons cluster in 6 different modes, depicted in cyan in **Figure 4-3A** and exhibit a mean size of 1.072 ± 0.014 μm, which is in line with previous reports (See **Table 4-2** for references).

4.4 Discussion

4.4.1 APP and BACE1 Axonal Transport in Human Neurons is Consistent with Behavior of Kinesin-1-Dependent Cargo

APP axonal transport has been extensively studied in a variety of different systems including *Drosphila* segmental nerves, mouse hippocampal neurons, mouse DRGs, mouse mixed cortical and hippocampal neurons, and rat cortical neurons (See **Table 4-1** for summary of literature). There is some variation in the imaging time (15-120 seconds) and frame rate capture (1-10 Hz), but certain parameters common to APP axonal transport still emerge. First, C-terminally tagged APP has an anterograde directionality bias such that approximately 70% of tagged, motile vesicles move anterogradely. Second, APP moves very fast *in vivo* at velocities faster than reported by *in vitro* studies evaluating kinesin motor

activity (Goldsbury et al., 2011; Kaether et al., 2000; Stamer et al., 2002). Finally, APP has been reported to move in distinct carriers: elongated tubular structures and small punctate structures (Kaether et al., 2000).

Consistent with previously published reports, APP moves with an anterograde bias in hIPSC-derived *wt/wt* neurons (See **Figure 4-1F, Table 4-1**). In addition, the percent of stationary APP vesicles (25.5%) is also similar to previously published data. The only notably different exception is Deng et al., 2013, which reported that 67.7% of APP vesicles were stationary. The high percent of stationary APP vesicles may be because the study was done in mouse *embryonic* cortical neurons as opposed to adult mouse neurons or due to the slower acquisition frame rate of 1Hz.

In comparing the APP transport data to publications that include the reversing category, it is worth noting that hIPSC-derived *wt/wt* neurons seem to have a greater percent of reversing events (44.8% vs 9.2% and 15.8%) (Gunawardena et al., 2013; Reis et al., 2012). There are a number of reasons that may explain the increase in reversing events in hIPSC-derived neurons. The publications that reported fewer reversing events were both done in *Drosophila* segmental nerve by imaging permeabilized embryos. Therefore, it's possible that the increase in reversing events could be an artifact of using an *in vitro*, overexpressing culture system. Alternatively, the increase in reversing events could be species-specific and reflective of human APP transport as opposed to *Drosophila.* Finally, it is generally well accepted in the hIPSC field that the

differentiated neurons analyzed are not fully mature so perhaps the increase in reversal events is due to the young nature of the neurons. Clearly further work needs to be done to determine if the increase in the reversing category is species-specific, maturity-dependent, or due to the *in vitro* transfection system.

As mentioned above, APP FAT is regulated by kinesin-1 motors, but *in vivo* speeds are faster than *in vitro* reported speeds (Amaratunga et al., 1995; Ferreira et al., 1992; Kamal et al., 2000; Koo et al., 1990; Simons et al., 1995; Szodorai et al., 2009; Tienari et al., 1996). Consistent with previous reports (Goldsbury et al., 2011; Gunawardena et al., 2013; Kaether et al., 2000; Reis et al., 2012; Stamer et al., 2002), APP segmental (defined as velocities within a moving vesicle trajectory segment unbroken by a pause) and duration-weighted velocities (the average velocity behavior that vesicles exhibit per time spent moving) in hIPSC-derived neurons were substantially faster than the highest mean velocity of 0.8 μm/sec reported for single or multiple kinesin-1 motors in vitro (Howard, 2002). In fact, mean anterograde duration-weighted segmental velocities were faster than values reported in *Drosophila* segmental nerve axons using similar imaging parameters (Gunawardena et al., 2013; Reis et al., 2012). Interestingly, this is consistent with reported segmental velocities in mouse hippocampal neurons (~2.0 μm/sec (Rodrigues et al., 2012)) and in mouse DRGs (~1.3 μm/sec (Fu and Holzbaur, 2013)), which were also acquired at a fast frame rate (10 Hz and 4 Hz, respectively). This suggests that mammalian APP may move at faster speeds than *Drosophila* or, as with the increase in reversal

events, it's an artifact of an *in vitro* transfection system.

Importantly, anterograde APP moved predominantly in long, uninterrupted tracks with long run lengths and exhibited few pausing events (**Table 4-2**), as expected of a highly processive, kinesin-1-driven cargo. In contrast, retrograde APP moved at slower speeds with shorter run and a slightly higher pause frequency. The slower, less consistent movement behavior of retrograde APP is consistent with dynein-driven transport, which in contrast to kinesin-1 behaves in a poorly processive fashion and requires dynactin to function optimally (Levy and Holzbaur, 2006).

While APP transport has been studied extensively because of its connection to AD, published reports of BACE1 axonal transport behavior are few. Nevertheless, there are indications that BACE1 is transported bidirectionally in axons and that BACE1 undergoes FAT (Buggia-Prévot et al., 2014; Deng et al., 2013; Steuble et al., 2012; Wang et al., 2012; Ye and Cai, 2014). BACE1 anterograde transport is regulated by a kinesin-1-dependent mechanism (Kamal et al., 2000; Steuble et al., 2012) while retrograde BACE1 transport is thought to be regulated by dynein and Snapin, as a dynein motor adaptor for the late endosome (Ye and Cai, 2014). Directionality behavior of BACE1 is more variable than for APP with conflicting reports. Steuble et al. 2012 published that BACE1 moves in axons with an anterograde bias (72% of motile BACE1 vesicles), while two conflicting reports (Wang et al., 2012; Ye and Cai, 2014) report that BACE1 moves with a retrograde bias. Yet another couple of publications (Buggia-Prévot

et al., 2014; Deng et al., 2013) report BACE1 moves equally in an anterograde and retrograde direction. Differences may be due to differences in neuronal subtype, age, or because of transfection-induced changes to BACE1 motility.

4.4.2 Rab5a Axonal Transport is Consistent with Behavior of Kinesin-3-Dependent Cargo

Unlike the highly processive transport behavior of APP and BACE1, Rab5a was predominantly stationary and exhibited few long-range runs with vesicles moving in a saltatory, reversing pattern. The different transport behavior of Rab5a may be reflective of different motor involvement since unlike APP and BACE1, which are known to require kinesin-1 for proper processive movement, Rab5a motility is thought to be mediated by kinesin-3 (Huckaba et al., 2011; Schuster et al., 2011). Unlike kinesin-1 motors, which are very resistant to dissociation by force, kinesin-3 motors exhibit extreme sensitivity to load (Arpağ et al., 2014). Seemingly counterintuitively, kinesin-3 is the fastest kinesin motor, but because of the weak electrostatic interaction between its positively charged K-loop and the negatively charged C-terminus of tubulin it exhibits substantial detachment from microtubules.

Thus, the frequent reversals and pausing events of Rab5a vesicles may be reflecting when Rab5a-positive endosomes interact with obstacles or due to physical limitations of moving large endosomes. In fact, the recent publication linking APP β-CTF accumulation to enlarged Rab5a endosomes suggests that a

tipping point occurs when vesicular expansion reaches sizes about 0.5 μm^2 may have inadvertently hit upon a unique property of kinesin-3-dependent cargo, which readily detach from microtubules because of the biophysical properties of kinesin-3 (Arpağ et al., 2014; Kim et al., 2015). Regardless, our data suggest that Rab5a vesicles are behaving as expected in *wt/wt* human neurons and that plasmid transfection can be used to address questions of early endosome dynamics in a human system.

4.4.3 Lysotracker Axonal Transport is Consistent with the Requirement for Dynein-Mediated Retrograde Movement for Maturation

While published results of lysosomal behavior in axons is limited, there are some common parameters that emerge. Of particular note are recent observations indicating that lysosomes (or acidic vesicles) initiate distally in axons and require retrograde transport for proper acidification and maturation (Maday et al., 2012; Moughamian et al., 2013). The requirement for retrograde transport in neurons to drive late endosome/lysosomal maturation is similar to published results in non-polarized cells. The endosomal-lysosomal system initiates at peripheral regions of the cell with kinesin-bound, anterograde vesicles such as early endosomes clustering in the periphery of a cell and progressively recruiting components of the retrograde machinery (Li et al., 2014; Scott et al., 2014).

In our hands, Lysotracker-positive vesicles exhibited a retrograde bias with smaller lysosomes in the distal segments of axons that progressively became larger and brighter as they approached the soma (not shown). In fact, soma Lysotracker-positive vesicles were dramatically brighter than axonal ones and exposure time had to be increased to visualize axonal Lysotracker vesicles. Given the consistent observations that the endosomal-lysosomal system is affected in fAD (reviewed in Nixon, 2013) and the hypothesis that impairments in retrograde pathways may lead to neuronal dysfunction (Perlson et al., 2010), demonstrating proper acidic vesicle axonal transport in hIPSC-derived is very important.

4.4.4 Mitochondria Axonal Transport is Consistent with Previous Reports and Suggests hIPSC-Derived Neurons are Immature

Mitochondria are known to move bi-directionally over long distances, exhibiting frequent reversal events (Sheng, 2014). They are very dynamic structures that can undergo fission and fusion events and whose behavior is highly dependent on cell heath, respiration, metabolic state, and synaptic activity. Additionally, mitochondrial behavior and motility is influenced by the maturity of the neuron. For example, mature neurons are known to exhibit predominantly stationary mitochondria (70-80%) (Kang et al., 2008) and mitochondria are known to “dock” at active synapses (Sun et al., 2013). The movement behavior of

mitochondria we observed in hIPSC-derived human neurons is, therefore, most similar to the data obtained from immature neurons.

The high motility and low percentage of stationary mitochondria we observe are most closely related to mitochondria behavior away from synaptic sites and fits with the observation that hIPSC-derived neurons do not form many active synapses (Goldstein et al., 2014; Obashi and Okabe, 2013). This confirms the long-held tenant that current differentiation protocols for hIPSC-derived neurons generate predominantly immature, young neurons. To fully evaluate the contribution of mitochondrial dynamics in neurodegenerative disease, future experiments may need to be performed in aged neurons or using next-generation differentiation protocols that generate mature neurons more rapidly (Zhang et al., 2013).

4.4.5 Final Thoughts

The data from this chapter are consistent with previously published reports of APP, BACE1, Rab5a, lysosomal, and mitochondrial motility in culture systems. Though hIPSC-derived neurons are frequently criticized for incompletely recapitulating mouse model systems, our data from this chapter indicate that axonal transport is behaving similarly to previously published reports. APP and BACE1 move bi-directionally in a strongly processive fashion at fast speeds consistent with motily of kinesin-1-dependent cargo. Rab5a is predominantly stationary, exhibiting saltatory behavior consistent with its role as a kinesin-3

cargo. Lysotracker vesicles exhibit a retrograde movement bias and staining pattern consistent with reports that indicate acidic vesicles require retrograde transport for proper maturation. Mitochondria move bi-directionally with the majority of organelles exhibiting either reversing or stationary behavior. Importantly, this is the first description of hIPSC-derived neurons grown and imaged for axonal transport behavior with Invitrogen Trackers in microfluidic devices.

The combined data from this chapter indicate that hIPSC-derived neurons can be used to analyze the axonal transport behavior of a variety of cargo and that axonal cargo behavior is similar to other published systems.

4.5 Acknowledgements

Chapter 4 contains parts of a manuscript currently being prepared for submission. Reyna, S.M.*, Woodruff, G., Weissmiller, A., Dunlap, M., Kloss, N., Goldstein, L.S.B. “Altered Axonal Transport of APP and Lysotracker Vesicles in $PS1^{\Delta E9}$ hIPSC-Derived Neurons.” The dissertation author was the primary investigator and author of this paper.

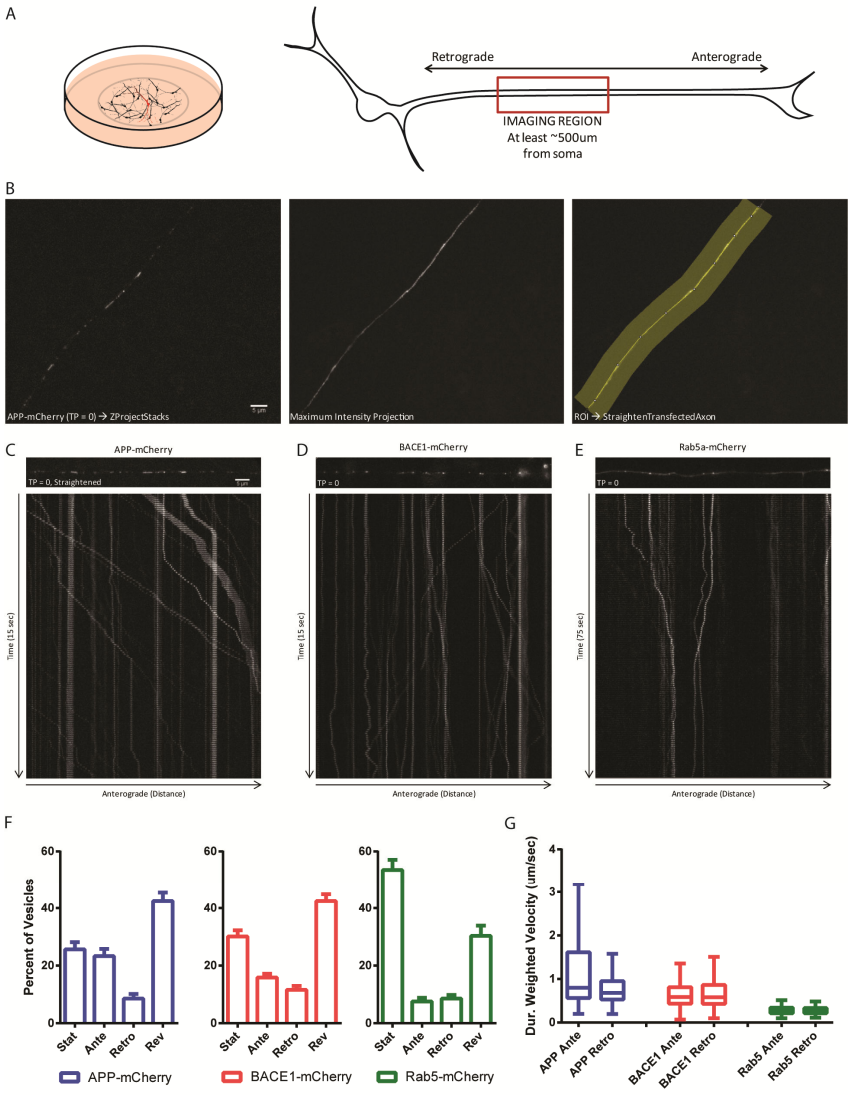

Figure 4-1 Imaging Transfected Cargo in hIPSC-Derived *wt/wt* Neurons
A) First inset: Schematic of differentiated NPCs dissociated, replated, and transfected with fluorescent constructs in 35-mm imaging slides. Second inset: schematic of hIPSC-derived neuronal morphology, directionality of axonal transport, and imaging region. Movies were acquired at least 500 µm from the cell soma in medial axonal regions. B) Movies were processed in ImageJ to generate maximum intensity projections and identify axons with motile vesicles. ROIs were manually generated from the Maximum Intensity Projections and used to straighten axons. Examples of straightened axons and kymographs for APP-mCherry (C), BACE1-mCherry (D), and Rab5a-mCherry (E). F) Quantification of average directionality of vesicles in *wt/wt* neurons for APP-mCherry (blue), BACE1-mCherry (red), and Rab5a-mCherry (Green). Averages represent the average of 6-7 coverslips and 2 NPC lines per condition. G) Box plot distributions of the duration-weighted velocities for APP-mCherry (blue), BACE1-mCherry (red), and Rab5a-mCherry (Green). Box plots represent Tukey's distribution as determined by Prism software.

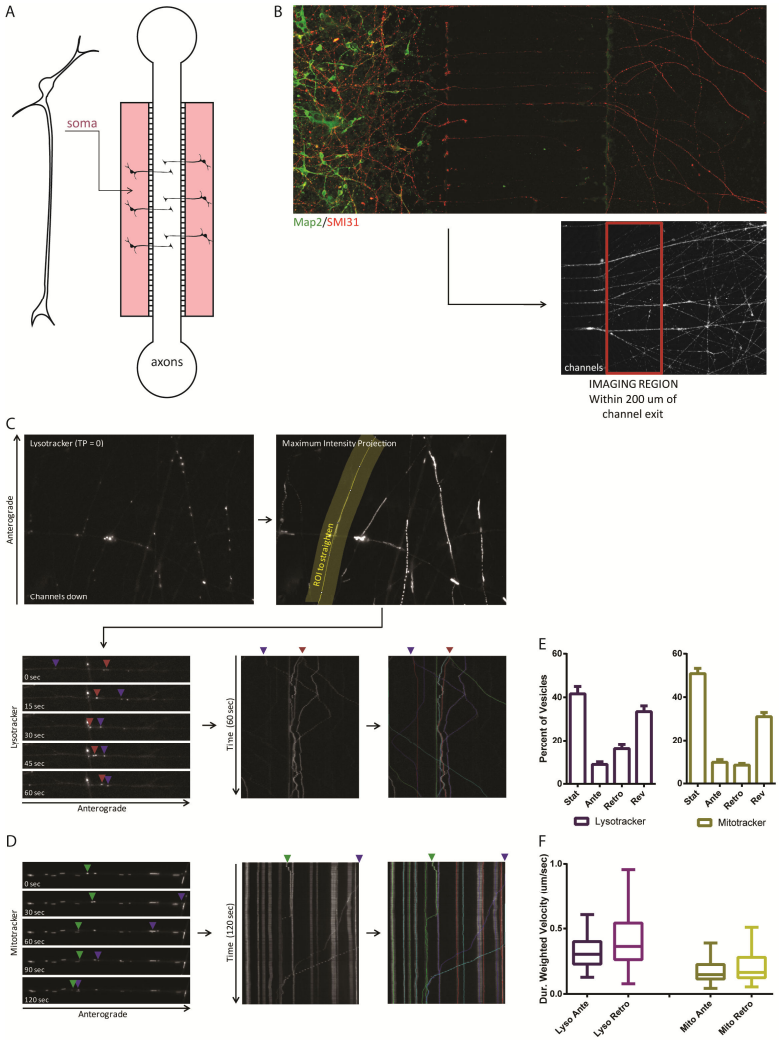

Figure 4-2 Imaging Lysotracker and Mitotracker Dyes in hIPSC-Derived Axons Grown in Microfluidic Devices

A) Schematic of microfluidic devices employed for culturing dNPCs. Dimensions: Soma chamber (3mm x 23mm x 10mm), capillary channels (10µm x 3µm x 450µm) and axonal chamber (3mm x 100µm x 39mm). B) dNPCs were dissociated and replated in soma side of microfluidic devices and allowed to extend axons for 6-8 days. Neurons were properly polarized such that processes that grew through capillary channels were SMI31-positive but Map2-negative. For tracker experiments, axons were imaged within 200um of the channel exit and at least 100um away from the axon terminal. C) Axons were imaged directly in the microfluidic chambers plated on glass coverslips. Axons with motile trackers were identified by generated maximum intensity projections and then manually identifying ROIs. Anterogradely-moving vesicles were defined as movement away from the channel exit. Examples of straightened-axons and kymographs with Lysotracker (C) and Mitotracker (D) staining. Individual tracks are color highlighted. Percent directionality (E) and duration-weighted segmental velocity box plots (F) of Lysotracker (purple) and Mitotracker (yellow) vesicles. Box-plots were generated in Prism using Tukey whiskers.

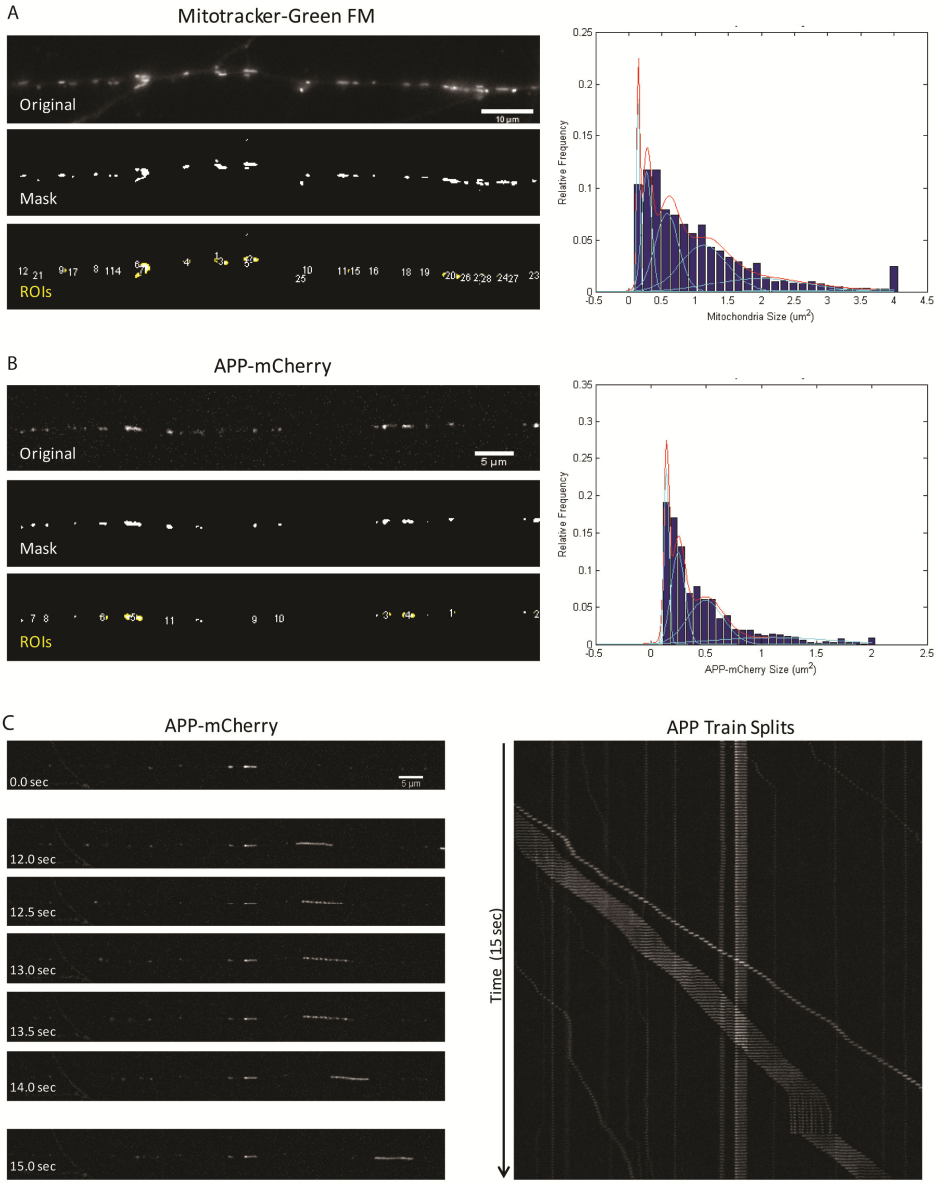

Figure 4-3 Size Segmentation Program to Analyze Mitochondria and APP Size
A) Mitotracker and B) APP-mCherry-expressing axons were thresholded to generate masks and ROIs corresponding to individual structures were automatically generated in ImageJ. Mitochondria and APP clustered in non-parametric distributions with multiple modes. C) A surprising movie where a long APP-mCherry tubule paused at ~12 sec and split into 9 clearly distinct vesicles before continuing to move anterogradely at fast speeds.

Table 4-1 Summary of Cargo Movement Parameters in the Current Study and the Literature

	Publication	Label	Cell Type	Percent Directionality [a, b]				Segmental Velocities		Dur. Weighted Segmental Velocities		Parameters	
				Stationary	Anterograde	Retrograde	Reversing	Anterograde	Retrograde	Anterograde	Retrograde	Time (s)	s / Frame
APP	**Current**	**APP-mCherry**	**Human iPSC-Derived Neurons**	**25.5**	**21.5 (47.1)[c]**	**8.2 (27.4)[c]**	**44.8**	**1.097 ± 0.024**	**0.801 ± 0.014**	**1.385 ± 0.041**	**0.894 ± 0.023**	**15**	**0.1**
	Reis et al., MBoC (2012)	APP-YFP	Drosophila segmental nerve	40.3	32.4	18.1	9.2	0.86 ± 0.55	0.87 ± 0.45	1.09 ± 0.58	1.02 ± 0.41	15	0.1
	Gunawardena et al., Hum Mol Genet. (2013	APP-YFP	Drosophila segmental nerve	31.1	28.8	24.2	15.8	0.83 ± 0.53	0.63 ± 0.36	1.03 ± 0.55	0.76 ± 0.38	22.5	0.15
	Rodrigues et al., Hum Mol Genet. (2012)	APP-YFP	Mouse hippocampal neurons					~2.0	~2.0			15	0.1
	Fu and Holzbaur, JCB (2013)	APP-YFP	Mouse DRGs	~30.0	~40.0	~30.0		~1.3	~1.2			60	0.25
	Kaether et al., MBoC (2000)	APP-YFP	Mouse hippocampal neurons	32.0	48.0	20.0		4.5 ± 1.5	2.9 ± 1.0				
	Chiba et al., Mol Cell Biol (2014)	APP-EGFP	Mixed mouse cortical neurons	24.0	66.0	10.0		2.73 ± 0.69				20	
	Mar et al., J Neuro. (2014)	APP-YFP	Mouse DRGs		~50.0	~50.0		~2.8	~1.8			120	0.8
	Szodorai et al., J Neuro. (2009)	APP-GFP/RFP	Mixed mouse cortical neurons	41.0	30.0	29.0						120	0.2
	Deng et al., J Biol Chem (2013)	APP-EGFP	Mouse embryonic cortical Neurons	67.7	17.1	15.1						60	1
	Steuble et al., Biology Open (2012)	APP-mRFP	Mouse hippocampal neurons		74.0	26.0						60	1
	Vagnoni et al., Hum Mol Genet (2013)	APP-EGFP	Rat cortical neurons					~4.2	~2.0			120	1
BACE1	**Current**	**BACE1-mCherry**	**Human iPSC-Derived Neurons**	**30.2**	**13.9 (35.3)[c]**	**13.2 (34.4)[c]**	**42.6**	**0.662 ± 0.013**	**0.667 ± 0.013**	**0.775 ± 0.022**	**0.789 ± 0.021**	**120**	**1**
	Deng et al., J Biol Chem (2013)	BACE1-mRFP	Mouse Embryonic Cortical Neurons	59.2	22.5	18.3		0.26	~0.16			60	1
	Steuble et al., Biology Open (2012)	BACE1-eGFP	Mouse hippocampal neurons		72	28						60	1
	Buggia-Prevot et al., Mol Neurodegener (20	BACE1-YFP	Mouse hippocampal neurons					0.56 ± 0.03	0.52 ± 0.03			3-5 min	1
	Buggia-Prevot et al., Mol Neurodegener (20	BACE1-YFP	Adult Hippocampal Mossy Fibers					0.33 ± 0.01	0.33 ± 0.02			4 min	0.067
Rab5	**Current**	**Rab5a-mCherry**	**Human iPSC-Derived Neurons**	**52.3**	**8.3 (23.8)[c]**	**8.5 (23.9)[c]**	**30.4**	**0.275 ± 0.006**	**0.282 ± 0.007**	**0.297 ± 0.009**	**0.297 ± 0.009**	**75 sec**	**0.5**
	Power et al., Mol Neuro (2012)	Rab5-YFP	Drosophila larval neurons	~55.0	~10.0	~15	~20.0			0.68	0.62	75 sec	0.5
	Ponomareva et al., J Neuro (2014)	GFP-Rab5c	Zebrafish RB sensory neurons		50	50		~0.4	~0.38			400 s	2
Lysosomes	**Current**	**Lysotracker Red DN**	**Human iPSC-Derived Neurons**	**27.0**	**9.6 (29.6)[c]**	**19.1 (43.5)[c]**	**44.4**	**0.41 ± 0.029**	**0.454 ± 0.025**	**0.48 ± 0.048**	**0.531 ± 0.038**	**60**	**0.5**
	Lee et al., J Neuro (2011)	Lysotracker Red	Mouse cortical neurons	3.2	50.0	46.8		~0.19	0.17 (0.29 ± 0.03)[d]			5 min	3-5 s
	Lee et al., J Neuro (2011)	YFP-LAMP	Mouse cortical neurons	4.9	56.1	39.0		~0.3	0.28 (0.54 ± 0.05)[d]			5 min	3-5 s
	Moughamian and Holzbaur, Neuron (2012)	Lamp1-RFP	Mouse primary DRG neurons	~55.0	~20.0	~25.0						131.8	366 ms
	Mar et al., J Neuro. (2014)	Lysotracker Red	Mouse DRGs	60				~0.75	~0.95			120	0.8
Mitochondria	**Current**	**Mitotracker Green F**	**Human iPSC-Derived Neurons**	**50.6**	**8.9 (23.0)[c]**	**8.6 (26.4)[c]**	**31.9**	**0.191 ± 0.004**	**0.229 ± 0.006**	**0.207 ± 0.007**	**0.257 ± 0.009**	**120**	**1**
	Denton et al., Stem Cells (2014)	Mitotracker Red CMX	Human iPSC-Derived Neurons	0.9				0.48 ± 0.21	0.50 ± 0.19			5 min	5
	Saporta et al., Experimental Neurology (201	MitoDsRed	Human iPSC-Derived Motor Neurons	0.45								5 min	1
	Lu et al., J Neurosci Methods (2012)	MitoDsRed2	Mouse DA neurons in microfluidic devices	80	12.5	7.5		~0.39	~0.35			5 min	5
	Morris and Hollenbeck. J of Cell Biol (1995)	R123	Chicken sympathetic chain ganglia	81	12	7		0.32	0.38				
	Sheng. JCB (2014)	Review		70-80				0.32-0.91 um/s					

a. Percent motility is represented as total of reported values for each study. For example, studies that did not report reversing population show only percent of stationary, anterograde, and retrograde.

b. For publications that did not report averages in text values were estimated from figures. Estimates are denoted by a " ~ " sign.

c. For comparison, percent directionality in the current study are also given excluding the reversing population in parantheses. These represent vesicles that moved predominantly in anterograde or retrograde direction throughout the entire imaging time. Stationary percent remains unchanged.

d. In Lee et al., J Neuro (2011) multiple velocity values were reported depending on the experiment. The first value is estimated from Figure 5, in parantheses values were obtained from Table 1.

Table 4-2 Summary of All Analysis Parameters for Axonal Cargo in *wt/wt* hIPSC-Derived Neurons

	APP-mCherry				BACE1-mCherry				Rab5a-mCherry				Lysotracker				Mitotracker			
	Pixel Scale	Time (s)	s/frame	Hz	Pixel Scale	Time (s)	s/frame	Hz	Pixel Scale	Time (s)	s/frame	Hz	Pixel Scale	Time (s)	s/frame	Hz	Pixel Scale	Time (s)	s/frame	Hz
Imaging Conditions	0.127	15	0.1	10	0.127	15	0.1	10	0.208	75	0.5	2	0.208	60	0.5	2	0.208	120	1	1
	Coverslips		Axons		Coverslips		Axons		Coverslips		Axons		Coverslips		Axons		Coverslips		Axons	
Experiment Details	7		46		6		64		3		36		3		29		8		96	
Vesicles	1695				1786				740				423				1926			
	Stat	Ante	Retro	Rev	Stat	Ante	Retro	Rev	Stat	Ante	Retro	Rev	Stat	Ante	Retro	Rev	Stat	Ante	Retro	Rev
Directionality (with Reversing)	25.49	21.47	8.2	44.84	30.24	13.94	13.21	42.61	52.3	8.78	8.51	30.41	43.26	8.51	15.6	32.62	50.57	8.93	8.62	31.88
Directionality (without Reversing)	25.49	47.14	27.37		30.24	35.33	34.43		52.3	23.78	23.92		43.26	21.51	35.22		50.57	23	26.43	
		MEAN ± SEM		COUNT		MEAN ± SEM		COUNT		MEAN ± SEM		COUNT		MEAN ± SEM		COUNT		MEAN ± SEM		COUNT
Sliding Window Velocity (µm/s)	Ante	1.451 ± 0.006		91737	Ante	0.811 ± 0.004		72502	Ante	0.276 ± 0.002		18348	Ante	0.447 ± 0.007		2942	Ante	0.198 ± 0.001		43363
	Retro	0.922 ± 0.005		59080	Retro	0.82 ± 0.004		68248	Retro	0.286 ± 0.002		19547	Retro	0.492 ± 0.006		4451	Retro	0.274 ± 0.002		49145
Average Instantaneous Velocity (µm/s)	Ante	1.247 ± 0.035		799	Ante	0.716 ± 0.024		631	Ante	0.248 ± 0.01		176	Ante	0.411 ± 0.036		34	Ante	0.188 ± 0.008		443
	Retro	0.876 ± 0.029		464	Retro	0.704 ± 0.023		615	Retro	0.264 ± 0.012		177	Retro	0.437 ± 0.027		50	Retro	0.246 ± 0.009		509
Duration Weighted Velocity (µm/s)	Ante	1.385 ± 0.041		1097	Ante	0.775 ± 0.022		987	Ante	0.297 ± 0.009		282	Ante	0.48 ± 0.048		61	Ante	0.207 ± 0.007		482
	Retro	0.894 ± 0.023		863	Retro	0.789 ± 0.021		966	Retro	0.297 ± 0.009		282	Retro	0.531 ± 0.038		73	Retro	0.257 ± 0.009		531
Segmental Velocity (µm/s)	Ante	1.097 ± 0.024		2131	Ante	0.662 ± 0.013		2148	Ante	0.275 ± 0.006		698	Ante	0.41 ± 0.029		106	Ante	0.191 ± 0.004		897
	Retro	0.801 ± 0.014		1868	Retro	0.667 ± 0.013		2163	Retro	0.282 ± 0.007		698	Retro	0.454 ± 0.025		128	Retro	0.229 ± 0.006		940
Net Velocity (µm/s)	Ante	0.884 ± 0.039		799	Ante	0.387 ± 0.025		631	Ante	0.063 ± 0.008		176	Ante	0.196 ± 0.039		34	Ante	0.083 ± 0.008		443
	Retro	0.432 ± 0.031		464	Retro	0.379 ± 0.023		615	Retro	0.082 ± 0.011		177	Retro	0.253 ± 0.028		50	Retro	0.141 ± 0.009		509
Pause Frequency (count/s)	Ante	0.05 ± 0.002		577	Ante	0.072 ± 0.002		549	Ante	0.029 ± 0.001		151	Ante	0.022 ± 0.002		29	Ante	0.012 ± 0		430
	Retro	0.065 ± 0.003		324	Retro	0.077 ± 0.002		533	Retro	0.025 ± 0.001		156	Retro	0.018 ± 0.001		47	Retro	0.011 ± 0		483
Single Pause Duration (s)	Ante	3.317 ± 0.146		577	Ante	2.17 ± 0.062		549	Ante	6.856 ± 0.304		151	Ante	8.664 ± 0.953		29	Ante	13.119 ± 0.506		430
	Retro	2.219 ± 0.111		324	Retro	2.332 ± 0.072		533	Retro	6.291 ± 0.246		156	Retro	8.087 ± 0.711		47	Retro	14.305 ± 0.65		483
Run Length (µm)	Ante	10.209 ± 0.382		2131	Ante	4.665 ± 0.192		2148	Ante	4.487 ± 0.223		698	Ante	7.698 ± 0.796		106	Ante	6.547 ± 0.304		897
	Retro	5.03 ± 0.205		1868	Retro	4.431 ± 0.172		2163	Retro	4.856 ± 0.237		698	Retro	10.517 ± 0.808		128	Retro	8.996 ± 0.401		940
Total Run Length (µm)	Ante	19.831 ± 0.655		1097	Ante	10.151 ± 0.385		987	Ante	11.106 ± 0.491		282	Ante	13.81 ± 1.373		61	Ante	13.446 ± 0.59		482
	Retro	10.887 ± 0.414		863	Retro	9.921 ± 0.359		966	Retro	12.02 ± 0.594		282	Retro	18.392 ± 1.252		73	Retro	18.954 ± 0.807		531
Full Run Length (µm)	Ante	2.867 ± 0.157		205	Ante	2.669 ± 0.139		323	Ante	4.889 ± 0.495		116	Ante	2.83 ± 0.379		12	Ante	2.915 ± 0.173		120
	Retro	3.102 ± 0.249		187	Retro	3.14 ± 0.235		320	Retro	4.184 ± 0.302		104	Retro	5.163 ± 0.903		18	Retro	4.242 ± 0.299		109
Net Run Length (µm)	Ante	19.898 ± 0.872		799	Ante	8.716 ± 0.57		631	Ante	4.713 ± 0.603		176	Ante	11.702 ± 2.353		34	Ante	9.969 ± 0.936		443
	Retro	9.714 ± 0.707		464	Retro	8.521 ± 0.524		615	Retro	6.083 ± 0.786		177	Retro	15.136 ± 1.667		50	Retro	16.945 ± 1.126		509
Switch Frequency (count/s)		0.085 ± 0.003		1263		0.071 ± 0.002		1246		0.025 ± 0.002		353		0.023 ± 0.002		84		0.016 ± 0.001		952

5. Altered Axonal Transport of APP and Lysotracker Vesicles in PS1ΔE9 hIPSC-Derived Neurons

Abstract

A long-standing hypothesis for Alzheimer's Disease (AD) is that axonal transport defects can contribute to impaired neuronal function and drive neurodegeneration. . The evidence for amyloid precursor protein (APP) being a key player in the development of AD is abundant, and mutations in presenilin 1 (PS1) that alter APP proteolytic processing cause familial AD (fAD). Previous work indicated that suppression of PS activity resulted in increased anterograde and, to a lesser extent, retrograde velocities of APP in *Drosophila* axons. This raised the possibility that fAD mutations that reduce PS activity could have similar effects on APP axonal transport. We report that hIPSC-derived neurons with $PS1^{\Delta E9}$ mutations drive enhanced anterograde transport of APP. The increased anterograde velocities and direction of APP in $PS1^{\Delta E9}$ neurons is rescued by overexpression of a phosphodeficient JIP1 (S421A) construct and suggests that $PS1^{\Delta E9}$ mutant neurons drive increased levels of phosphorylated JIP1 (pJIP1) at least partly due to increased levels of APP CTFs. Downstream consequences of increased pJIP1 include impairments in axonal acidic vesicle density, processive retrograde transport, and maturity all of which are impaired in $PS1^{\Delta E9}$ neurons and APP-CTF overexpressing neurons. Thus, perturbations of APP and acidic vesicle transport as a result of reduced PS activity could be driving early neuropathology in fAD.

5.1 Introduction

The major hypothesis in the field of Alzheimer's Disease (AD) research is the amyloid cascade hypothesis, which posits that oligomeric Aβ fragments accumulate abnormally in patients and drive neurotoxic events ultimately leading to neurodegeneration. Though research has focused largely on testing the amyloid cascade model, the last 20 years have seen an appalling clinical trial success rate of 0.4% (Toyn and Ahlijanian, 2014). An alternative, long-standing hypothesis for AD is that axonal transport defects could directly contribute to impairments of neuronal function and lead to neurodegeneration. The evidence for amyloid precursor protein (APP) being a key player in the development of AD is abundant, and mutations in humans that overexpress APP (Down's Syndrome, APP duplication) or alter APP proteolytic processing (many mutations described in APP, PS1, PS2) cause AD. While most work has focused on the role of one of APP's proteolytic product, Aβ, in neuronal dysfunction, there is mounting evidence pointing to toxic effects of APP itself and the βCTF fragment, the immediate Aβ precursor, on protein sorting and axonal transport (Jin et al., 2002; Lu et al., 2000; Toyn and Ahlijanian, 2014; Weissmiller et al., 2015). For instance, mutations or treatments that increase βCTFs have been shown to drive axonal swellings in FAD APP^{SWE} mice (Tg-swAPP PrP) (Stokin et al., 2005), result in reduced retrograde BDNF signaling (Weissmiller et al., 2015), and lead to organelle jams in axons (Dolma et al., 2014; Gunawardena et al., 2013). Collectively, these findings suggest that excess APP CTFs are acting to poison

the transport machinery, perhaps by modulating kinesin-1 activity at the expense of its proper function. Therefore, it is possible that APP could be poisoning the transport of kinesin-1 dependent cargo such as APP, lysosomes, and/or mitochondria and jeopardize the general health of the neuron.

Perhaps the strongest piece of evidence linking increased APP CTF production to neuronal dysfunction, however, comes from the recent clinical trial failures of gamma secretase inhibitors (GSIs). Many GSIs, which ablate Aβ production but dramatically increase APP CTF levels, failed at Phase III due in part to worsened cognitive outcomes. Previous work from our lab in *Drosophila* indicated that APP axonal transport is regulated by stable assemblies of kinesin-1 and cytoplasmic dynein (Reis et al., 2012), altered in APP mutations (Rodrigues et al., 2012; Stokin et al., 2005), and enhanced by PS1 haploinsufficiency (Dolma et al., 2014; Gunawardena et al., 2013). In this chapter, we sought to evaluate the axonal transport dynamics of APP in hIPSC-derived neurons with $PS1^{\Delta E9}$ mutation. The $PS1^{\Delta E9}$ mutation is a single point mutation that results in in-frame skipping of exon 9 at the endoproteolytic site of PS1. Recent work from our lab indicated that $PS1^{\Delta E9}$ mutations act as loss-of-function mutations for certain γ-secretase-dependent functions, but can also act as gain-of-function mutations for others (Woodruff et al., 2013). Since PS1 haploinsufficiency enchanced anterograde and retrograde velocities in $PS1^{+/-}$ flies, we wanted to test if $PS1^{\Delta E9}$ mutations drive similar effects on APP transport.

We report that $PS1^{wt/\Delta E9}$ and $PS1^{\Delta E9/\Delta E9}$ neurons have enhanced anterograde APP axonal transport, which is influenced by gene dose.

APP undergoes fast axonal transport mediated by kinesin-1 and is influenced by a number of factors. The C-terminal region of APP may form a complex with kinesin-1 perhaps indirectly through JIP1 (Inomata et al., 2003; Matsuda et al., 2003; Scheinfeld et al., 2002; Verhey et al., 2001), Calsyntenin-1 (Steuble et al., 2012), or by direct binding to APP (Kamal et al., 2000). Regulation of velocity can be further influenced by APP processing (Leem et al., 2002; Muresan et al., 2009; Rodrigues et al., 2012), endosomal sorting (Kim et al., 2015), and phosphorylation of many adaptors or APP itself. For instance, phosphorylation of JIP1 (Chiba et al., 2014; Fu and Holzbaur, 2014, 2013), Tau (Noble et al., 2013), GSK3β (Dolma et al., 2014), and APP (Inomata et al., 2003) have all been associated with differential regulation of APP directionality and speeds. The regulation of APP transport by JIP1 was particularly interesting given recent data indicating that fast anterograde speeds of APP are lost with JIP1 knockdown (Chiba et al., 2014) and that JIP1 regulates the directionality of APP axonal transport by coordinating kinesin and dynein motors (Fu and Holzbaur, 2013).

By overexpressing a phosphomimetic of JIP1 S421D in $PS1^{wt/wt}$ neurons, we were able to mimic the enhanced anterograde axonal transport behavior of APP seen in $PS1^{\Delta E9/\Delta E9}$ neurons. Furthermore, overexpression of the phosphodeficient JIP1 S421A rescued $PS1^{\Delta E9/\Delta E9}$ APP transport to $PS1^{wt/wt}$

levels, while having no statistically significant effect in $PS1^{wt/wt}$ neurons (Fu and Holzbaur, 2013). Increased phosphoryation of JIP1 in fAD neurons can have effects beyond regulation of APP velocities and, in fact, processive retrograde transport of autophagosomes in axons requires non-pJIP1 (Fu et al., 2014). To test if axonal acidic vesicles are functioning correctly in $PS1^{\Delta E9/\Delta E9}$ neurons we made used of Lysotracker DND-99 and evaluated axonal transport dynamics. In support of a role of enhanced pJIP1 in $PS1^{\Delta E9}$ neurons, $PS1^{\Delta E9}$ neurons had reduced axonal density of acidic vesicles with a tendency toward reduced retrograde-moving Lysotracker vesicles. Furthermore, intensity analysis of Lysotracker vesicles suggests that acidic vesicles are not maturing properly in $PS1^{\Delta E9}$ axons.

It is well-characterized that the phosphotyrosine-binding (PTB) domain in JIP1 allows it to bind to the YENPTY motif in the C-terminus of APP (Scheinfeld et al., 2002). Given the close relationship between the C-terminus of APP and JIP1, we wondered if the reduction in Lysotracker density seen in $PS1^{\Delta E9}$ neurons could be partly explained by an increase in APP βCTFs. To test if βCTFs drive reduced axonal Lysotracker density, we transfected mouse hippocampal neurons and hIPSC-derived neurons with GFP, APP-YFP, APP^{SWE}-YFP, and C99-GFP (βCTF) and measured Lysotracker density and transport. We report that βCTF-ovexpressing neurons have reduced axonal Lysotracker density.

Overall our data indicate that PS1 may function to control kinesin-1 activity through phosphorylation of JIP1, possibly by as a result of increased levels of APP βCTFs, and leads to alterations in axonal transport of both APP and Lysotracker vesicles with detrimental effects in fAD mutations.

5.2 Methods

5.2.1 Cell Culture

Cell culture of neurons and differentiated NPCs was performed as described in 3.2.1.

5.2.2 Statistical Methods

Statistics were performed using GraphPad Prism. Percent directionality of transfected cargo is represented as the average of the average across multiple experiments, representing 2 NPC lines per genotype (Figures 5-1, 5-3). Percent directionality and density of Tracker cargo (Lysotracker and Mitotracker) is represented as the average across axons since F-test indicated that axons were not statistically different from each other across experiments (Figures 5-4, 5-6, 5-7). For experiments with JIP1 phosphorylation constructs, average across axons is depicted (Figure 5-5). Percent directionality and densities were normally distributed and a two-way ANOVA with a post hoc Tukey test was used to compare genotypes. Duration-weighted segmental velocities were not normally distributed and a nonparametric Kruskal-Wallis test with Dunn’s multiple

comparison was used to compare genotype medians. Box-plots in the figures were plotted using Tukey whiskers in Prism, excluding outliers.

5.2.3 Axonal Transport of Transfected and Tracker Cargo

Methods for axonal transport are extensively described in Chapter 4.

5.2.3 Immunofluorescence

Quantitative immunofluorescence methods are extensively described in Chapter 2.

5.2.4 Antibodies and plasmids

Lamp2 (BD) was used at 1:200 on purified neurons. Rab5a and Rab5b were generously donated by the Mobley lab at UCSD and used at 1:100. APP-mCherry and Rab5a-mCherry constructs were generously donated by Mobley lab. GFP, APP-YFP, APP^{SWE}-YFP, and C99-EGFP constructs are described in Rodrigues et al. 2012. BACE1-mCherry was synthesized and cloned in house by Angels Almenar (found hidden in the -80C freezer downstairs). The phosphomimetic JIP1 S421D and phosphodeficient JIP1 S421A were generously donated by the Holzbaur lab.

5.3 Results

5.3.1 $PS1^{\Delta E9}$ Neurons Have Enhanced Anterograde APP Transport

To test if PS1$^{\Delta E9}$ mutations affect axonal transport of APP, we transfected hIPSC-derived differentiated NPCs with APP-mCherry and analyzed the transport behavior of APP with Laptrack71 in Matlab. As discussed in Chapter 4, APP predominantly undergoes FAT with a strong anterograde bias (see kymograph examples in **Figure 5-1A**). Detailed analysis of many axons and APP tracks indicated that APP directionality was affected in PS1$^{\Delta E9/\Delta E9}$ neurons with more reversing APP vesicles and fewer stationary ones. APP percent directionality was not statistically different in PS1$^{wt/\Delta E9}$ neurons compared to PS1$^{wt/wt}$ (**Figure 5-1B, first inset**). Additional analysis looking at simple population clustering (defined as the average direction a single vesicle took throughout the entire movie) indicated that most of the reversing APP vesicles were moving in a predominantly anterograde direction without affecting the retrograde population (**Figure 5-1B, second inset**). While PS1$^{wt/\Delta E9}$ neurons did not reach significance, there is a clear trend to increased anterograde APP. Strikingly, APP duration-weighted segmental velocities were increased in PS1$^{\Delta E9/\Delta E9}$ neurons for anterograde-moving APP vesicles and, to a lesser extent, retrograde-moving APP vesicles (**Figure 5-2C)**. PS1$^{wt/\Delta E9}$ neurons had increased anterograde duration-weighted segmental velocities, but did not exhibit a change in retrograde speeds.

Overall, the pooled data suggested that APP is moving more anterogradely at the expense of the retrograde population so we postulated that the retrograde/anterograde flux ratio (a measure of fluid moving in a tube) was

reduced. While there was a clear trend to a reduced retrograde/anterograde ratio, APP flux in PS1$^{\Delta E9/\Delta E9}$ did not reach significance, Paradoxically, PS1$^{wt/\Delta E9}$ flux was reduced compared to PS1$^{wt/wt}$ (**Figure 5-2D**). Given our observation that APP vesicles travel in both long tubules and single punctuate vesicles and that long APP tubules are composed of trains of linked APP vesicles (**Figure 4-3C**), we tested if APP sizes were different in PS1$^{\Delta E9}$ mutant neurons (See **4.2.3** for detailed methods). Size analysis of transfected APP indicated that APP sizes are not different in PS1$^{\Delta E9}$ mutant axons.

5.3.2 Individual APP Vesicles Have More CTF:NTF and KLC:APP Ratios in PS1$^{\Delta E9/\Delta E9}$ Neurons

The most consistent difference of APP transport behavior in PS1$^{\Delta E9}$ mutations was the increased speed of anterograde APP movement. Regulation of velocity and direction can theoretically be influenced by differences in APP processing, possibly because different APP fragments exhibit differential affinity to cargo adaptors (Rodrigues et al., 2012; Yoon et al., 2006). To test if differences in transport behavior are due to differences in the relative amounts of APP-FL, APP-NTF, and APP-CTF in axons, we stained axons grown in microfluidic devices with an APP C-terminal antibody (APP Epitomics) and an APP N-terminal antibody (5a3/1g7) that exhibit minimal staining in APP$^{-/-}$ backgrounds (**Figure 3-1**) (Guo et al., 2012). Axonal APP densities of both CTF and NTF-stained puncta are reduced in PS1$^{\Delta E9/\Delta E9}$ mutant axons (**Figure 5-2A**), but percent association of NTF on CTF or CTF on NTF are not different (**Figure**

5-2B). These results indicate that the percent association of NTF and CTF stains are not markedly different in PS1$^{\Delta E9/\Delta E9}$ neurons though there is less APP overall. Interestingly, when we looked at individual APP vesicles and measured the relative intensity of CTF staining to NTF staining, it became apparent that CTF:NTF staining was increased in individual APP vesicles (**Figure 5-2C**). Given that PS1$^{\Delta E9}$ mutations are known to exhibit increased levels of APP CTFs overall (Woodruff et al., 2013), this suggests more APP CTF is being sorted into each APP axonal vesicle in PS1$^{\Delta E9}$ mutations.

It's long been held that kinesin-1 *run lengths* are positively correlated with motor number, but *in vitro* studies indicate that *velocities* do not correlate with motor number (Shubeita et al., 2008). The observation that cargo velocities are independent on motor number is largely based on *in vitro* results and inconsistent with *in vivo* data looking at lipid droplet movement (Shubeita et al., 2008) and APP axonal transport (Reis et al., 2012). Thus, the possibility that APP velocities could be driven by increased motor association on APP vesicles existed. We, therefore, co-stained axons with APP and KLC, and evaluated motor composition on APP vesicles, as previously described (**2.2.4**) (Szpankowski et al., 2012). While PS1$^{wt/\Delta E9}$ axons had fewer KLC puncta axonal density (**Figure 5-2D**) and average percent association of KLC on APP (**Figure 5-2E**), we were skeptical that this was a true genotype-specific effect given that PS1$^{\Delta E9/\Delta E9}$ axons were not statistically different. When we evaluated individual APP puncta, it was apparent that the relative amounts of KLC:APP were increased in PS1$^{\Delta E9/\Delta E9}$ vesicles

(**Figure 5-2F, G**). The data from the two immunofluorescence experiments suggest that APP vesicles may be moving faster because of differences in the relative amounts of APP CTF:NTF and/or kinesin-1 motor:APP. Distinguishing between the two possibilities will require further work, but it's intriguing to see that regulation is occurring at the level of individual vesicles rather than in the pooled population as a whole (given that percent association is not markedly different). The data do suggest that the relative amount of motor number on individual APP vesicles may be driving increased velocities.

5.3.3 Phosphomimetic JIP1 (S421D) Induces Enhanced Anterograde APP Axonal Transport in PS1$^{wt/wt}$ Neurons

APP undergoes fast axonal transport mediated by kinesin-1 and is influenced by a number of factors. The C-terminal region of APP may form a complex with kinesin-1 perhaps indirectly through JIP1 (Inomata et al., 2003; Kamal et al., 2000; Matsuda et al., 2003; Muresan and Muresan, 2005), Calsyntenin-1 (Steuble et al., 2012), or by direct binding to APP (Kamal et al., 2000). For instance, phosphorylation of JIP1 (Chiba et al., 2014; Fu and Holzbaur, 2013), Tau (Mandelkow et al., 2004; Noble et al., 2013), GSK3β (Dolma et al., 2014), and APP (Inomata et al., 2003; Muresan and Muresan, 2005, 2007; Suzuki and Nakaya, 2008) have all been associated with differential regulation of APP directionality and speeds. From previous work in the lab, we know that PS1$^{\Delta E9}$ mutations do not have elevated levels of phosphorylated Tau

(Woodruff et al., 2013) or phosphorylated GSK3β (data not shown) at the time points analyzed. This raised the possibility that APP vesicle velocity was increased because of increased APP phosphorylation and/or increased JIP1 phosphorylation. Given that JIP1 is thought to form a complex with phosphorylated APP (pAPPJIP1-1) (Inomata et al., 2003; Muresan and Muresan, 2005), it is possible that both events are occurring together and driving increased kinesin-1 association on APP. Unfortunately, measuring levels of phosphorylated APP, kinesin-1, and JIP1 was challenging due to limited sample volumes and experiments are still ongoing.

The regulation of APP transport by JIP1 was particularly interesting given recent data indicating that fast anterograde speeds of APP are lost with JIP1 knockdown (Chiba et al., 2014) and that JIP1 regulates the directionality of APP axonal transport by coordinating kinesin and dynein motors (Fu and Holzbaur, 2013). The recent Cell Biol publication by Erika Holzbaur's group indicated that pJIP1 enhances Halo-KHC speed and run lengths *in vitro* and drives increased APP anterograde direction and speeds *in vivo*. This suggests that binding of KHC stalk to JIP1 may function to enhance KHC speed and APP anterograde motility.

We, therefore, wanted to test the hypothesis that increased pJIP1 can enhance APP anterograde transport in $PS1^{wt/wt}$ neurons. We co-transfected $PS1^{wt/wt}$ neurons with APP-mCherry and a phosphomimetic mutant of JIP1 (S421D) or a phosphodeficient mutant of JIP1 (S421A), and measured axonal transport properties of APP. As predicted, S421D increased anterograde

directionality of APP vesicles (**Figure 5-3A**) and led to faster speeds of both anterograde and retrograde APP tracks (**Figure 5-3B**). These patterns of behavior are remarkably similar to the transport behavior seen in $PS1^{\Delta E9}$ neurons and suggests that phosphorylation of JIP1 enhances APP anterograde motility. Interestingly, overexpression of the phosphodeficient JIP1 S421A did not lead to statistically significant differences in APP directionality or speeds in $PS1^{wt/wtw}$ neurons though there were clear trends to decreased anterograde directionality and speed, as well as an increased stationary pool.

5.3.4 Phosphodificient JIP1 (S421A) Rescues APP Axonal Transport of $PS1^{\Delta E9/\Delta E9}$ Neurons to $PS1^{wt/wt}$ Levels

This raised the possibility that the faster APP velocities seen in $PS1^{\Delta E9}$ mutations could be rescued by using the phosphodeficient mutant S421A. Indeed, $PS1^{\Delta E9/\Delta E9}$ neurons co-transfected with APP-mCherry and JIP1 S421A exhibited a decrease in the population of anterograde-moving APP vesicles (**Figure 5-3C**) and APP velocities were reduced to levels that were not statistically different from $PS1^{wt/wt}$ speeds (**Figure 5-3D**). Retrograde velocities were also reduced, though to slower speeds that $PS1^{wt/wt}$ neurons (**Figure 5-3D**). This likely reflects an overcorrection of APP transport behavior due to excess of non-pJIP1 from overexpression. Regardless, it is encouraging that S421A did not have a statistically significant effect on APP transport behavior in $PS1^{wt/wt}$ neurons, but dramatically affected APP transport in $PS1^{\Delta E9/\Delta E9}$ neurons. Further

work to determine if increased levels of pJIP1 are responsible for enhanced APP anterograde transport is ongoing.

5.3.5 PS1$^{\Delta E9/\Delta E9}$ Neurons Have Normal Transport of Mitochondria

Given the striking APP axonal transport data, we wondered if all axonal cargo was altered as a result of the PS1$^{\Delta E9}$ mutation. We decided to analyze mitochondria transport using Mitotracker Green-FM because this did not require overexpression of a tagged plasmid construct. Furthermore, we wanted to analyze the behavior of another axonally transported cargo that requires kinesin-1 for motility (see **4.1** for more details about Kinesin-1b and mitochondria). Quantification of total mitochondria axonal density indicated that PS1$^{wt/\Delta E9}$ and PS1$^{\Delta E9/\Delta E9}$ axons had similar amounts of mitochondria as PS1$^{wt/wt}$ axons (**Figure 5-4A**). Motility was also not significantly different and mitochondria moved with similar directionality and speeds across all genotypes (**Figure 5-4B, C**). Finally, analysis of mitochondrial size indicated that PS1$^{\Delta E9}$ mitochondria were morphologically similar to PS1$^{wt/wt}$ mitochondria (**Figure 5-4D**). Collectively, the data indicate that not all kinesin-1 cargo is affected by PS1$^{\Delta E9}$ mutations.

5.3.6 PS1$^{\Delta E9/\Delta E9}$ Neurons Have Increased Ratio of Axonally Secreted sAPPα/β

As part of our work, we serendipitously came upon the observation that PS1$^{\Delta E9/\Delta E9}$ axons have increased axonally secreted sAPPα/β because of reduced

sAPPβ levels. For these experiments, differentiated NPCs were grown in microfluidic chambers and allowed to extend their axons for 6-8 days. To measure levels of axonally secreted APP fragments, we changed the media in the compartments, kept the axons in fluidic isolation, and then harvested both media and protein for analysis (Niederst et al., 2015). Interestingly, total levels of full-length APP normalized to tubulin trended toward less (consistent with our axonal immunofluorescence results described in **3.3.1**) (**Figure 5-5A**). When we measured sAPPα/β by using an MSD ELISA (described in Israel et al. 2012), it was apparent that $PS1^{\Delta E9/\Delta E9}$ axons had an increased ratio of axonally secreted sAPPα/β because of reduced sAPPβ levels (**Figure 5-5B**). This is in stark contrast to the ratio of secreted sAPPα/β in the somatodendritic compartment (**Figure 5-5B,** first inset).

These results were intriguing because they suggested that an APP vesicle containing sAPPβ was not trafficking correctly to the axon or that a vesicle responsible for processing APP to sAPPβ was not present in the axon or was functioning incorrectly. This is particularly interesting given that BACE1-mediated APP cleavage constitutes the rate-limiting step in Aβ generation (Evin and Weidemann, 2002). In searching for possible endocytic candidates that regulate BACE-mediated processing of APP, we identified BACE1 vesicles themselves, early endosomes (Wang et al., 2012), lysosomes (Ye and Cai, 2014), and, more broadly, acidic vesicles (Hook et al., 2002).

5.3.7 Rab5a and BACE1 Axonal Transport is not Different in PS1$^{\Delta E9/\Delta E9}$ Axons

Rab5a is a small GTPase localized to the plasma membrane, clathrin-coated vesicles, and early endosomes (Bucci et al., 1994). Both APP and BACE1 are internalized and sorted into Rab5a-positive early endosomes though the routes are different (Reviewed in Zhang and Song, 2013). It's thought that the residence time of APP and/or BACE1 in early endosomes is essential for β-cleavage and that increased association can drive accelerated APP processing and Aβ generation (Rajendran et al., 2006). This raised the possibility that enhanced anterograde APP axonal transport and the reduction in axonally-secreted sAPPβ may be due to impairments in Rab5a GTPase or BACE1 function in axons.

To test if early endosomes and BACE1 are being transported correctly in PS1$^{\Delta E9/\Delta E9}$ axons, we transfected cells with Rab5a-mCherry or BACE1-mCherry and evaluated axonal transport behavior as described in **3.3.1**. Following extensive characterization, it became apparent that neither Rab5a nor BACE1 axonal transport were affected by PS1$^{\Delta E9}$ mutations. Rab5a and BACE1 axonal density, percent directionality, and duration-weighted segmental velocities were not different (**Figure 5-6A,B**). To demonstrate that Rab5a-mCherry construct was actually labeling Rab5a, we transfected mouse hippocampal neurons with Rab5a-mCherry, fixed the samples, and co-stained with a Rab5a antibody or a Rab5b antibody. Rab5b stained neurons exhibited minimal signal in Rab5a-

mCherry transfected neurons, while Rab5a staining dramatically increased (**Figure 5-6C**).

5.3.8 $PS1^{\Delta E9}$ Neurons Have Fewer Axonal Acidic Vesicles

Since we didn't see differences in Rab5a or BACE1, we looked to evaluate the transport properties of lysosomes and/or acidic vesicles by using Lysotracker DND-99. One piece of supporting evidence pointing to the involvement of acidic vesicles in BACE1-mediated processing of APP is the report that BACE1's optimal pH value for activity is acidic (pH5-6) (Hook et al., 2002). We were also interested in looking at acidic vesicles given recent results linking increased pJIP1 with improper processive retrograde transport of autophagosomes in the medial axon (Fu and Holzbaur, 2014; Fu et al., 2014) and the frequent reports of impaired lysosomal function in PS1 fAD mutations (reviewed in Nixon and Mcbrayer, 2013). We started by looking at Lamp2 staining in hIPSC-derived purified neurons. Though there was $PS1^{\Delta E9/\Delta E9}$ soma had increased Lamp2-positive structures, there was no difference in the counts (**Figure 5-7A**). The size difference was also much smaller than what's been previously reported in the literature for post-mortem samples of AD (Gowrishankar et al., 2015; Nixon and Yang, 2011), so we questioned whether this was biologically meaningful. Interestingly, when we looked at axonal acidic vesicle density as measured by Lysotracker staining (see **4.2.2** for details), we observed a marked decrease in total density of axonal acidic vesicles in $PS1^{\Delta E9}$ neurons (**Figure 5-7B**). Because we measured acidic vesicle axonal density in

axons that grew through microfluidic devices, we were analyzing Lysotracker density in the medial axon.

This raised the possibility that processive retrograde motility of acidic vesicles was impaired in $PS1^{\Delta E9}$ axons because of increased pJIP1. Indeed, clustering Lysotracker populations by directionality indicated that $PS1^{\Delta E9/\Delta E9}$ neurons had reduced density of retrograde-moving Lysotracker vesicles while anterograde density was more variable (**Figure 5-7B**). Measuring the flux ratio of Retrograde:Anterograde Lysotracker movement never reached significance but strongly trended to less retrograde flux **(Figure 5-7C**). Duration-weighted segmental velocities were similarly not statistically different though $PS1^{\Delta E9/\Delta E9}$ axonal Lysotracker structures had a much wider range of velocities than $PS1^{wt/wt}$ and $PS1^{wt/\Delta E9}$ acidic vesicle (**Figure 5-7D**). Overall, the motility results indicate that there are trends to reduced retrograde directionality of Lysotracker vesicles in young $PS1^{\Delta E9/\Delta E9}$ axons and raised the possibility that maturation of acidic vesicles was not normal in $PS1^{\Delta E9/\Delta E9}$ neurons. Lysotracker DND-99 intensity is a qualitative measure of acidic vesicle maturity, and dimmer vesicles are thought to be immature, improperly acidified vesicles (Nixon Review). In support of improper acidification and maturity of Lysotracker structures, $PS1^{\Delta E9}$ neurons exhibited a dose-dependent reduction in Lysotracker axonal puncta intensity (**Figure 5-7E**). Further work with ratiometric probes such as Dextran Fluorescein-Tetramethylrhodamine or Lysosensor Yellow/Blue (see **2.2.3**) will need to be

done to definitively determine if axonal acidic vesicle maturation is impaired in $PS1^{\Delta E9}$ axons.

As a final note, we measured average axonal density in both $PS1^{\Delta E9/null}$ and $PS1^{wt/null}$ hIPSC-derived neurons and saw that both exhibited reduced numbers of acidic vesicles in axons (**Figure 5-7G**). The magnitude of the change was on the order seen in $PS1^{wt/\Delta E9}$ and not as dramatic as that seen in $PS1^{\Delta E9/\Delta E9}$, raising the possibility that two copies of $PS1^{\Delta E9}$ can poison axonal transport of acidic vesicles more efficiently than haploinsufficiency.

5.3.9 Neurons with Elevated Levels of β-CTFs Have Fewer Axonal Acidic Vesicles in Both Mouse Neurons and Human hIPSC-Derived Neurons

The increased levels of APP CTFs in $PS1^{\Delta E9}$ neurons (Woodruff et al. 2012) and increased relative levels of CTF:NTF in axonal APP vesicles (**Figure 5-2C**), suggested that toxic APP CTFs could be partly responsible for the reduction in acidic vesicle density observed. To test this possibility, we made use of the γ-secretase inhibitor (GSI), Compound E, and treated $PS1^{wt/wt}$ neurons with 1μM GSI for 24 hours to allow accumulation of APP CTFs (see **Figure 3-9D**). We analyzed Lysotracker axonal density and transport in $PS1^{wt/wt}$ + GSI alongside $PS1^{\Delta E9}$ neurons and saw that GSI reduced axonal Lystracker density (**Figure 5-7B)**, reduced retrograde Lysotracker density (**Figure 5-7B**), reduced the retrograde percent of Lysotracker vesicles (**Figure 5-7C**), and further reduced retrograde:anterograde flux ratio (**Figure 5-7C**). The results were

remarkably similar to those seen in $PS1^{\Delta E9}$ neurons and raised the possibility that increased APP CTFs are affecting Lysotracker function. Vesicle maturity was also analyzed by measuring Lysotracker intensity, but in this case the vesicles were much brighter (**Figure 5-7E**). This is likely because GSI dramatically increases lysosomal calcium levels (data not shown) and Lysotracker DND-99 is known to cross-react with calcium. Since the effects of GSI treatment on Lysotracker puncta could be independent of APP and due to another one of γ-secretase's many targets, we also employed a transfection approach.

We overexpressed GFP, APP-YFP, APP^{SWE}-YFP, and C99-EGFP (βCTF) in both mouse hippocampal neurons and hIPSC-derived $PS1^{wt/wt}$ neurons. 18 hours later, we incubated neurons with Lysotracker DND-99 and imaged Lysotracker transport and density in transfected axons (**Figure 5-8**). In mouse hippocampal neurons, overexpression of APP^{SWE}-YFP and C99-EGFP, but not APP-YFP or GFP, dramatically reduced Lysotracker axonal density with minimal effects on overall transport behavior (**Figure 5-8C**). Interestingly, when we repeated this experiment in hIPSC-derived $PS1^{wt/wt}$ neurons, we saw that not only did APP^{SWE}-YFP and C99-EGFP overexpression result in reduced axonal Lysotracker density compared to GFP alone, but so did APP-YFP (**Figure 5-8D**).

5.4 Discussion

Overall our results indicate that $PS1^{\Delta E9}$ mutations are affecting APP axonal transport and acidic vesicles in a manner remarkably similarly to PS

haploinsufficiency (Gunawardena et al., 2013). Namely, increased velocities of APP with a stronger anterograde bias and reduced lysotracker axonal density.

5.4.1 Do fAD PS1$^{\Delta E9}$ Mutations Enhance APP Anterograde Transport Through Increased APP CTFs and/or pJIP1?

The implication that reduced PS1 activity drives enhanced APP velocities in both *Drosophila* (Gunawardena et al., 2013) and an fAD PS1 mutation, PS1$^{\Delta E9}$, suggests that one of the functions of PS is to suppress kinesin activity. While considerable work still needs to be done to distinguish between the many possible regulators of kinesin-1 activity (i.e. phosphorylation of APP, JIP1, GSK3β, kinesin-1, etc.), it's encouraging that the phosphodeficient JIP1 S421A was able to rescue the enhanced anterograde velocities in PS1$^{\Delta E9/\Delta E9}$ neurons, while having no discernible effect in the PS1$^{wt/wt}$ neurons. The results suggest that JIP1 phosphorylation is playing a role along a mechanistic pathway linking PS activity to kinesin-1, possibly through a γ-secretase-indendent pathway. Another possibility is that PS1$^{\Delta E9}$ neurons exist in a "stress-induced" state where phosphorylation of JIP1 is increased and accelerated APP motility is a secondary consequence of increased JNK activation. PS1$^{\Delta E9}$ mutations drive increased cytoplasmic calcium (unpublished results and Bojarski et al., 2008), which have been shown to activate JNK signaling (Kim and Sharma, 2004).

The report that PS haploinsufficiency also drives increased APP velocities (Gunawardena et al., 2013) suggests that in the case of APP speed regulation,

$PS1^{\Delta E9}$ is functioning like a loss-of-function mutation. That being said, it's possible that elevated levels of βCTFs are acting directly or indirectly to accelerate APP transport. It's possible that βCTFs are more efficient at activating pJIP1 and, consequently, kinesin-1. In this case, the accelerated speed of APP in $PS1^{\Delta E9}$ axons is a reflection of increased levels of βCTFs. This is inconsistent with previous work from our lab looking at axonal transport of βCTF-GFP alone, which indicated that βCTFs had reduced anterograde transport both in terms of directionality and speed (Rodrigues et al., 2012). It's possible that βCTFs activate kinesin less efficiently and the increase in APP soma intensity (**Figure 2-2**) is due to "trapped" βCTFs that are unable to "escape" the soma by recruiting anterograde motor. Thus, transport behavior of APP in the axons is a reflection of fewer βCTFs reaching the axon, however, this does not match the immunofluorescence data that indicates there is increased CTF:NTF ratios on individual vesicles without changes in overall percent colocalization of CTF and NTF staining (**Figure 5-2**).

An alternative possibility is that βCTFs *do* activate kinesin-1 more effectively and are accumulating at distal axonal processes, unable to initiate processive retrograde motion. In this case, the observation that βCTF-GFP constructs move more retrogradely may be misleading. It's possible that rather than following bona-fide βCTFs, βCTF-GFP overexpression results in rapid processing of βCTF to Aβ, leaving an intact GFP that is cleared back to the soma via an APP-independent mechanism. Further work to distinguish between these

possibilities will have to be done. One potential experiment to address the question of whether βCTFs are more efficient at activating/recruiting kinesin-1 would be to transfect neurons with a double-label RFP-APP-YFP and pull down a CTF-enriched fraction by using a YFP antibody. RFP-APP-YFP live imaging may also help to determine if CTF-enriched APP moves differently than NTF-enriched APP or FL-APP.

5.4.2 Downstream Effects of Increased APP CTFs and pJIP1: Are Acidic Vesicles Impaired in fAD PS1$^{\Delta E9}$ Mutations?

One of the interesting implications if reduced PS1 activity is driving increased kinesin-1 activity is that relevant kinesin-1 substrates will redistribute. Assuming that pJIP1 is the primary cause, we would predict that cargos that depend on JIP1 scaffolding to bind kinesin-1 will exhibit an anterograde bias in motility, clustering in the periphery of the cell at the expense of their retrograde movement. Unfortunately, the literature linking JIP1 function to specific neuronal cargo is relatively sparse, but recent work of Fu et al., 2014 suggests that autophagosomes are likely to depend on JIP1 for proper transport and maturation. This is particularly interesting given that autophagy, lysosomes, and acidic vesicles, more generally, are thought to be functioning improperly in PS1 mutations of fAD (Coffey et al., 2014; Lee et al., 2010; Neely and Green, 2011; Nixon and Yang, 2011; Tarabal et al., 2001; Wolfe et al., 2013).

Importantly, there is controversy in the field concerning if PS deficiency does, in fact, drive reduced lysosomal acidification with some groups reporting elevated levels of lysosomal pH (Lee et al., 2010) while others claim that acidification is normal and calcium defects are not (Coen et al., 2012). Perhaps part of the controversy stems from differences in the cellular polarization of the model systems used. In non-polarized cells like blastocysts, fibroblasts, or immortalized cell lines, all of the acidic vesicles can be easily visualized in a single plane, including immature ones that presumably cluster at the cell periphery. In neurons, however, the least mature acidic vesicles would not be present in the soma, but would instead be found at the distal axon tip (Maday et al., 2012). In analyzing acidic vesicle maturity, experimenters will need to take into account the unique polarized structure of the neuron and carefully evaluate soma, dendrites, and axons before making conclusions.

A further implication of reduced axonal density and initiation of retrograde motility of lysosomes is that protein clearance from axons will be impaired in fAD models. Spreading of Aβ from neuron to neuron is thought to be a primary driver of AD pathology. If lysosomal clearance in axons is less efficient in $PS1^{\Delta E9}$ neurons, neurons will not be able to respond to stress-induced injury, clear dysfunctional synapses, or degrade toxic peptides (Domert et al., 2014).

5.4.3 Final Thoughts

Collectively, our data suggest that PS1$^{\Delta E9}$ mutations affect kinesin-1 activity and drive more anterograde transport of select cargo at the expense of retrograde clearance. Further work to determine if altered axonal transport of APP and acidic vesicles is due to increased levels of APP CTFs, increased phosphorylation of motor adaptors or APP itself, or directly due to a γ-secretase substrate will need to be done. It will also be important to determine if these defects are common to other fAD mutations and sAD genomes.

5.5 Acknowledgements

Chapter 5 contains parts of a manuscript currently being prepared for submission. Reyna, S.M.*, Woodruff, G., Weissmiller, A., Dunlap, M., Kloss, N., Goldstein, L.S.B. “Altered Axonal Transport of APP and Lysotracker Vesicles in PS1$^{\Delta E9}$ hIPSC-Derived Neurons.” The dissertation author was the primary investigator and author of this paper.

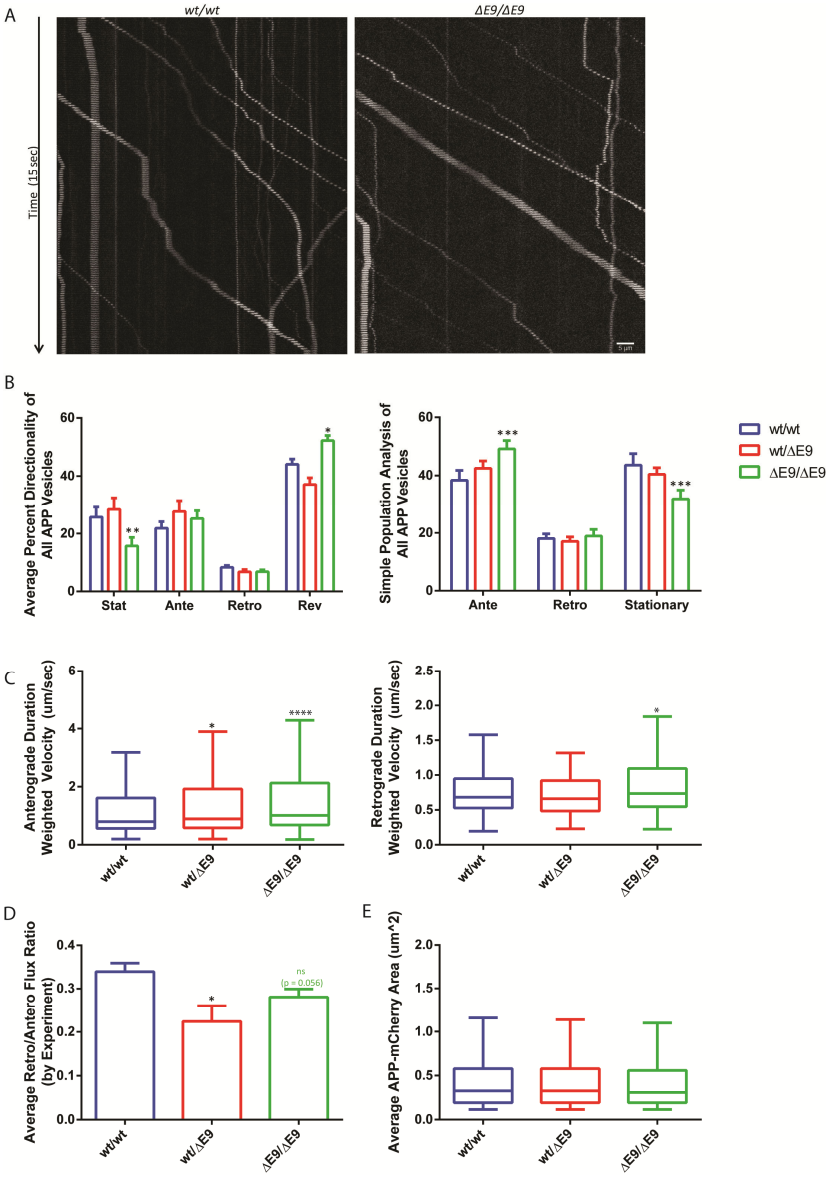

Figure 5-1 Enhanced Anterograde Axonal Transport of APP in PS1$^{\Delta E9}$ Neurons
A) Examples of APP-mCherry kymographs used for quantification of APP axonal transport in PS1$^{wt/wt}$ and PS1$^{\Delta E9/\Delta E9}$ neurons. B) PS1$^{\Delta E9/\Delta E9}$ neurons have reduced population of stationary APP vesicles and an increase in the reversing. With simple population analysis, it becomes apparent that this is because of an increase in anterograde-moving APP vesicles at the expense of stationary ones. C) Strikingly, anterograde APP vesicles move faster in PS1$^{\Delta E9}$ neurons in a dose-dependent manner. PS1$^{\Delta E9/\Delta E9}$ retrograde APP duration-weighted velocities are also significantly increased. D) Analysis of the retrograde/anterograde flux ratio trends to reduced in PS1$^{\Delta E9/\Delta E9}$ neurons and is significantly reduced in PS1$^{wt/\Delta E9}$ neurons. E) APP sizes are not different in PS1$^{\Delta E9}$ neurons. Data represent PS1$^{wt/wt}$ 46 axons, 7 coverslips, PS1$^{wt/\Delta E9}$ 16 axons, 3 coverslips, and PS1$^{\Delta E9/\Delta E9}$ 37 axons, 6 coverslips and over 400-1700 tracks for all genotypes.

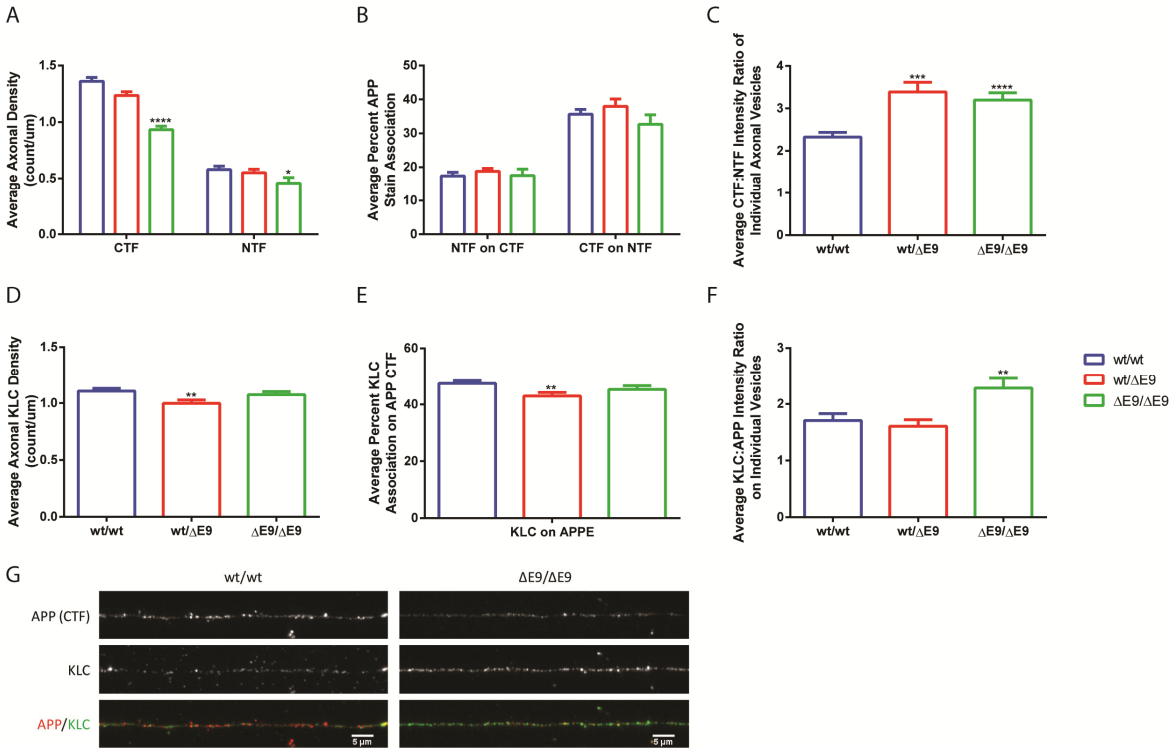

Figure 5-2 Individual APP Vesicles in PS1$^{\Delta E9}$ Neurons Have Increased CTF:NTF and KLC:APP Ratios

A) Average axonal density of APP Epitomics (CTF) and 5a3/1g7 (NTF) puncta staining in hIPSC-derived neuronal axons. PS1$^{\Delta E9/\Delta E9}$ axons had reduced average axonal densities of both CTF and NTF. B) Percent colocalization of NTF/CTF and CTF/NTF were not different in PS1$^{\Delta E9}$ axons compared to PS1$^{wt/wt}$. C) The CTF:NTF intensity ratio on individual APP vesicles was increased in both PS1$^{wt/\Delta E9}$ and PS1$^{\Delta E9/\Delta E9}$ axonal APP vesicles. D) Analysis of average axonal density of KLC puncta in hIPSC-derived neurons indicated that PS1$^{wt/\Delta E9}$ had reduced KLC axonal density, but not PS1$^{\Delta E9/\Delta E9}$ axons. E) Percent colocalization of KLC on APP CTF vesicles was only reduced in PS1$^{wt/\Delta E9}$ axons and not PS1$^{\Delta E9/\Delta E9}$ axons. F) The KLC:APP intensity ratio on individual APP vesicles was increased in PS1$^{\Delta E9/\Delta E9}$ axonal APP vesicles. G) Example staining of axonal APP (CTF) and KLC puncta in PS1$^{wt/wt}$ and PS1$^{\Delta E9/\Delta E9}$ neurons.

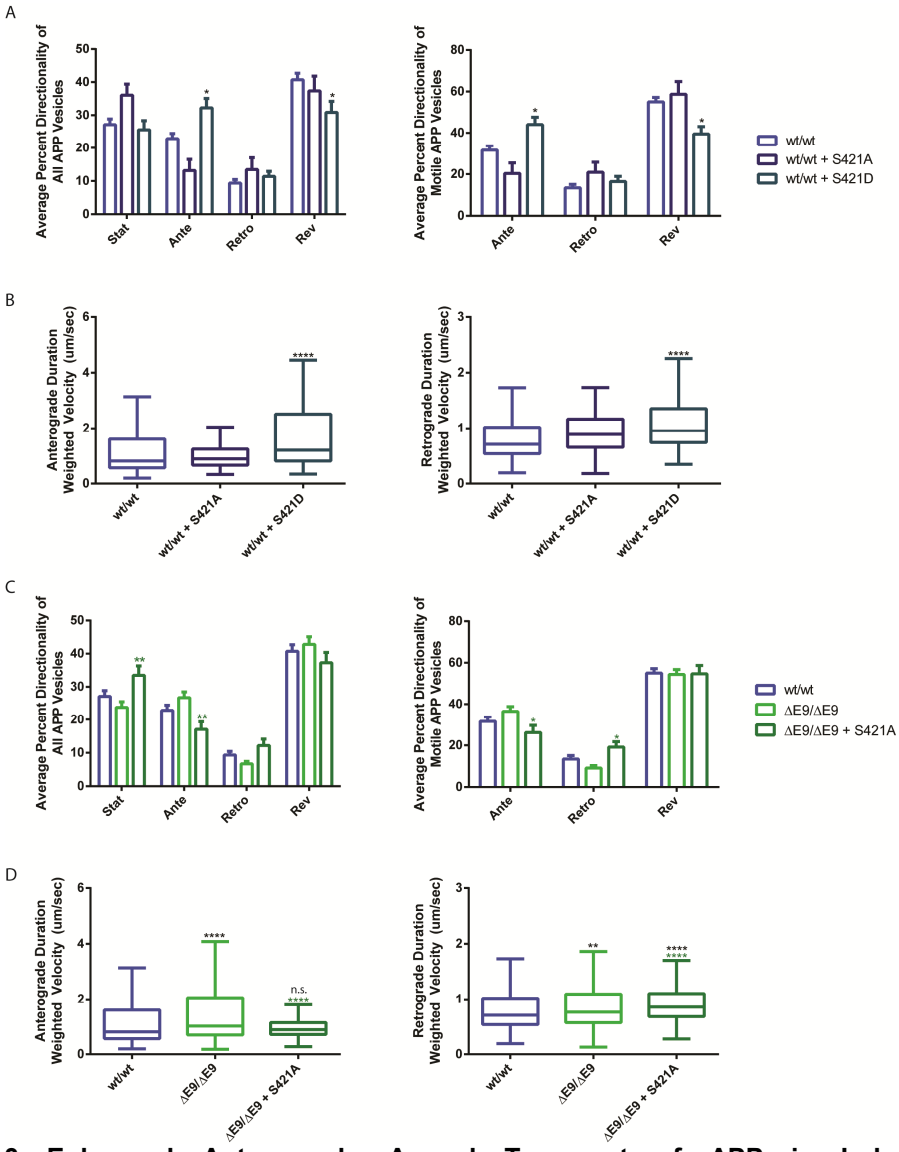

Figure 5-3 Enhanced Anterograde Axonal Transport of APP is Induced with Phosphomimetic JIP1 S421D in PS1$^{wt/wt}$ Axons and Rescued with Phosphodeficient JIP1 S421A to PS1$^{wt/wt}$ Levels In PS1$^{\Delta E9/\Delta E9}$ Axons

A) PS1$^{wt/wt}$ neurons were co-transfected with APP-mCherry and JIP1 S421A or JIP1 S421D and analyzed for transport behavior. PS1$^{wt/wt}$ neurons co-transfected with JIP1 S421D had enhanced anterograde transport of APP and reduced reversing cargo, similar to PS1$^{\Delta E9/\Delta E9}$ neurons. B) Duration-weighted velocities were increased in the anterograde and retrograde directions in PS1$^{wt/wt}$ neurons co-transfected with JIP1 S421D. C) PS1$^{\Delta E9/\Delta E9}$ axons co-transfected with JIP1 S421A had increased stationary and reduced anterograde-moving APP vesicles. Motile vesicles moved retrogradely more frequently too. D) Anterograde duration-weighted velocities were rescued to PS1$^{wt/wt}$ levels when PS1$^{\Delta E9/\Delta E9}$ neurons were co-transfected with JIP1 S421A (black significance). This behavior represented a stastically significant change comparing PS1$^{\Delta E9/\Delta E9}$ neurons with and without JIP1 S421A. Retrograde duration-weighted velocities were "over-rescued" and collapsed to slower speeds.

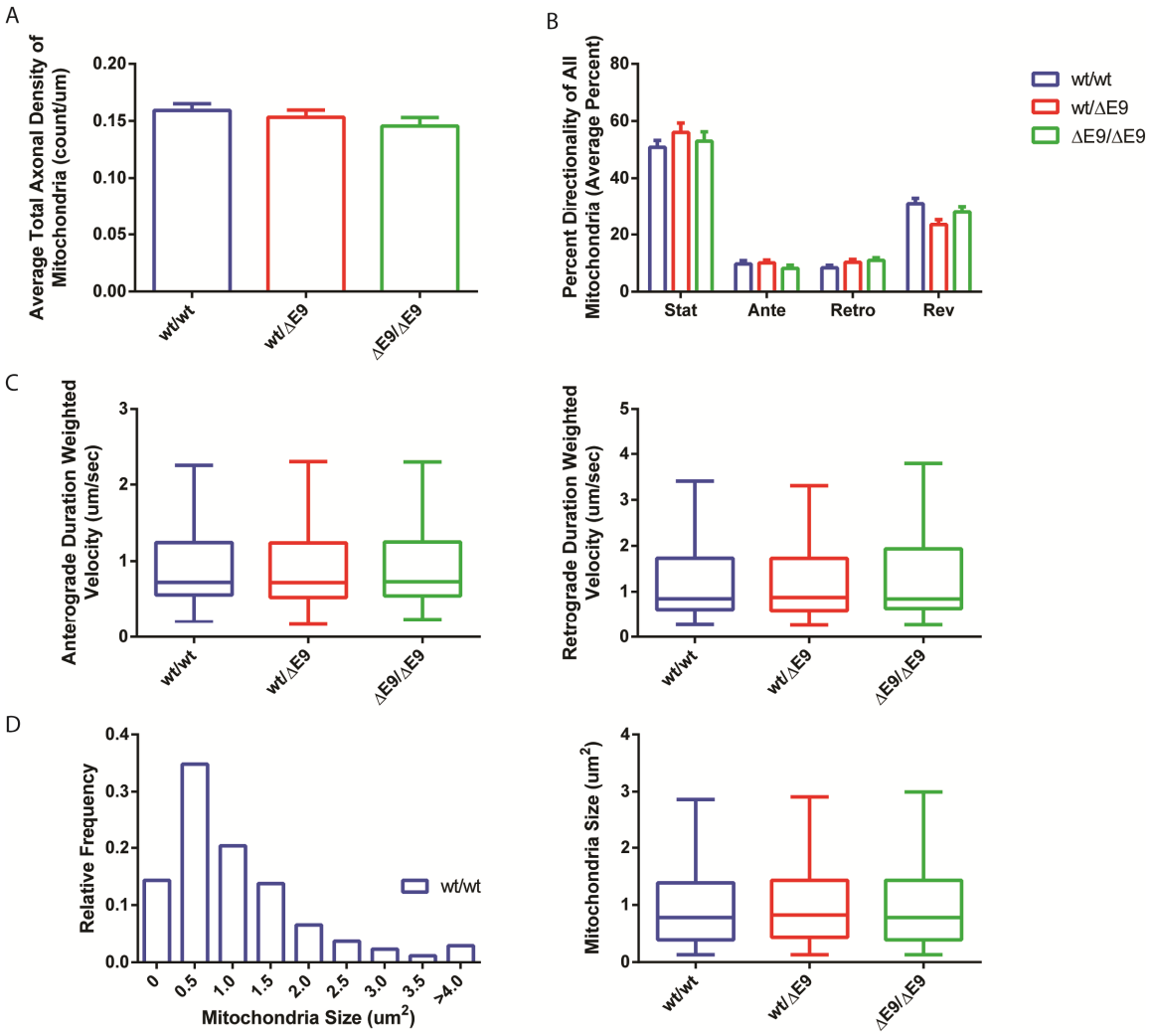

Figure 5-4 Axonal Transport of Mitochondria is not Different in PS1$^{\Delta E9}$ Neurons
A) Average axonal density of mitochondria (identified as Mitotracker-positive structures) was not different in PS1$^{\Delta E9}$ neurons. B) Directionality was also not different in PS1$^{\Delta E9}$ neurons. C) Duration-weighted anterograde and retrograde velocities of mitochondria are also not different in PS1$^{\Delta E9}$ neurons. D) Mitochondria size are not different in PS1$^{\Delta E9}$ neurons. Data represent PS1$^{wt/wt}$ 96 axons, 8 coverslips, PS1$^{wt/\Delta E9}$ 73 axons, 5 coverslips, and PS1$^{\Delta E9/\Delta E9}$ 69 axons, 5 coverslips and over 250-500 tracks for all genotypes.

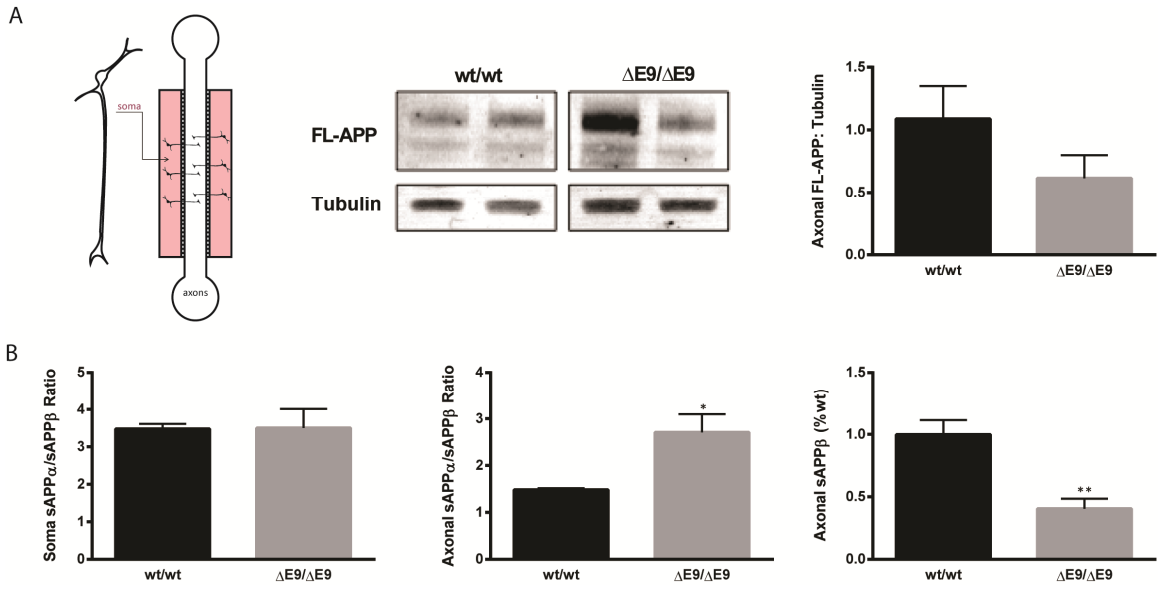

Figure 5-5 PS1$^{\Delta E9}$ Have Reduced Axonal FL APP Levels and Increased sAPPα/β AxonalSecretion Because of Reduced sAPPβ

A) Differentiated NPCs were grown in microfluidic devices and harvested for protein to run on a Western. FL-APP was detectable in PS1$^{wt/wt}$ and PS1$^{\Delta E9/\ \Delta E9}$ axons, but not PS1$^{wt/\ \Delta E9}$ axons. Western is a spliced together membrane from the same experiment. Fl-APP:Tubulin was quantified using Odyssey and PS1$^{\Delta E9/\Delta E9}$ trended to reduced axonal Fl-APP. B) In contrast to soma secreted sAPPα/β levels, which are not different, PS1$^{\Delta E9/\ \Delta E9}$ axons have increased axonal secreted sAPPα/β levels because of reduced sAPPβ.

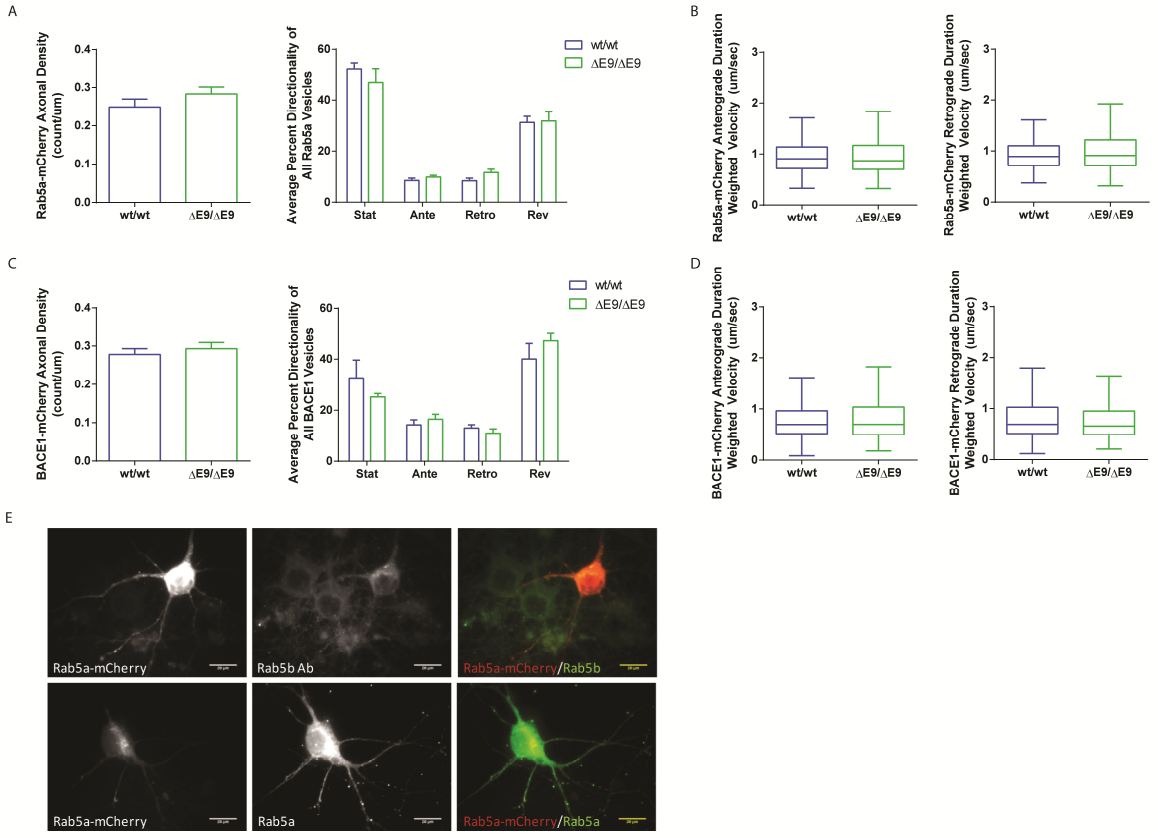

Figure 5-6 BACE1 and Rab5a Axonal Transport is Not Different in PS1$^{\Delta E9/\Delta E9}$ Neurons
A) Rab5a axonal density and percent directionality of vesicles is not different in PS1$^{\Delta E9/\Delta E9}$ neurons. B) Duration-weighted anterograde and retrograde velocities are also not different in PS1$^{\Delta E9/\Delta E9}$ neurons. C) BACE1 axonal density and percent directionality of vesicles is not different in PS1$^{\Delta E9/\Delta E9}$ neurons. D) Duration-weighted anterograde and retrograde velocities of BACE1 vesicles are also not different in PS1$^{\Delta E9/\Delta E9}$ neurons. E) Antibody validation of Rab5a-mCherry construct. Rab5a-mCherry transfected mouse neurons were fixed and co-stained with and antibody against Rab5b or Rab5a. Rab5b exhibited minimal staining in Rab5a-mCherry transfected neurons but Rab5a staining dramatically increased.

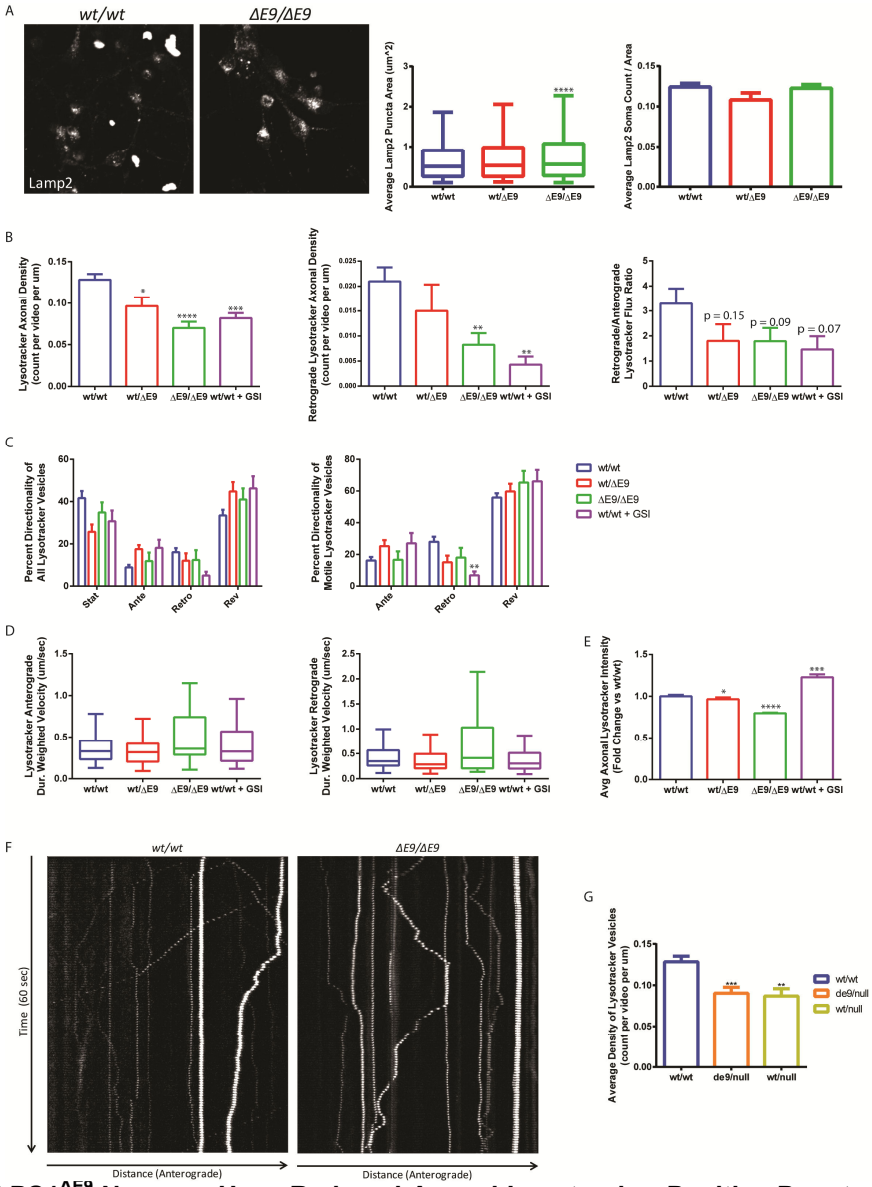

Figure 5-7 PS1$^{\Delta E9}$ Neurons Have Reduced Axonal Lysotracker-Positive Puncta and a Trend to Reduced Retrograde-Destined Lysotracker Puncta

A) Soma Lamp2 staining demonstrated a small but significant increase in Lamp2-positive structures in PS1$^{\Delta E9/\Delta E9}$ neurons though not counts. B) Lysotracker axonal density was markedly reduced in PS1$^{wt/\Delta E9}$ and PS1$^{\Delta E9/\Delta E9}$ axons. This was reflected in reduced retrograde lysotracker vesicles in PS1$^{\Delta E9/\Delta E9}$ axons and PS1$^{wt/wt}$ axons treated with a γ-secretase inhibitor. Anterograde densities were variable. C) Percent directionality and retrograde/anterograde flux ratio suggest that PS1$^{\Delta E9}$ lysosomes are trending to reduced retrograde movement. D) Duration-weighted segmental velocities were not different in PS1$^{\Delta E9}$ axons. E) Average intensity of axonal Lysotracker puncta indicate that PS1$^{\Delta E9}$ axonal acidic structures are dimmer and suggest they are less acidified and not as mature. F) Example kymographs of Lysotracker movement in PS1$^{wt/wt}$ and PS1$^{\Delta E9/\Delta E9}$ axons.

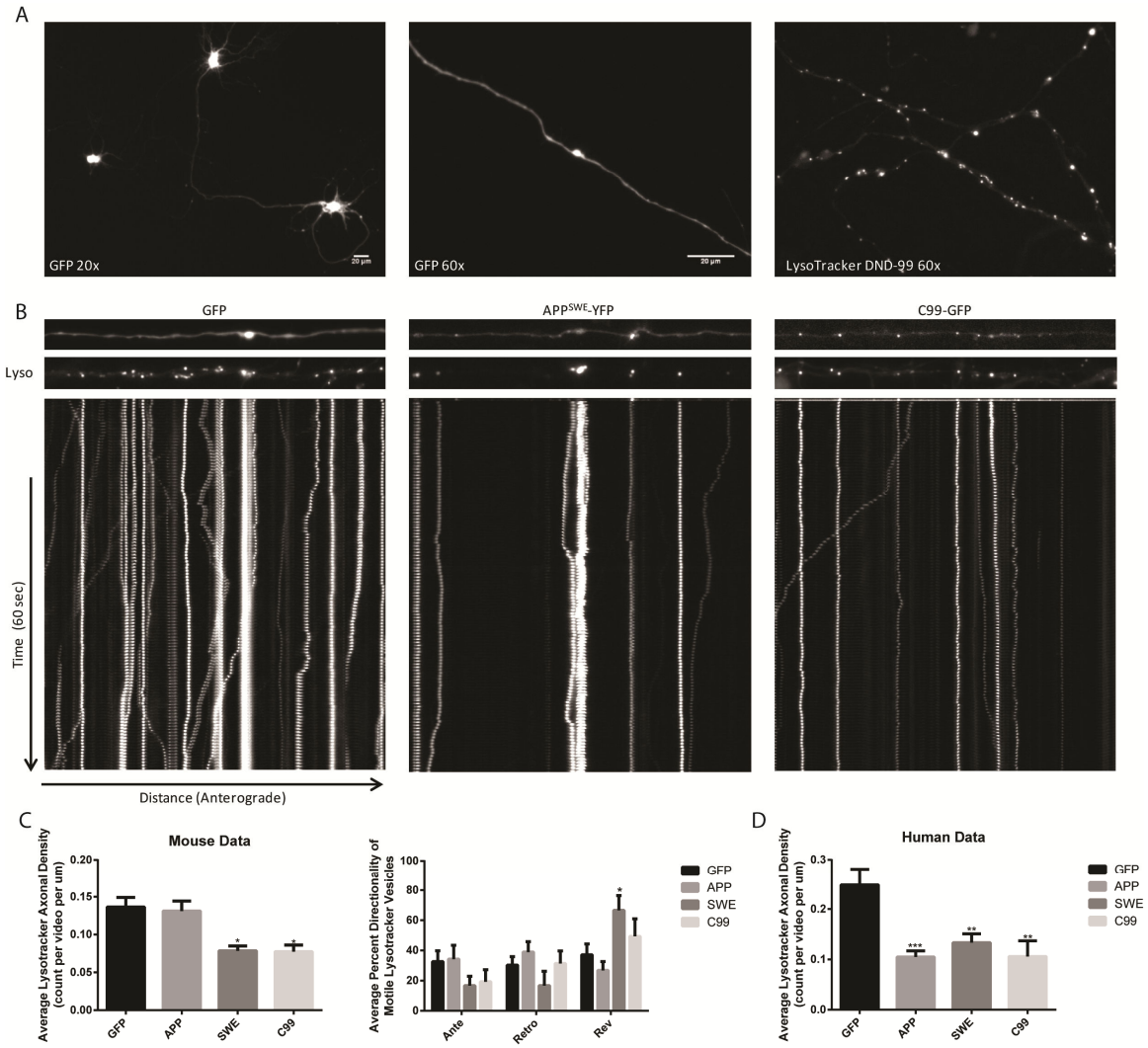

Figure 5-8 β-CTF Overexpressing Constructs Have Reduced Axonal Lysotracker Density in Both Mouse Neurons and Human hIPSC-Derived Neurons

A) Example images showing GFP-transfected hippocampal neurons and an axon selected for analysis. Lysotracker DND-99 staining is also depicted. B) Example kymographs of Lysotracker DND-99 movement in GFP, APP^{SWE}-YFP, and C99-EGFP transfected hippocampal neurons. C) Axonal Lysotracker density and directionality data in transfected mouse hippocampal neurons. Only APP^{SWE}-YFP and C99-EGFP overexpressing mouse axons had reduced Lysotracker axonal density and not GFP or APP-YFP transfected axons. D) The mouse data was repeated in hIPSC-derived neurons. Axonal Lysotracker density was reduced in APP-YFP, APP^{SWE}-YFP, and C99-EGFP transfected neurons compared to GFP-transfected alone.

6. Final Discussion

Abstract

The evidence that AD is a disease of impaired protein sorting is plentiful. Unbiased screens have consistently identified regulators of endocytic trafficking as major risk factors for AD and endosome abnormalities are the earliest known disease-specific alterations in AD (Cataldo et al., 2000; Ginsberg et al., 2010; Treusch et al., 2011). Enlarged early endosomes have been reported in models of Down syndrome (DS) and APP duplications where an extra copy of APP drives a cascade of β-CTF-dependent endocytic dysfunction (Cataldo et al., 2000, 2008; Israel et al., 2012; Kim et al., 2015; Laifenfeld et al., 2007). Further support for a role of altered endocytosis in AD is repeated data indicating that endosomes are highly active sites of APP processing and production of Aβ requires sequential cleavage of APP by β-secretase (BACE1) and γ-secretase along the endolysosomal route (Dingwall, 2001; Hook et al., 2002). Thus, determining how sorting pathways drive altered localization and sorting of APP, its secretases, and other related proteins is critically important for understanding AD pathogenesis.

6.1 Implications from Impaired Transyctosis

Neurons develop a highly polarized structure and require complex sorting pathways to move proteins synthesized in the cell body along long distances toward the axon terminal. One possible route that proteins take to enter the axon is called transcytosis, which refers to receptor-mediated ligand internalization at one side of the cell followed by release at the other end, with and without subsequent protein recycling (Kelly, 1993; Mostov and Simister, 1985). Numerous proteins are known to undergo transcytosis in neurons whether in anterograde (away from the soma toward the synapse) or retrograde direction (from the synapse to the soma) including including APP (Niederst et al., 2015), BACE1 (Buggia-Prévot et al., 2014), TrkA (Ascaño et al., 2009), L1/NgCAM (Wisco et al., 2003; Yap et al., 2008) and LDL/cholesterol (Karten et al., 2003).

In this thesis work, we demonstrate that fAD mutations have defective transcytosis of certain Rab11-dependent proteins such as APP and LDL. Interestingly, reduction of Rab11 axonal density is common to multiple fAD mutations, namely $PS1^{\Delta E9}$ and APP^{v717f} mutations.

The basal reduction suggests that it's not just induction of transcytosis with an antibody (22C11) or with externally administered cholesterol (LDL-BODIPY) but baseline impairments in many Rab11-dependent (and possibly kinesin-1- or JIP1-dependent) pathways. In further support of a constitutively impaired transcytotic pathway, TrkB axonal density and sAPPβ secretion were also reduced in $PS1^{\Delta E9}$ neurons. Previously publications have shown that TrkA:B

and BACE1 can enter the axon via a transcytotic soma-to-axon route. That defects in this process may be important for the development of AD comes from evidence that knockdown of EHD-mediated BACE1 transcytosis significantly reduced Aβ production (Buggia-Prévot et al., 2013), that reducing lysosomal-mediated BACE1 degradation significantly elevates Aβ production (Ye and Cai, 2014), and that TrkA-positive basal forebrain cholinergic neurons (BFCNs) are lost early in AD (Cattaneo and Calissano, 2012). This thesis work is the first report of impaired transcytosis in neurons expressing endogenous levels of mutated fAD proteins and suggests that, despite the small differences, these may be critically important for disease pathogenesis.

6.2 Axonal Transport in fAD: Does APP Compete Anterograde Motor?

There is strong evidence that axonal transport defects are important in AD including observations of defects in neurotrophic signaling independent of Aβ (Salehi et al., 2006), axonal traffic jams (Stokin et al., 2005), microtubule destabilization as a result of abnormally phosphorylated Tau (Baas and Qiang, 2005; Mandelkow et al., 2004; Noble et al., 2013), and reduced motor levels in frontal cortex of AD patients (Morel et al., 2012). Furthermore, impaired axonal transport of mitochondria (Reddy, 2011), autophagosomes (Lee et al., 2010; Neely and Green, 2011; Sanchez-Varo et al., 2012), lysosomes (Ye and Cai, 2014), early endosomes (Kim et al., 2015), BDNF (Weissmiller et al., 2015), and APP (Brunholz et al., 2012; Gandy et al., 2007; Gunawardena et al., 2013; Reis

et al., 2012; Stokin et al., 2005, 2008; Szodorai et al., 2009; Vagnoni et al., 2012) are implicated in AD. The alterations in axonal transport are puzzling and finding a common pathway that can account for these different changes has been challenging. Nevertheless, the data from the $PS1^{\Delta E9}$ neurons does point to a role for kinesin-1, possibly through JIP1, in driving axonal transport differences.

That $PS1^{\Delta E9}$ neurons exhibit enhanced APP anterograde axonal transport suggests that PS1 normally functions to suppress kinesin activity. Combined with the observation that phosphodeficient JIP1 was able to reduce APP velocities to $PS1^{wt/wt}$ levels, the implication is that axonally-destined APP is more efficient at activating anterograde motor. The possibility thus exists that APP in fAD mutations sequesters kinesin-1 from other cargo and could explain the reduction in Rab11, TrkB, APP, and lysosomal densities seen in fAD mutant axons. The fact that Rab5a, BACE1, and mitochondria are normal suggests that it's not all kinesin-1 cargo, but may be axonal cargo that use JIP1 to link kinesin motor to the membrane. Future experiments with JIP1 knockout can help to address whether or not these AD-relevant cargo utilize JIP1 for motility. Ultimately, the results point to a role for APP, possibly the βCTFs, in competing limited motor amounts from other cargo and impairing their axonal entry.

6.3 Defective Cholesterol Sorting: Common Pathways for fAD and sAD?

Genetic analyses have provided important clues to biological pathways that might be defective in fAD and sAD (Antonell et al., 2013). However, the most

common and highly penetrant APOE4 genetic risk factor for sAD, does not obviously perturb the same pathways as those that are altered in fAD APP and presenilin 1 (PS1) mutations. There is some evidence that APOE allelic state might influence turnover of potentially neurotoxic Aβ, but other possibilities have not been ruled out (Arold et al., 2012; Mahley et al., 2006). An intriguing alternative hypothesis, suggested by some epidemiologic evidence and some experiments in mouse overexpression models, is that trafficking of cholesterol-containing lipoproteins could be altered in fAD mutations and sAD APOE4 carriers.

Partial support for this conjecture comes from the normal function of APOE, which is to serve as a lipoprotein constituent mediating brain cholesterol traffic from sites of synthesis in astrocytes to sites of utilization in neurons. Support for this idea is also provided by evidence that the APOE4 variant is trafficked and transported aberrantly in neurons and other cells (Brodbeck et al., 2011). In this regard, while most work on fAD has focused on amyloid-induced phenotypes, there is abundant evidence for non-amyloid induced trafficking and transport defects in fAD mutants (Kim et al., 2015; Pimplikar et al., 2010; Shioi et al., 2007; Stokin et al., 2008). In addition, there is evidence that mutations in PS1 can increase cholesterol levels, diminish uptake of lipoproteins, and influence transcription of cholesterol biosynthetic genes (Walter and van Echten-Deckert, 2013).

We found that fAD mutant neurons alter subcellular distribution and trafficking of APP and internalized lipoprotein, leading to elevated levels of APP in the soma and reduced levels in the axons. One possible mechanism is that β-CTFs bind to LRP1 (Kounnas et al., 1995; Pietrzik et al., 2002), and retain LRP1 in a Rab11 containing compartment until the β-CTF is cleaved by γ-secretase. This idea would explain why γ-secretase inhibition impairs LDL uptake and why that defect can be rescued by β-Secretase inhibition. Another intriguing possibility is that APP, through its C-terminal domain, acts as a cholesterol sensing protein (Beel et al., 2010; Song et al., 2013). There is ample evidence linking elevated cholesterol levels with increased association of APP and β-CTFs to lipid rafts thus favoring amyloidogenic processing of APP (Beel et al., 2010; Bodovitz and Klein, 1996; Guardia-Laguarta et al., 2010; Grimm et al., 2008; Kojro et al., 2001; Simons et al., 1998; Wahrle et al., 2002). The finding that APP β-CTF favors binding to cholesterol over homodimerization suggests that elevated levels of β-CTFs can drive retention of cholesterol in membrane-bound structures mimicking a cholesterol enriched state (Beel et al., 2010). This state could drive a negative feedback loop whereby high levels of APP or the proteolytic products of amyloidogenic APP processing, Aβ, β-CTFs, and AICD, downregulate intracellular cholesterol uptake, biosynthesis, and turnover(Pierrot et al., 2013). The observation that basal Rab11 is reduced in axons of fAD mutant neurons suggests that a common constitutive recycling/transyctotic

pathway is impaired and raises the possibility that modulating Rab11 activity could also rescue fAD phenotypes.

The observation that the major risk factor for sAD is the E4 allele of APOE, the major brain cholesterol carrier, raises the possibility that lipoprotein transcytosis defects could be a common defect present in multiple fAD and sAD forms. Epidemiologic evidence implicating cholesterol as a major player in AD also dovetails with these molecular and cellular findings (reviewed in Fonseca et al., 2010; Wolozin, 2004). Neurons are dependent on uptake of extracellular cholesterol from lipoprotein particles to perform functions such as axon elongation and synapse formation and maintenance (Barres and Smith, 2001; Lane-Donovan et al., 2014; Mauch et al., 2001; Nägler et al., 2001; Pfrieger, 2003; Pierrot et al., 2013). In fact, glia-derived cholesterol was reported to enhance synaptogenesis of adult rat CNS (Mauch et al., 2001; Nägler et al., 2001) suggesting that a defect in endocytosis and transcytosis of extracellularly-derived cholesterol could have long-term functional consequences leading to impaired neurotransmitter release and synaptic function. Therefore the defects in LDL endocytosis and transcytosis described here for multiple fAD mutations could contribute to a wide array of phenotypes that have been associated with AD. Collectively, the data suggest that modulating cholesterol homeostasis could have protective effects in AD neurons.

6.4 Are βCTFs the Common Driving Factor?

Hidden in the data is the implication that elevation of APP βCTFs might be the relevant factor driving impairments in endocytic sorting and axonal transport, possibly because of differential affinity to motors and/or cholesterol itself. It's possible that βCTFs interact directly with lipoproteins and impair proper sorting of endosomes and cargo by driving defective fusion and fission events, maintaining endosomes in a membrane-bound state, and impairing motor recruitment. Future experiments to ascertain the relationship between βCTFs and motors, βCTFs and cholesterol, and cholesterol and motors will need to be done to fully understand how βCTFs function to drive AD pathology. Importantly, extending investigation to sAD patients will help determine if these phenotypes are common to idiopathic AD as well as inherited fAD.

While several important AD-relevant insights have been garnered from studies of endocytosis in non-polarized cell models, there is little known about the complex sorting pathways afflicted in AD in the polarized cells of interest: neurons. This thesis work sheds light on a number of interesting and unique sorting pathways that may be specifically afflicted in neurons with fAD mutations. Of particular interest are the implications of defective recycling and transcytosis of APP and lipoproteins as well as the evidence for altered axonal transport of a specific subset of axonal cargo. The combined data suggests that fAD (and likely sAD) mutations converge on the common phenotype of impaired axonal delivery of cargo. It further suggests that modulating sorting pathways, possibly

by regulating cholesterol homeostasis or motor activity, can help to alleviate sorting dysfunction and recalibrate the system to a wild-type state.

APPENDIX

Split Channels

%% Program splits channels from an LSM5 file. Mostly useful to identify Map2 files for SomatoDendrite_ROI program.%%

```
dir1 = getDirectory("Choose Source Directory");
dir2 = getDirectory("Choose Green Directory");
dir3 = getDirectory("Choose Red Destination Directory");
dir4 = getDirectory("Choose Map2 Destination Directory");

list = getFileList(dir1);
setBatchMode(true);
for (i=0; i<list.length; i++) {
showProgress(i+1, list.length);
open(dir1+list[i]);
run("Split Channels");
run("Set Scale...", "distance=4.818 known=1 pixel=1 unit=µm global");
selectWindow("C3-"+list[i]);
saveAs("Tiff",dir3+"Gr_"+list[i]);
selectWindow("C2-"+list[i]);
saveAs("Tiff",dir3+"Rd_"+list[i]);
run("Close");
selectWindow("C1-"+list[i]);
saveAs("Tiff",dir4+"Map2_"+list[i]);
run("Close");}
```

SomatoDendrite_ROI

%% This program requires a folder of tif files stained with Map2 or another neuronal cell body marker. It then creates two destination folders. One are the thresholded Map2 images so that you can see what the program is actually counting and how it's processing the Map2 images to a black and white mask. Adjustments can be made by changing the "Subtract background" and/or "setThreshold" settings. The second destination folder is a folder composed entirely of zip files that can be used to measure intensity, count puncta, measure overlaps, etc.%%

```
dir = getDirectory("Choose Map2 Directory");
dir4 = getDirectory("Choose Map2 Mask Directory");
dir5 = getDirectory("Choose Map2 Soma ROI Directory");
list = getFileList(dir);
setBatchMode(true);
for (i=0; i<list.length; i++) {
showProgress(i+1, list.length);
open(dir+list[i]);
run("Set Scale...", "distance=4.818 known=1 pixel=1 unit=µm global");
run("Subtract Background...", "rolling=50");
run("8-bit");
run("Smooth");
setThreshold(15, 255);
run("Convert to Mask");
saveAs("Tiff",dir4+list[i]);
run("Watershed");
run("Analyze Particles...", "size=100-400 circularity=0.00-1.00 show=Nothing
add");
roiManager("Save",dir5+"Soma_"+list[i]+".zip");
selectWindow(list[i]);
run("Close");
setBatchMode(false);
setBatchMode(true);}
```

PunctaInROIAnalysis

%% This program counts puncta in all the ROIs identified by the SomatoDendrite_ROI program. Adjustable settings are bolded and can be modified depending on the stain in question. The output consists of a single summary file with puncta counts per cell as well as a large results file with the areas and intensities of individual puncta. %%

```
run("Set Measurements...", "area mean standard min centroid limit display
redirect=None decimal=4");
dir1 = getDirectory("Choose Source Directory ");
dir2 = getDirectory("Choose Destination Directory ");
list = getFileList(dir1);
dir3 = getDirectory("Choose ROI Directory ");
list2 = getFileList(dir3);
setBatchMode(true);
for (i=0; i<list.length; i++) {
showProgress(i+1, list.length);
open(dir1+list[i]);
selectWindow(list[i]);
run("Set Scale...", "distance=4.818 known=1 pixel=1 unit=µm global");
run("Subtract Background...", "rolling=5");
setMinAndMax(5000, 65535);
run("8-bit");
run("Smooth");
setThreshold(15, 255);
run("Convert to Mask");
run("Watershed");
saveAs("Tiff",dir2+list[i]);
roiManager("Open", dir3+list2[i])
n = roiManager("count");
       for (j=0; j<n; j++)  {
       roiManager("select", j)
run("Analyze Particles...", "size=0.1-100 circularity=0.00-1.00 show=Nothing
summarize add");}
selectWindow(list[i]);
run("Close");
open(dir1+list[i]);
roiManager("Save",dir2+"Puncta_"+list2[i]+".zip");
selectWindow(list[i]);
n = roiManager("count");
       for (j=0; j<n; j++)  {
       roiManager("select", j)
       roiManager("Measure");}
```

```
selectWindow(list[i]);
run("Close");
setBatchMode(false);
setBatchMode(true);}
selectWindow("Summary");
saveAs("Text",dir2+"Puncta_Summary");
selectWindow("Results");
saveAs("Text",dir2+"Puncta_Results");
```

MeasureIntensityinROI_1Ch

%% Measures intensity in ROIs generated from SomatoDendrite_ROI program. Output consists of text files for each image analyzed with individual puncta data summarized. This includes area, mean, standard deviation, min, max intensity. %%

```
run("Set Measurements...", "area mean standard min limit display redirect=None
decimal=4");
dir4 = getDirectory("Choose Channel Directory ");
dir2 = getDirectory("Choose Destination Directory ");
dir3 = getDirectory("Choose ROI Directory ");
list4 = getFileList(dir4);
list2 = getFileList(dir3);
setBatchMode(true);
for (i=0; i<list4.length; i++) {
showProgress(i+1, list4.length);
open(dir4+list4[i]);
run("Set Scale...", "distance=4.818 known=1 pixel=1 unit=µm global");
roiManager("Open", dir3+list2[i]);
selectWindow(list4[i]);
roiManager("Measure");
selectWindow("Results");
saveAs("Text",dir2+list4[i]+"_ROIIntensity");
run("Close");
run("Close");
setBatchMode(false);
setBatchMode(true);}
```

Overlap_counts_in_ROI

%% Counts colocalized puncta from two different stains, channel 1 (Ch1) and channel 2 (Ch2). Adjustable parameters are bolded. Output consists of a text files per image of colocalized puncta counts. To determine percent colocalized, overlap puncta counts can be taken as a ratio from Ch1 puncta and Ch2 puncta (determined in PunctaInROIAnalysis program). %%

```
dir1 = getDirectory("Choose Ch1 Source Directory ");
dir2 = getDirectory("Choose Ch2 Source Directory ");
dir3 = getDirectory("Choose ROI Directory");
list = getFileList(dir1);
list2 = getFileList(dir2);
list3 = getFileList(dir3);
dir5 = getDirectory("Choose Overlap Destination Directory ");
setBatchMode(true);
for (i=0; i<list.length; i++) {
showProgress(i+1, list.length);
open(dir1+list[i]);
selectWindow(list[i]);
run("Set Measurements...", "area mean standard min display redirect=None
decimal=4");
run("Set Scale...", "distance=4.818 known=1 pixel=1 unit=µm global");
selectWindow(list[i]);
run("Subtract Background...", "rolling=10");
run("8-bit");
setThreshold(20, 255);
run("Convert to Mask");
run("Watershed");
run("Fill Holes");
run("Duplicate...", "title=C1");
selectWindow(list[i]);
run("Close");

open(dir2+list2[i]);
selectWindow(list2[i]);
run("Subtract Background...", "rolling=5");
run("8-bit");
setThreshold(15, 255);
run("Convert to Mask");
run("Watershed");
run("Watershed");
run("Duplicate...", "title=C2");
selectWindow(list2[i]);
```

```
run("Close");

imageCalculator("AND create", "C1","C2");
selectWindow("Result of C1");
run("Duplicate...", "title=C1_C2");
roiManager("Open", dir3+list3[i])
n = roiManager("count");
       for (j=0; j<n; j++)  {
       roiManager("select", j)
run("Analyze Particles...", "size=0.1-infinity circularity=0.00-1.00 show=Nothing
exclude summarize");}
selectWindow("Summary");
saveAs("Text",dir5+list3[i]);
run("Close");
selectWindow("C1_C2");
run("Close");
run("Close");
setBatchMode(false);
setBatchMode(true);}
```

ZProject_Stacks

%% Performs a Max intensity projection on all stacks in a folder in order to identify axons with motile vesicles. %%

```
dir = getDirectory("Choose Stack Directory ");
dir2 = getDirectory("Choose Destination Directory ");
list = getFileList(dir);
setBatchMode(true);
for (i=0; i<list.length; i++) {
showProgress(i+1, list.length);
run("TIFF Virtual Stack...");
run("Z Project...", "start=1 stop=121 projection=[Max Intensity]");
saveAs("Tiff",dir2+list[i]);
     close();
 }
 setBatchMode(false);
```

StraightenTransfectedAxons

%% This program requires a folder of videos in a stack format and a folder of roi's that define single axons for straightening. Straightened axons will be saved with the roi name so ensure that the roi name matches the file name. As a cautionary note, if the roi is too close to the edge of an image, an error can occur and the video will not straighten. Simply adjust the roi giving you trouble, save it, and re-run the program if this happens. %%

```
dir1 = getDirectory("Choose Video Directory ");
dir3 = getDirectory("Choose ROI Directory ");
dir4 = getDirectory("Choose Destination Directory ");
list = getFileList(dir1);
list3 = getFileList(dir3);
list4 = getFileList(dir4);
setBatchMode(true);
for (i=0; i<list.length; i++) {
showProgress(i+1, list.length);
open(dir1+list[i]);
roiManager("Open", dir3+list3[i])
n = roiManager("count");
       for (j=0; j<n; j++)  {
       roiManager("select", j)}
selectWindow(list[i]);
run("Straighten...", "line=80 process");
```

```
run("16-bit");
saveAs("Tiff",dir4+list3[i]);
run("Close");
run("Close");
setBatchMode(false);
setBatchMode(true);}
```

Calcium

%% This program requires a directory consisting of videos in stack format with Red (Fura2), Green (Fluo4), and BF images. LSM5 files preferred. The program takes the full video set and uses the Fluo4 staining to generate a Max Intensity Projection, which is then used to identify soma. A max intensity projection is used to account for moving cells in a field

```
run("Set Measurements...", "area mean limit display redirect=None decimal=4");
dir4 = getDirectory("Choose Movie Directory ");
dir2 = getDirectory("Choose Destination Directory ");
dir3 = getDirectory("Choose ROI Directory ");
list4 = getFileList(dir4);
setBatchMode(true);
for (i=0; i<list4.length; i++) {
showProgress(i+1, list4.length);
open(dir4+list4[i]);
run("Set Scale...", "distance=3.103 known=1 pixel=1 unit=µm global");
selectWindow(list4[i]);
run("Split Channels");
selectWindow("C3-"+list4[i]);
run("Close");
selectWindow("C1-"+list4[i]);
run("Duplicate...", "title=Projection duplicate range=1-180");
run("Z Project...", "start=1 stop=180 projection=[Max Intensity]");
selectWindow("MAX_Projection");
run("Subtract Background...", "rolling=50");
run("Smooth");
setThreshold(10, 255);
run("Convert to Mask");
run("Despeckle");
run("Watershed");
run("Analyze Particles...", "size=50-500 circularity=0.00-1.00 show=Nothing
exclude add");
roiManager("Save",dir3+"Soma_"+list4[i]+".zip");
selectWindow("MAX_Projection");
run("Close");
selectWindow("C1-"+list4[i]);
roiManager("Multi Measure");
saveAs("Text",dir2+list4[i]+"_Fluo4");
selectWindow("C2-"+list4[i]);
roiManager("Multi Measure");
selectWindow("Results");
saveAs("Text",dir2+list4[i]+"_Fura2");
run("Close");
```

```
run("Close");
setBatchMode(false);
setBatchMode(true);}
```

MATLAB

```
function Sol_THREE_Density
clc
close all
clear classes

%%%%%%%% SOLS EDIT %%%%%

%%% This program gives the number of puncta
%%% in each channel specified as well as the
%%% axon length of each image.

%%%%%%%%%%%%%%%%%%%%%
%%%%%%%%%%%%%%%%%%%%%
RADIUS=300;
ONETHRES=[179 9e10];
TWOTHRES=[383 9e10];
THREETHRES=[667 9e10];
AMPSCALE=10000;
%%%%%%%%%%%%%%%%%%%%%
GROUP=char('Axons');
%%% FILE CONTAINING X Y DATA %%%%%%%%%%%%%%
ONE=char('GFP2.mat'); %%% SEED Channel
TWO=char('GFP2.mat'); %%% SECOND Channel
THREE=char('GFP2.mat'); %%% THIRD Channel
%%%%%%%%%%%%%%%%%%%%%%%%%%%%%%%%%%%%%%%%%
%%%
%%% ROI MATLAB FILE %%%%%%%%%%%%%%%%%%%%%%%
ROI=char('ROI2.mat'); %ROI File
%%% FILE OUTPUT NAME %%%%%%%%%%%%%%%%%%%%%%
fid=fopen('GFP2_Density.txt', 'wt');
%%%%%%%%%%%%%%%%%%%%%%%%%%%%%%%%%%%%%%%%%
%%%%%%%%%%%%%%%%%%
PXLSCL= 207.5550021;
VAR(1)=RADIUS;
VAR(2:3)=ONETHRES;
VAR(4:5)=TWOTHRES;
VAR(6:7)=THREETHRES;
VAR(8)=AMPSCALE;
VAR(9)=PXLSCL;
Sol_THREE_Density_Program(fid,GROUP,ONE,TWO,THREE,VAR,ROI)
end
```

```
function
Sol_THREE_Density_Program(fid,GROUP,ONE,TWO,THREE,VAR,ROI)
CKLC1=0;
CDHC1=0;
CBOTH=0;
CNONE=0;
CKLCAMP=0;
CDHCAMP=0;
RADIUS=VAR(1);
ONETHRES=VAR(2:3);
TWOTHRES=VAR(4:5);
THREETHRES=VAR(6:7);
AMPSCALE=VAR(8);
PXLSCL=VAR(9);

fprintf(fid,'GROUP_____IMG_ID_____ONE_____TWO_____THRE
E_____ AXL\n');

load(ROI);
for RPT=1:length(RESULT);
   fprintf('Processing IMG %d of %d\n',RPT,length(RESULT))
%%%%%%% AXON LENGTH %%%%%%%%%%%%%%%
       D1 = [x{RPT},y{RPT}];
       S = squareform(pdist(D1));
       d = length(S);
       S = S(1:d-1,2:d);
       AXL = (trace(S)/2000)*PXLSCL;
%%%%%%%%%%%%%%%%%%%%%%%%%%%%%%%%%%%%

   BW=[RESULT{RPT}];
   load(ONE)
   if isempty(movieInfo(RPT).xCoord)
      continue
   else
   MC1=[movieInfo(RPT).xCoord(:,1) movieInfo(RPT).yCoord(:,1)
movieInfo(RPT).amp(:,1)];
   end
%%%%%%% ONE CHANNEL COUNTER %%%%%%
       MCR=round(MC1);
       XYA=0;
       CNT=1;
       for i=1:length(MCR(:,1))
          if BW(MCR(i,2),MCR(i,1))==1
             XYA(CNT,1:3)=MC1(i,1:3);
```

```
            CNT=CNT+1;
        end
    end
    ADAT=XYA;

%%%%%%% TWO CHANNEL COUNTER %%%%%%%

  load(TWO)
  if isempty(movieInfo(RPT).xCoord)
    continue
  else
  MC2=[movieInfo(RPT).xCoord(:,1) movieInfo(RPT).yCoord(:,1)
movieInfo(RPT).amp(:,1)];
  end
  MCR=round(MC2);
    XYB=0;
    CNT=1;
    for i=1:length(MCR(:,1))
      if BW(MCR(i,2),MCR(i,1))==1
        XYB(CNT,1:3)=MC2(i,1:3);
        CNT=CNT+1;
      end
    end
    BDAT=XYB;

%%%%%%% THREE CHANNEL COUNTER %%%%%%%

  load(THREE)
  if isempty(movieInfo(RPT).xCoord)
    continue
  else
  MC3=[movieInfo(RPT).xCoord(:,1) movieInfo(RPT).yCoord(:,1)
movieInfo(RPT).amp(:,1)];
  end
    MCR=round(MC3);
    XYC=0;
    CNT=1;
    for i=1:length(MCR(:,1))
      if BW(MCR(i,2),MCR(i,1))==1
        XYC(CNT,1:3)=MC3(i,1:3);
        CNT=CNT+1;
      end
    end
    CDAT=XYC;
```

```
    ADAT(:,1:2)=PXLSCL*ADAT(:,1:2);
    BDAT(:,1:2)=PXLSCL*BDAT(:,1:2);
    CDAT(:,1:2)=PXLSCL*CDAT(:,1:2);
    ADAT(:,3)=ADAT(:,3)*AMPSCALE;
    BDAT(:,3)=BDAT(:,3)*AMPSCALE;
    CDAT(:,3)=CDAT(:,3)*AMPSCALE;

    ONEEXCLUD=0;
    TWOEXCLUD=0;
    THREEEXCLUD=0;

%%%%%%%%%%%%%%%%%%%%%%%%%%%%%%%%%%%%%%%%%
    for i=1:length(ADAT)
        X=ADAT(i,1);
        Y=ADAT(i,2);
        Z=ADAT(i,3);
        if  Z<=ONETHRES(1) | Z>ONETHRES(2)
            ONEEXCLUD=ONEEXCLUD+1;
        end
    end
    for i=1:length(BDAT)
        BX=BDAT(i,1);
        BY=BDAT(i,2);
        BZ=BDAT(i,3);
        if  BZ<=TWOTHRES(1) | BZ>TWOTHRES(2)
            TWOEXCLUD=TWOEXCLUD+1;
        end
    end
    for i=1:length(CDAT)
        CX=CDAT(i,1);
        CY=CDAT(i,2);
        CZ=CDAT(i,3);
        if  CZ<=THREETHRES(1) | CZ>THREETHRES(2)
            THREEEXCLUD=THREEEXCLUD+1;
        end
    end
 LA=length(ADAT)-ONEEXCLUD;
 LB=length(BDAT)-TWOEXCLUD;
 LC=length(CDAT)-THREEEXCLUD;

 LA=LA/AXL;
 LB=LB/AXL;
 LC=LC/AXL;
```

```
%%% OUTPUT is [IMG ID PRPCNT KLCCNT DHCCNT AXL]
 fprintf(fid,'%10s %10d %10.2f %10.2f %10.2f
%10.2f\n',GROUP,RPT,LA,LB,LC,AXL);


end
fprintf('Done\n')
fclose(fid);

end


function Sol_MakeROIs_v1
clc
close all
clear classes

%%%%%%%%%%%%%%%%%%%%  ROI Generator
%%%%%%%%%%%%%%%%%%%%

%%% This program saves ROI shape in binary form and %%%
%%% x and y position of vertices to facilitate %%%%%%%%
%%% file generation for the colocalization program %%%%


%%% IMAGE FILES %%%%%%%%%%%

FNAME = 'GFP2_%03d.tif';
NS = 001; %First Image Number, must be three digits
NE = 010; %Last Image Number, must be three digits

%%% ROI OUTPUT NAME %%%%%%%%%%%%%%%%%%%%%
fid = 'ROI2.mat';
%%%%%%%%%%%%%%%%%%%%%%%%%%%%%%%%%%%%%%%%%%%%%%%%%%%%%%%%
%%%
Sol_MakeROIs_Program_v1(NS,NE,FNAME,fid);
end
function Sol_MakeROIs_Program_v1(NS,NE,FNAME,fid)
IMAGES=cell(NS,NE);

% Load Images
   for i=NS:NE
      IMAGES{i} = imread(sprintf(FNAME,i));
```

```
    end
RESULT = cell(NS,NE);
    for i=NS:NE;
        [RESULT{i},x{i},y{i}] = roipoly(IMAGES{i});
        save(char(fid),'RESULT','x','y');
        fprintf('Finished IMG %d of %d\n',i,NE)
    end
    fprintf('Done\n')
end

function Sol_THREE_Colocalization_v1
clc
close all
clear classes

%%%%%%%% SOLS EDIT %%%%%

%%%%%%%%%%%%%%%%%%%%%%%%%%% EDIT
%%%%%%%%%%%%%%%%%%%%%%%%%%%%%%%%%
%%%%%%%%%%%%%%%%%%%%%%%%%%
RADIUS=300;
ONETHRES=[0 9e10];
TWOTHRES=[0 9e10];
THREETHRES=[0 9e10];
AMPSCALE=10000;
%%%%%%%%%%%%%%%%%%%%%%%%%%
GROUP=char('Axons');
%%% FILE CONTAINING X Y DATA %%%%%%%%%%%%%%%%
ONE=char('GFP2.mat'); %%% SEED Channel
TWO=char('GFP2.mat'); %%% SECOND Channel
THREE=char('GFP2.mat'); %%% THIRD Channel
%%%%%%%%%%%%%%%%%%%%%%%%%%%%%%%%%%%%%%%%%%%%%%%%%%%
%%%
%%% FILE OUTPUT NAME %%%%%%%%%%%%%%%%%%%%%%%%%%%
fid=fopen('ML_GFP2_Seed.txt','w');    %Seed Channel Data
pid=fopen('PER_GFP2_Seed.txt', 'w');  %Percentage Summary
%%% ROI MATLAB FILE %%%%%%%%%%%%%%%%%%%%%%%%%%%%
ROI=char('ROI2.mat'); %ROI File
%%%%%%%%%%%%%%%%%%%%%%%%%%%%%%%%%%%%%%%%%%%%%%%%%%%
%%%%%%%%%%%%%%%%%%%%%%%%%%%%%%%%%%%%%%%%%
PXLSCL=207.5550021;
VAR(1)=RADIUS;
VAR(2:3)=ONETHRES;
VAR(4:5)=TWOTHRES;
```

```
VAR(6:7)=THREETHRES;
VAR(8)=AMPSCALE;
VAR(9)=PXLSCL;
Sol_THREE_Colocalization_Program(fid,pid,GROUP,ONE,TWO,THREE,VAR,R
OI)
end


function
Sol_THREE_Colocalization_Program(fid,pid,GROUP,ONE,TWO,THREE,VAR,R
OI)
RADIUS=VAR(1);
ONETHRES=VAR(2:3);
TWOTHRES=VAR(4:5);
THREETHRES=VAR(6:7);
AMPSCALE=VAR(8);
PXLSCL=VAR(9);

    P=char(['GROUP___';
        'IMAGE_ID';
        'ADATA(X)';
        'ADATA(Y)';
        'TWO__CNT';
        'THREECNT';
        'BOTH____';
        'NONE____';
        'ONE AMP_'
        'TWO AMP_'
        'THR AMP_']);

    fprintf(fid,'%10s %10s %10s %10s %10s %10s %10s %10s %10s %10s
%10s\n',...
        P(1,:),P(2,:),P(3,:),P(4,:),P(5,:),P(6,:),P(7,:),P(8,:), P(9,:), P(10,:),P(11,:));

    Q=char(['GROUP';
        'IMAGE';
        'TWO__';
        'THREE';
        'BOTH_';
        'NONE_'
        'TOTAL';]);

    fprintf(pid,'%10s %10s %10s %10s %10s %10s %10s\n',...
```

```
        Q(1,:),Q(2,:),Q(3,:),Q(4,:),Q(5,:),Q(6,:),Q(7,:));

load(ROI);
for RPT=1:length(RESULT);
    fprintf('Processing IMG %d of %d\n',RPT,length(RESULT))

%%%%%%%%%%%%%%%%%%%%%%%%%%%%%%%%%%%%%%%%%%%%%%%%%%%%%%%%

    BW=[RESULT{RPT}];
    load(ONE)
    if isempty(movieInfo(RPT).xCoord)
        continue
    else
    MC1=[movieInfo(RPT).xCoord(:,1) movieInfo(RPT).yCoord(:,1)
movieInfo(RPT).amp(:,1)];
    end

%%%%%%% SEED CHANNEL COUNTER %%%%%%%
        MCR=round(MC1);
        XY=0;
        CNT=1;
        for i=1:length(MCR(:,1))
            if BW(MCR(i,2),MCR(i,1))==1
                XY(CNT,1:3)=MC1(i,1:3);
                CNT=CNT+1;
            end
        end
        ADAT=XY;
    ADAT(:,1:2)=PXLSCL*ADAT(:,1:2);
    ADAT(:,3)=ADAT(:,3)*AMPSCALE;

    load(TWO)
    if isempty(movieInfo(RPT).xCoord)
        continue
    else
    MC2=[movieInfo(RPT).xCoord(:,1) movieInfo(RPT).yCoord(:,1)
movieInfo(RPT).amp(:,1)];
    end
    load(THREE)
    if isempty(movieInfo(RPT).xCoord)
        continue
    else
    MC3=[movieInfo(RPT).xCoord(:,1) movieInfo(RPT).yCoord(:,1)
movieInfo(RPT).amp(:,1)];
```

```
    end
    BDAT=MC2(:,1:3);
    CDAT=MC3(:,1:3);

    BDAT(:,1:2)=PXLSCL*BDAT(:,1:2);
    CDAT(:,1:2)=PXLSCL*CDAT(:,1:2);
    BDAT(:,3)=BDAT(:,3)*AMPSCALE;
    CDAT(:,3)=CDAT(:,3)*AMPSCALE;

    %%% OUTPUT is [IMAGE ID, ADATA(X), ADATA(Y), B COUNT, C COUNT,
BOTH
    %%% COUNT, NONE COUNT, A AMP, B AMP, C AMP]

    OUTPUT=zeros(length(ADAT(:,1)));
    OUTPUT(:,1:2)=ADAT(:,1:2)/PXLSCL;
    PRPEXCLUD=0;
    for i=1:length(ADAT)
        X=ADAT(i,1);
        Y=ADAT(i,2);
        Z=ADAT(i,3);

        %%% B COUNTER %%%%%%%%%%%%%%%%%%%%%%%%%%
        BCNT=0;
        for j=1:length(BDAT)
            BX=BDAT(j,1);
            BY=BDAT(j,2);
            BZ=BDAT(j,3);
            BDIST=sqrt((X-BX)^2+(Y-BY)^2);
            if Z>ONETHRES(1) & Z<=ONETHRES(2)
                if BZ>TWOTHRES(1) & BZ<=TWOTHRES(2)
                    if BDIST<=RADIUS
                        BCNT=BCNT+1;
                        OUTPUT(i,8)=BZ;
                    end
                end
            end
        end
        OUTPUT(i,3)=BCNT;

%%%%%%%%%%%%%%%%%%%%%%%%%%%%%%%%%%%%%%%%%%%%%%%%%%%%%%%%

        %%% C COUNTER %%%%%%%%%%%%%%%%%%%%%%%%%%
        CCNT=0;
        for j=1:length(CDAT)
```

```
            CX=CDAT(j,1);
            CY=CDAT(j,2);
            CZ=CDAT(j,3);
            CDIST=sqrt((X-CX)^2+(Y-CY)^2);
            if Z>ONETHRES(1) & Z<=ONETHRES(2)
               if CDIST<=RADIUS
                  if CZ>THREETHRES(1) & CZ<=THREETHRES(2)
                     CCNT=CCNT+1;
                     OUTPUT(i,9)=CZ;
                  end
               end
            end
         end
         OUTPUT(i,4)=CCNT;

%%%%%%%%%%%%%%%%%%%%%%%%%%%%%%%%%%%%%%%

         %%% NONE COUNTER %%%%%%%%%%%%%%%%%%%%%%%%%%%
         if OUTPUT(i,3)>0 & OUTPUT(i,4) >0
            OUTPUT(i,5)=1;
         end
         if OUTPUT(i,3)==0 & OUTPUT(i,4)==0
            OUTPUT(i,6)=1;
         end

%%%%%%%%%%%%%%%%%%%%%%%%%%%%%%%%%%%%%%%
         if  Z<=ONETHRES(1) | Z>ONETHRES(2)
            PRPEXCLUD=PRPEXCLUD+1;
         end
      end


      %%%%%%% START UPDATE WITH APP AMP AFTER NONE
%%%%%%%%

      OUTPUT(:,7)=ADAT(:,3);

      for i=1:length(OUTPUT(:,1))
         fprintf(fid,'%10s %10d %10.4f %10.4f %10d %10d %10d %10d %10.4f
%10.4f %10.4f\n',...
            GROUP, RPT, OUTPUT(i,1), OUTPUT(i,2), OUTPUT(i,3),...
            OUTPUT(i,4), OUTPUT(i,5), OUTPUT(i,6),...
            OUTPUT(i,7), OUTPUT(i,8), OUTPUT(i,9));
      end
```

```
    %%%%%%%% END UPDATE WITH PRP AMP AFTER NONE %%%%%%%%%
    TWOPER=0;
    THREEPER=0;
    KNDPER=0;
    NONEPER=0;
    CNONE=0;
    LA=length(ADAT)-PRPEXCLUD;
    for i=1:length(OUTPUT(:,1))
        if OUTPUT(i,3)>0
            TWOPER=TWOPER+1;
        end
        if OUTPUT(i,4)>0
            THREEPER=THREEPER+1;
        end
        if OUTPUT(i,5)>0
            KNDPER=KNDPER+1;
        end
        if OUTPUT(i,6)>0
            NONEPER=NONEPER+1;
            CNONE=NONEPER-PRPEXCLUD;
        end

    end


    TWOPER=TWOPER/LA*100;
    THREEPER=THREEPER/LA*100;
    KNDPER=KNDPER/LA*100;
    CNONE=CNONE/LA*100;

fprintf(pid,'%10s %10d %10.2f %10.2f %10.2f %10.2f %10d\n',...
   GROUP, RPT, TWOPER, THREEPER, KNDPER, CNONE, LA);

end
fclose(fid);
fclose(pid);

end
```

REFERENCES

Agnello, M., Morici, G., and Rinaldi, A.M. (2008). A method for measuring mitochondrial mass and activity. Cytotechnology 56, 145–149.

Akwasaki Minta, J.P.Y.K. and R.Y.T. (1989). Fluorescent Indicators cytosolic calcium. J. Biol. Chem. *264*, 8171–8178.

Amaratunga, a, Leeman, S.E., Kosik, K.S., and Fine, R.E. (1995). Inhibition of kinesin synthesis in vivo inhibits the rapid transport of representative proteins for three transport vesicle classes into the axon. J. Neurochem. *64*, 2374–2376.

Anderson, E., Maday, S., Sfakianos, J., Hull, M., Winckler, B., Sheff, D., Fölsch, H., and Mellman, I. (2005). Transcytosis of NgCAM in epithelial cells reflects differential signal recognition on the endocytic and secretory pathways. J. Cell Biol. *170*, 595–605.

Anthony, S.M., and Granick, S. (2009). Image Analysis with Rapid and Accurate Two-Dimensional Gaussian Fitting. Langmuir *25*, 8152–8160.

Arpağ, G., Shastry, S., Hancock, W.O., and Tüzel, E. (2014). Transport by populations of fast and slow kinesins uncovers novel family-dependent motor characteristics important for in vivo function. Biophys. J. *107*, 1896–1904.

Ascaño, M., Richmond, A., Borden, P., and Kuruvilla, R. (2009). Axonal targeting of Trk receptors via transcytosis regulates sensitivity to neurotrophin responses. J. Neurosci. *29*, 11674–11685.

Ashford, J.W., and Mortimer, J. a (2002). Non-familial Alzheimer's disease is mainly due to genetic factors. J. Alzheimers. Dis. *4*, 169–177.

Baas, P.W., and Qiang, L. (2005). Neuronal microtubules: when the MAP is the roadblock. Trends Cell Biol. *15*, 183–187.

Balducci, C., and Forloni, G. (2011). App transgenic mice: Their use and limitations. NeuroMolecular Med. *13*, 117–137.

Barres, B. a, and Smith, S.J. (2001). Cation Between Nerve Cells At Meet-Purified Neurons To Form Synaps-. Science (80-.). *294*, 1296–1297.

Von Bartheld, C.S. (2004). Axonal Transport and Neuronal Transcytosis of Trophic Factors, Tracers, and Pathogens. J. Neurobiol. *58*, 295–314.

Beel, A.J., Sakakura, M., Barrett, P.J., and Sanders, C.R. (2010). Direct binding of cholesterol to the amyloid precursor protein: An important interaction in lipid-Alzheimer's disease relationships? Biochim. Biophys. Acta - Mol. Cell Biol. Lipids *1801*, 975–982.

Bentahir, M., Nyabi, O., Verhamme, J., Tolia, A., Horré, K., Wiltfang, J., Esselmann, H., and De Strooper, B. (2006). Presenilin clinical mutations can affect γ-secretase activity by different mechanisms. J. Neurochem. *96*, 732–742.

Bertram, L., and Tanzi, R.E. (2009). Genome-wide association studies in Alzheimer's disease. Hum. Mol. Genet. *18*, 137–145.

Bertram, L., Lill, C.M., and Tanzi, R.E. (2010). The genetics of Alzheimer disease: back to the future. Neuron *68*, 270–281.

Bezprozvanny, I. (2012). Presenilins: A novel link between intracellular calcium signaling and lysosomal function? J. Cell Biol. *198*, 7–10.

Bodovitz, S., and Klein, W.L. (1996). Cholesterol modulates alpha-secretase cleavage of amyloid precursor protein. J. Biol. Chem. *271*, 4436–4440.

Bojarski, L., Herms, J., and Kuznicki, J. (2008). Calcium dysregulation in Alzheimer's disease. Neurochem. Int. *52*, 621–633.

Bornfleth, H., Edelmann, P., Zink, D., Cremer, T., and Cremer, C. (1999). Quantitative motion analysis of subchromosomal foci in living cells using four-dimensional microscopy. Biophys. J. *77*, 2871–2886.

Braidy, N., Muñoz, P., Palacios, A.G., Castellano-Gonzalez, G., Inestrosa, N.C., Chung, R.S., Sachdev, P., and Guillemin, G.J. (2012). Recent rodent models for Alzheimer's disease: Clinical implications and basic research. J. Neural Transm. *119*, 173–195.

Brunholz, S., Sisodia, S., Lorenzo, A., Deyts, C., Kins, S., and Morfini, G. (2012). Axonal transport of APP and the spatial regulation of APP cleavage and function in neuronal cells. Exp. Brain Res. *217*, 353–364.

Bucci, C., Wandinger-Ness, a, Lütcke, a, Chiariello, M., Bruni, C.B., and Zerial, M. (1994). Rab5a is a common component of the apical and basolateral endocytic machinery in polarized epithelial cells. Proc. Natl. Acad. Sci. U. S. A. *91*, 5061–5065.

Buggia-Prévot, V., Fernandez, C.G., Riordan, S., Vetrivel, K.S., Roseman, J., Waters, J., Bindokas, V.P., Vassar, R., and Thinakaran, G. (2014). Axonal

BACE1 dynamics and targeting in hippocampal neurons: a role for Rab11 GTPase. Mol. Neurodegener. *9*, 1.

Burns, M., Gaynor, K., Olm, V., Mercken, M., LaFrancois, J., Wang, L., Mathews, P.M., Noble, W., Matsuoka, Y., and Duff, K. (2003). Presenilin redistribution associated with aberrant cholesterol transport enhances beta-amyloid production in vivo. J. Neurosci. *23*, 5645–5649.

Cai, D., Leem, J.Y., Greenfield, J.P., Wang, P., Kim, B.S., Wang, R., Lopes, K.O., Kim, S.H., Zheng, H., Greengard, P., et al. (2003). Presenilin-1 regulates intracellular trafficking and cell surface delivery of ??-amyloid precursor protein. J. Biol. Chem. *278*, 3446–3454.

Cao, L., Tan, L., Jiang, T., Zhu, X.-C., and Yu, J.-T. (2014). Induced Pluripotent Stem Cells for Disease Modeling and Drug Discovery in Neurodegenerative Diseases. Mol. Neurobiol. 244–255.

Cataldo, A.M., Peterhoff, C.M., Troncoso, J.C., Gomez-Isla, T., Hyman, B.T., and Nixon, R.A. (2000). Endocytic Pathway Abnormalities Precede Amyloid β Deposition in Sporadic Alzheimer's Disease and Down Syndrome. Am. J. Pathol. *157*, 277–286.

Cataldo, A.M., Mathews, P.M., Boiteau, A.B., Hassinger, L.C., Peterhoff, C.M., Jiang, Y., Mullaney, K., Neve, R.L., Gruenberg, J., and Nixon, R.A. (2008). Down syndrome fibroblast model of Alzheimer-related endosome pathology: accelerated endocytosis promotes late endocytic defects. Am. J. Pathol. *173*, 370–384.

Cattaneo, A., and Calissano, P. (2012). Nerve growth factor and Alzheimer's disease: New facts for an old hypothesis. Mol. Neurobiol. *46*, 588–604.

Chang, K.-A., and Suh, Y.-H. (2005). Pathophysiological roles of amyloidogenic carboxy-terminal fragments of the beta-amyloid precursor protein in Alzheimer's disease. J. Pharmacol. Sci. *97*, 461–471.

Chávez-Gutiérrez, L., Bammens, L., Benilova, I., Vandersteen, A., Benurwar, M., Borgers, M., Lismont, S., Zhou, L., Van Cleynenbreugel, S., Esselmann, H., et al. (2012). The mechanism of γ-Secretase dysfunction in familial Alzheimer disease. EMBO J. *31*, 2261–2274.

Cheezum, M.K., Walker, W.F., and Guilford, W.H. (2001). Quantitative comparison of algorithms for tracking single fluorescent particles. Biophys. J. *81*, 2378–2388.

Chevalier-Larsen, E., and Holzbaur, E.L.F. (2006). Axonal transport and neurodegenerative disease. Biochim. Biophys. Acta *1762*, 1094–1108.

Chiba, K., Araseki, M., Nozawa, K., Furukori, K., Araki, Y., Matsushima, T., Nakaya, T., Hata, S., Saito, Y., Uchida, S., et al. (2014). Quantitative analysis of APP axonal transport in neurons: role of JIP1 in enhanced APP anterograde transport. Mol. Biol. Cell *25*, 3569–3580.

Coen, K., Flannagan, R.S., Baron, S., Carraro-Lacroix, L.R., Wang, D., Vermeire, W., Michiels, C., Munck, S., Baert, V., Sugita, S., et al. (2012). Lysosomal calcium homeostasis defects, not proton pump defects, cause endo-lysosomal dysfunction in PSEN-deficient cells. J. Cell Biol. *198*, 23–35.

Coffey, E.E., Beckel, J.M., Laties, A.M., and Mitchell, C.H. (2014). Lysosomal alkalization and dysfunction in human fibroblasts with the Alzheimer's disease-linked presenilin 1 A246E mutation can be reversed with cAMP. Neuroscience *263*, 111–124.

Deinhardt, K., Salinas, S., Verastegui, C., Watson, R., Worth, D., Hanrahan, S., Bucci, C., and Schiavo, G. (2006). Rab5 and Rab7 Control Endocytic Sorting along the Axonal Retrograde Transport Pathway. Neuron *52*, 293–305.

Deng, M., He, W., Tan, Y., Han, H., Hu, X., Xia, K., Zhang, Z., and Yan, R. (2013). Increased expression of reticulon 3 in neurons leads to reduced axonal transport of ?? site amyloid precursor protein-cleaving enzyme. J. Biol. Chem. *288*, 30236–30245.

Denton, K.R., Lei, L., Grenier, J., Rodionov, V., Blackstone, C., and Li, X.J. (2014). Loss of spastin function results in disease-specific axonal defects in human pluripotent stem cell-based models of hereditary spastic paraplegia. Stem Cells *32*, 414–423.

Dingwall, C. (2001). Critical review Spotlight on BACE : The secretases as targets for treatment in Alzheimer disease. Science (80-.). *108*, 1243–1246.

Diwu, Z., Chen, C.-S., Zhang, C., Klaubert, D.H., and Haugland, R.P. (1999). A novel acidotropic pH indicator and its potential application in labeling acidic organelles of live cells. Chem. Biol. *6*, 411–418.

Van den Doel, L.R., Klein, a D., Ellenberger, S.L., Netten, H., Boddeke, F.R., van Vliet, L.J., and Young, I.T. (1998). Quantitative evaluation of light microscopes based on image processing techniques. Bioimaging *6*, 138–149.

Dolma, K., Iacobucci, G.J., Zheng, K.H., Shandilya, J., Toska, E., White, J. a., Spina, E., and Gunawardena, S. (2014). Presenilin influences glycogen synthase

kinase-3 ?? (GSK-3??) for kinesin-1 and dynein function during axonal transport. Hum. Mol. Genet. *23*, 1121–1133.

Domert, J., Rao, S.B., Agholme, L., Brorsson, A.-C., Marcusson, J., Hallbeck, M., and Nath, S. (2014). Spreading of amyloid-β peptides via neuritic cell-to-cell transfer is dependent on insufficient cellular clearance. Neurobiol. Dis. *65*, 82–92.

Dumanchin, C., Czech, C., Campion, D., Cuif, M.H., Poyot, T., Martin, C., Charbonnier, F., Goud, B., Pradier, L., and Frebourg, T. (1999). Presenilins interact with Rab11, a small GTPase involved in the regulation of vesicular transport. Hum. Mol. Genet. *8*, 1263–1269.

Edbauer, D., Winkler, E., Regula, J.T., Pesold, B., Steiner, H., and Haass, C. (2003). Reconstitution of [gamma]-secretase activity. Nat Cell Biol *5*, 486–488.

Encalada, S.E., Szpankowski, L., Xia, C., and Goldstein, L.S.B. (2011). Stable kinesin and dynein assemblies drive the axonal transport of mammalian prion protein vesicles. Cell *144*, 551–565.

Evin, G., and Weidemann, A. (2002). Biogenesis and metabolism of Alzheimer's disease Abeta amyloid peptides. Peptides *23*, 1285–1297.

Fargo, K. and, and Bleiler, L. (2014). Alzheimer's Association Report: 2014 Alzheimers disease facts and figures. Alzheimer's Dement. *10*, e47–e92.

Ferreira, a, Niclas, J., Vale, R.D., Banker, G., and Kosik, K.S. (1992). Suppression of kinesin expression in cultured hippocampal neurons using antisense oligonucleotides. J. Cell Biol. *117*, 595–606.

Fonseca, A.C.R.G., Resende, R., Oliveira, C.R., and Pereira, C.M.F. (2010). Cholesterol and statins in Alzheimer's disease: current controversies. Exp. Neurol. *223*, 282–293.

Fraley, C. (2007). Bayesian Regularization for Normal Mixture Estimation and Model-Based Clustering. *181*, 155–181.

Fu, M., and Holzbaur, E.L.F. (2014). MAPK8IP1/JIP1 regulates the trafficking of autophagosomes in neurons. Autophagy *10*, 2079–2081.

Fu, M.M., and Holzbaur, E.L.F. (2013). JIP1 regulates the directionality of APP axonal transport by coordinating kinesin and dynein motors. J. Cell Biol. *202*, 495–508.

Fu, M.M., Nirschl, J.J., and Holzbaur, E.F. (2014). LC3 Binding to the scaffolding protein jip1 regulates processive dynein-driven transport of autophagosomes. Dev. Cell *29*, 577–590.

Gandy, S., Zhang, Y.W., Ikin, A., Schmidt, S.D., Levy, E., Sheffield, R., Nixon, R. a., Liao, F.F., Mathews, P.M., Xu, H., et al. (2007). Alzheimer's presenilin 1 modulates sorting of APP and its carboxyl-terminal fragments in cerebral neurons in vivo. J. Neurochem. *102*, 619–626.

Gatz, M., Reynolds, C. a, Fratiglioni, L., Johansson, B., Mortimer, J. a, Berg, S., Fiske, A., and Pedersen, N.L. (2006). Role of genes and environments for explaining Alzheimer disease. Arch. Gen. Psychiatry *63*, 168–174.

Geisow, M.J. (1984). Fluorescein conjugates as indicators of subcellular pH. Exp. Cell Res. *150*, 29–35.

Gindhart, J.G., Desai, C.J., Beushausen, S., Zinn, K., and Goldstein, L.S. (1998). Kinesin light chains are essential for axonal transport in Drosophila. J. Cell Biol. *141*, 443–454.

Ginsberg, S.D., Alldred, M.J., Counts, S.E., Cataldo, A.M., Neve, R.L., Jiang, Y., Wuu, J., Chao, M. V, Mufson, E.J., Nixon, R.A., et al. (2010). Microarray analysis of hippocampal CA1 neurons implicates early endosomal dysfunction during Alzheimer's disease progression. Biol. Psychiatry *68*, 885–893.

Golde, T.E., Schneider, L.S., and Koo, E.H. (2011). Anti-aβ therapeutics in Alzheimer's disease: the need for a paradigm shift. Neuron *69*, 203–213.

Goldsbury, C., Baxa, U., Simon, M.N., Steven, A.C., Engel, A., Wall, J.S., Aebi, U., and Müller, S.A. (2011). Amyloid Structure and Assembly: Insights from Scanning Transmission Electron Microscopy. J. Struct. Biol. *173*, 1–13.

Goldstein, L.S.B., and Yang, Z. (2000). M ICROTUBULE -B ASED T RANSPORT S YSTEMS IN N EURONS : The Roles of Kinesins and Dyneins. 39–71.

Goldstein, L.S.B., Reyna, S., and Woodruff, G. (2014). Probing the Secrets of Alzheimer's Disease Using Human-induced Pluripotent Stem Cell Technology. Neurotherapeutics *12*, 121–125.

Goulian, M., and Simon, S.M. (2000). Tracking single proteins within cells. Biophys. J. *79*, 2188–2198.

Gowrishankar, S., Yuan, P., Wu, Y., Schrag, M., Paradise, S., Grutzendler, J., De Camilli, P., and Ferguson, S.M. (2015). Massive accumulation of luminal

protease-deficient axonal lysosomes at Alzheimer's disease amyloid plaques. Proc. Natl. Acad. Sci. 201510329.

Grafstein, B., and Forman, D.S. (1980). Intracellular transport in neurons. Physiol. Rev. *60*, 1167–1283.

Grimm, M.O.W., Grimm, H.S., Tomic, I., Beyreuther, K., Hartmann, T., and Bergmann, C. (2008). Independent inhibition of Alzheimer disease β- and γ-secretase cleavage by lowered cholesterol levels. J. Biol. Chem. *283*, 11302–11311.

Guardia-Laguarta, C., Coma, M., Pera, M., Clarimón, J., Sereno, L., Agulló, J.M., Molina-Porcel, L., Gallardo, E., Deng, A., Berezovska, O., et al. (2010). Mild Cholesterol Depletion Reduces Amyloid-β Production by Impairing APP Trafficking to the Cell Surface. *110*, 220–230.

Gunawardena, S., Yang, G., and Goldstein, L.S.B. (2013). Presenilin controls kinesin-1 and dynein function during APP-vesicle transport in vivo. Hum. Mol. Genet. *22*, 3828–3843.

Guo, Q., Li, H., Gaddam, S.S.K., Justice, N.J., Robertson, C.S., and Zheng, H. (2012). Amyloid precursor protein revisited: Neuron-specific expression and highly stable nature of soluble derivatives. J. Biol. Chem. *287*, 2437–2445.

Hargus, G., Ehrlich, M., Hallmann, A.-L., and Kuhlmann, T. (2014). Human stem cell models of neurodegeneration: a novel approach to study mechanisms of disease development. Acta Neuropathol. *127*, 151–173.

Hart, P.D. (1991). Ammonium chloride, an inhibitor of phagosome-lysosome fusion in macrophages, concurrently induces phagosome-endosome fusion, and opens a novel pathway: studies of a pathogenic mycobacterium and a nonpathogenic yeast. J. Exp. Med. *174*, 881–889.

Hartig, S.M. (2013). Basic image analysis and manipulation in imageJ. Curr. Protoc. Mol. Biol. 1–12.

Hirokawa, N., and Takemura, R. (2005). Molecular motors and mechanisms of directional transport in neurons. Nat. Rev. Neurosci. *6*, 201–214.

Hook, V.Y.H., Toneff, T., Aaron, W., Yasothornsrikul, S., Bundey, R., and Reisine, T. (2002). ??-amyloid peptide in regulated secretory vesicles of chromaffin cells: Evidence for multiple cysteine proteolytic activities in distinct pathways for ??-secretase activity in chromaffin vesicles. J. Neurochem. *81*, 237–256.

Howard, J. (2002). Mechanics of Motor Proteins.

Huckaba, T.M., Gennerich, A., Wilhelm, J.E., Chishti, A.H., and Vale, R.D. (2011). Kinesin-73 is a processive motor that localizes to Rab5-containing organelles. J. Biol. Chem. *286*, 7457–7467.

Inomata, H., Nakamura, Y., Hayakawa, A., Takata, H., Suzuki, T., Miyazawa, K., and Kitamura, N. (2003). A scaffold protein JIP-1b enhances amyloid precursor protein phosphorylation by JNK and its association with kinesin light chain 1. J. Biol. Chem. *278*, 22946–22955.

Inoue, H. (2010). Neurodegenerative disease-specific induced pluripotent stem cell research. Exp. Cell Res. *316*, 2560–2564.

Israel, M. a., Yuan, S.H., Bardy, C., Reyna, S.M., Mu, Y., Herrera, C., Hefferan, M.P., Van Gorp, S., Nazor, K.L., Boscolo, F.S., et al. (2012). Probing sporadic and familial Alzheimer's disease using induced pluripotent stem cells. Nature *482*, 216–220.

Jaqaman, K., Loerke, D., Mettlen, M., Kuwata, H., Grinstein, S., Schmid, S.L., and Danuser, G. (2008). Robust single particle tracking in live cell time-lapse sequences. Nat. Methods *5*, 695–702.

Jin, L.-W., Hua, D.H., Shie, F.-S., Maezawa, I., Sopher, B., and Martin, G.M. (2002). Novel tricyclic pyrone compounds prevent intracellular APP C99-induced cell death. J. Mol. Neurosci. *19*, 57–61.

Jonsson, T., Atwal, J.K., Steinberg, S., Snaedal, J., Jonsson, P. V., Bjornsson, S., Stefansson, H., Sulem, P., Gudbjartsson, D., Maloney, J., et al. (2012). A mutation in APP protects against Alzheimer's disease and age-related cognitive decline. Nature *488*, 96–99.

Kaether, C., Skehel, P., and Dotti, C.G. (2000). Axonal membrane proteins are transported in distinct carriers: a two-color video microscopy study in cultured hippocampal neurons. Mol. Biol. Cell *11*, 1213–1224.

Kamal, A., Stokin, G.B., Yang, Z., Xia, C.-H., and Goldstein, L.S.. (2000). Axonal Transport of Amyloid Precursor Protein Is Mediated by Direct Binding to the Kinesin Light Chain Subunit of Kinesin-I. Neuron *28*, 449–459.

Kang, J.-S., Tian, J.-H., Pan, P.-Y., Zald, P., Li, C., Deng, C., and Sheng, Z.-H. (2008). Docking of axonal mitochondria by syntaphilin controls their mobility and affects short-term facilitation. Cell *132*, 137–148.

Karch, C.M., and Goate, A.M. (2014). Alzheimer's Disease Risk Genes and Mechanisms of Disease Pathogenesis. Biol. Psychiatry *77*, 43–51.

Karten, B., Vance, D.E., Campenot, R.B., and Vance, J.E. (2003). Trafficking of cholesterol from cell bodies to distal axons in Niemann Pick C1-deficient neurons. J. Biol. Chem. *278*, 4168–4175.

Kelly, R.B. (1993). A question of endosomes. Nature *364*, 487–488.

Kim, J., and Sharma, R.P. (2004). Calcium-mediated activation of c-Jun NH2-terminal kinase (JNK and apoptosis in response to cadmium in murine macrophages. Toxicol. Sci. *81*, 518–527.

Kim, S., Sato, Y., Mohan, P.S., Peterhoff, C., Pensalfini, a, Rigoglioso, a, Jiang, Y., and Nixon, R. a (2015). Evidence that the rab5 effector APPL1 mediates APP-βCTF-induced dysfunction of endosomes in Down syndrome and Alzheimer's disease. Mol. Psychiatry 1–10.

King, S.J., and Schroer, T.A. (2000). Dynactin increases the processivity of the cytoplasmic dynein motor. Nat Cell Biol *2*, 20–24.

Kojro, E., Gimpl, G., Lammich, S., Marz, W., and Fahrenholz, F. (2001). Low cholesterol stimulates the nonamyloidogenic pathway by its effect on the alpha - secretase ADAM 10. Proc. Natl. Acad. Sci. U. S. A. *98*, 5815–5820.

Kondo, T., Asai, M., Tsukita, K., Kutoku, Y., Ohsawa, Y., Sunada, Y., Imamura, K., Egawa, N., Yahata, N., Okita, K., et al. (2013). Modeling Alzheimer's disease with iPSCs reveals stress phenotypes associated with intracellular Aβ and differential drug responsiveness. Cell Stem Cell *12*, 487–496.

Koo, E.H., Sisodia, S.S., Archer, D.R., Martin, L.J., Weidemann, a, Beyreuther, K., Fischer, P., Masters, C.L., and Price, D.L. (1990). Precursor of amyloid protein in Alzheimer disease undergoes fast anterograde axonal transport. Proc. Natl. Acad. Sci. U. S. A. *87*, 1561–1565.

Kounnas, M.Z., Moir, R.D., Rebeck, G.W., Bush, A.I., Argraves, W.S., Tanzi, R.E., Hyman, B.T., and Strickland, D.K. (1995). LDL receptor-related protein, a multifunctional ApoE receptor, binds secreted β-amyloid precursor protein and mediates its degradation. Cell *82*, 331–340.

Kubitscheck, U., Kückmann, O., Kues, T., and Peters, R. (2000). Imaging and tracking of single GFP molecules in solution. Biophys. J. *78*, 2170–2179.

Kumar-Singh, S., Theuns, J., Van Broeck, B., Pirici, D., Vennekens, K., Corsmit, E., Cruts, M., Dermaut, B., Wang, R., and Van Broeckhoven, C. (2006). Mean

age-of-onset of familial alzheimer disease caused by presenilin mutations correlates with both increased Aβ42 and decreased Aβ40. Hum. Mutat. *27*, 686–695.

Kyriazis, G. a., Wei, Z., Vandermey, M., Jo, D.G., Xin, O., Mattson, M.P., and Chan, S.L. (2008). Numb endocytic adapter proteins regulate the transport and processing of the amyloid precursor protein in an isoform-dependent manner: Implications for Alzheimer disease pathogenesis. J. Biol. Chem. *283*, 25492–25502.

Laifenfeld, D., Patzek, L.J., McPhie, D.L., Chen, Y., Levites, Y., Cataldo, A.M., and Neve, R.L. (2007). Rab5 mediates an amyloid precursor protein signaling pathway that leads to apoptosis. J. Neurosci. *27*, 7141–7153.

Lane-Donovan, C., Philips, G.T., and Herz, J. (2014). More than cholesterol transporters: lipoprotein receptors in CNS function and neurodegeneration. Neuron *83*, 771–787.

Lazo, O.M., Gonzalez, a., Ascano, M., Kuruvilla, R., Couve, a., and Bronfman, F.C. (2013). BDNF Regulates Rab11-Mediated Recycling Endosome Dynamics to Induce Dendritic Branching. J. Neurosci. *33*, 6112–6122.

Lee, J.-H., Yu, W.H., Kumar, A., Lee, S., Mohan, P.S., Peterhoff, C.M., Wolfe, D.M., Martinez-Vicente, M., Massey, A.C., Sovak, G., et al. (2010). Lysosomal proteolysis and autophagy require presenilin 1 and are disrupted by Alzheimer-related PS1 mutations. Cell *141*, 1146–1158.

Leem, J.Y., Saura, C.A., Pietrzik, C., Christianson, J., Wanamaker, C., King, L.T., Veselits, M.L., Tomita, T., Gasparini, L., Iwatsubo, T., et al. (2002). A Role for Presenilin 1 in Regulating the Delivery of Amyloid Precursor Protein to the Cell Surface. Neurobiol. Dis. *11*, 64–82.

Leifer, B. (2003). Early diagnosis of Alzheimer's disease: clinical and economic benefits. J. Am. Geriatr. Soc. *51*, S281–S288.

Levy, J.R., and Holzbaur, E.L.F. (2006). Cytoplasmic dynein/dynactin function and dysfunction in motor neurons. Int. J. Dev. Neurosci. *24*, 103–111.

Li, K., Yang, L., Zhang, C., Niu, Y., Li, W., and Liu, J.-J. (2014). HPS6 interacts with dynactin p150Glued to mediate retrograde trafficking and maturation of lysosomes. J. Cell Sci. *127*, 4574–4588.

Liu, C.-C., Kanekiyo, T., Xu, H., and Bu, G. (2012). Apolipoprotein E and Alzheimer disease: risk, mechanisms, and therapy. Changes *29*, 997–1003.

Lloyd-Evans, E., Morgan, A.J., He, X., Smith, D. a, Elliot-Smith, E., Sillence, D.J., Churchill, G.C., Schuchman, E.H., Galione, A., and Platt, F.M. (2008). Niemann-Pick disease type C1 is a sphingosine storage disease that causes deregulation of lysosomal calcium. Nat. Med. *14*, 1247–1255.

Lu, D.C., Rabizadeh, S., Chandra, S., Shayya, R.F., Ellerby, L.M., Ye, X., Salvesen, G.S., Koo, E.H., and Bredesen, D.E. (2000). A second cytotoxic proteolytic peptide derived from amyloid beta-protein precursor. Nat. Med. *6*, 397–404.

MacAskill, A.F., and Kittler, J.T. (2010). Control of mitochondrial transport and localization in neurons. Trends Cell Biol. *20*, 102–112.

Maday, S., Wallace, K.E., and Holzbaur, E.L.F. (2012). Autophagosomes initiate distally and mature during transport toward the cell soma in primary neurons. J. Cell Biol. *196*, 407–417.

Mandelkow, E.M., Thies, E., Trinczek, B., Biernat, J., and Mandelkow, E. (2004). MARK/PAR1 kinase is a regulator of microtubule-dependent transport in axons. J. Cell Biol. *167*, 99–110.

Mar, F.M., Simoes, a R., Leite, S., Morgado, M.M., Santos, T.E., Rodrigo, I.S., Teixeira, C. a, Misgeld, T., and Sousa, M.M. (2014). CNS axons globally increase axonal transport after peripheral conditioning. J Neurosci *34*, 5965–5970.

Marquez-Sterling, N.R., Lo, a C., Sisodia, S.S., and Koo, E.H. (1997). Trafficking of cell-surface beta-amyloid precursor protein: evidence that a sorting intermediate participates in synaptic vesicle recycling. J. Neurosci. *17*, 140–151.

Matsuda, S., Matsuda, Y., and D'Adamio, L. (2003). Amyloid β protein precursor (AβPP), but not AβPP-like protein 2, is bridged to the kinesin light chain by the scaffold protein JNK-interacting protein 1. J. Biol. Chem. *278*, 38601–38606.

Mauch, D.H., Nägler, K., Schumacher, S., Göritz, C., Müller, E.C., Otto, a, and Pfrieger, F.W. (2001). CNS synaptogenesis promoted by glia-derived cholesterol. Science *294*, 1354–1357.

Maxfield, F.R. (2014). Role of endosomes and lysosomes in human disease. Cold Spring Harb. Perspect. Biol. *6*.

Mertens, J., Stüber, K., Wunderlich, P., Ladewig, J., Kesavan, J.C., Vandenberghe, R., Vandenbulcke, M., van Damme, P., Walter, J., Brüstle, O., et al. (2013). APP processing in human pluripotent stem cell-derived neurons is

resistant to NSAID-based γ-secretase modulation. Stem Cell Reports *1*, 491–498.

Morel, M., Héraud, C., Nicaise, C., Suain, V., and Brion, J.P. (2012). Levels of kinesin light chain and dynein intermediate chain are reduced in the frontal cortex in Alzheimer's disease: Implications for axoplasmic transport. Acta Neuropathol. *123*, 71–84.

Morris, R.L. (1995). Axonal transport of mitochondria along microtubules and F-actin in living vertebrate neurons. J. Cell Biol. *131*, 1315–1326.

Mostov, K.E., and Simister, N.E. (1985). Transcytosis. Cell *43*, 389–390.

Moughamian, A.J., Osborn, G.E., Lazarus, J.E., Maday, S., and Holzbaur, E.L.F. (2013). Ordered Recruitment of Dynactin to the Microtubule Plus-End is Required for Efficient Initiation of Retrograde Axonal Transport. J. Neurosci. *33*, 13190–13203.

Muresan, Z., and Muresan, V. (2005). Coordinated transport of phosphorylated amyloid-β precursor protein and c-Jun NH(2)-terminal kinase–interacting protein-1. J. Cell Biol. *171*, 615–625.

Muresan, Z., and Muresan, V. (2007). The Amyloid-β Precursor Protein Is Phosphorylated via Distinct Pathways during Differentiation, Mitosis, Stress, and Degeneration. Mol. Biol. Cell *18*, 3835–3844.

Muresan, V., Varvel, N.H., Lamb, B.T., and Muresan, Z. (2009). The cleavage products of amyloid-beta precursor protein are sorted to distinct carrier vesicles that are independently transported within neurites. J. Neurosci. *29*, 3565–3578.

Nägler, K., Mauch, D.H., and Pfrieger, F.W. (2001). Glia-derived signals induce synapse formation in neurones of the rat central nervous system. J. Physiol. *533*, 665–679.

Nangaku, M., Sato-Yoshitake, R., Okada, Y., Noda, Y., Takemura, R., Yamazaki, H., and Hirokawa, N. (1994). KIF1B, a novel microtubule plus end-directed monomeric motor protein for transport of mitochondria. Cell *79*, 1209–1220.

Neely, K.M., and Green, K.N. (2011). Presenilins mediate efficient proteolysis via the autophagosome-lysosome system. Autophagy *7*, 664–665.

Niederst, E., Reyna, S., and Goldstein, L.S.B. (2015). Axonal Amyloid Precursor Protein and its Fragments Undergo Somatodendritic Endocytosis and Processing. Mol. Biol. Cell.

Nixon, R. a (2013). The role of autophagy in neurodegenerative disease. Nat. Med. *19*, 983–997.

Nixon, R. a., and Mcbrayer, M. (2013). Lysosome and Calcium Dysregulation in Alzheimer's disease - Partners in Crime. Biochem Soc Trans *41*, 1495–1502.

Nixon, R.A., and Yang, D.-S. (2011). Autophagy failure in Alzheimer's disease--locating the primary defect. Neurobiol. Dis. *43*, 38–45.

Noble, W., Hanger, D.P., Miller, C.C.J., and Lovestone, S. (2013). The Importance of Tau Phosphorylation for Neurodegenerative Diseases. Front. Neurol. *4*, 83.

Obashi, K., and Okabe, S. (2013). Regulation of mitochondrial dynamics and distribution by synapse position and neuronal activity in the axon. Eur. J. Neurosci. *38*, 2350–2363.

Ohkuma, S., and Poole, B. (1978). Fluorescence probe measurement of the intralysosomal pH in living cells and the perturbation of pH by various agents. Proc. Natl. Acad. Sci. U. S. A. *75*, 3327–3331.

Okada, Y., Yamazaki, H., Sekine-Aizawa, Y., and Hirokawa, N. (1995). The neuron-specific kinesin superfamily protein KIF1A is a uniqye monomeric motor for anterograde axonal transport of synaptic vesicle precursors. Cell *81*, 769–780.

Payne, N.L., Sylvain, A., O'Brien, C., Herszfeld, D., Sun, G., and Bernard, C.C.A. (2015). Application of human induced pluripotent stem cells for modeling and treating neurodegenerative diseases. N. Biotechnol. *32*, 212–228.

Perlson, E., Maday, S., Fu, M.-M., Moughamian, A.J., and Holzbaur, E.L.F. (2010). Retrograde axonal transport: pathways to cell death? Trends Neurosci. *33*, 335–344.

Pfister, K.K., Shah, P.R., Hummerich, H., Russ, A., Cotton, J., Annuar, A.A., King, S.M., and Fisher, E.M.C. (2006). Genetic Analysis of the Cytoplasmic Dynein Subunit Families. PLoS Genet. *2*, e1.

Pfrieger, F.W. (2003). Role of cholesterol in synapse formation and function. Biochim. Biophys. Acta - Biomembr. *1610*, 271–280.

Pierrot, N., Tyteca, D., D'auria, L., Dewachter, I., Gailly, P., Hendrickx, A., Tasiaux, B., Haylani, L. El, Muls, N., N'Kuli, F., et al. (2013). Amyloid precursor protein controls cholesterol turnover needed for neuronal activity. EMBO Mol. Med. *5*, 608–625.

Pietrzik, C.U., Busse, T., Merriam, D.E., Weggen, S., and Koo, E.H. (2002). The cytoplasmic domain of the LDL receptor-related protein regulates multiple steps in APP processing. EMBO J. *21*, 5691–5700.

Power, D., Srinivasan, S., and Gunawardena, S. (2012). In-vivo evidence for the disruption of Rab11 vesicle transport by loss of huntingtin. Neuroreport *23*, 970–977.

Rajendran, L., Honsho, M., Zahn, T.R., Keller, P., Geiger, K.D., Verkade, P., and Simons, K. (2006). Alzheimer's disease beta-amyloid peptides are released in association with exosomes. Proc. Natl. Acad. Sci. U. S. A. *103*, 11172–11177.

Reddy, P.H. (2011). Abnormal Tau, Mitochondrial Dysfunction, Impaired Axonal Transport of Mitochondria, and Synaptic Deprivation in Alzheimer's Disease. Brain Res. *1415*, 136–148.

Reis, G.F., Yang, G., Szpankowski, L., Weaver, C., Shah, S.B., Robinson, J.T., Hays, T.S., Danuser, G., and Goldstein, L.S.B. (2012). Molecular motor function in axonal transport in vivo probed by genetic and computational analysis in Drosophila. Mol. Biol. Cell *23*, 1700–1714.

Rodrigues, E.M., Weissmiller, A.M., and Goldstein, L.S.B. (2012). Enhanced ??-secretase processing alters APP axonal transport and leads to axonal defects. Hum. Mol. Genet. *21*, 4587–4601.

Rosa-Ferreira, C., and Munro, S. (2011). Arl8 and SKIP Act Together to Link Lysosomes to Kinesin-1. Dev. Cell *21*, 1171–1178.

Sakane, H., Yamamoto, H., and Kikuchi, A. (2010). LRP6 is internalized by Dkk1 to suppress its phosphorylation in the lipid raft and is recycled for reuse. J. Cell Sci. *123*, 360–368.

Salehi, A., Delcroix, J.-D., Belichenko, P. V, Zhan, K., Wu, C., Valletta, J.S., Takimoto-Kimura, R., Kleschevnikov, A.M., Sambamurti, K., Chung, P.P., et al. (2006). Increased App expression in a mouse model of Down's syndrome disrupts NGF transport and causes cholinergic neuron degeneration. Neuron *51*, 29–42.

Sanchez-Varo, R., Trujillo-Estrada, L., Sanchez-Mejias, E., Torres, M., Baglietto-Vargas, D., Moreno-Gonzalez, I., De Castro, V., Jimenez, S., Ruano, D., Vizuete, M., et al. (2012). Abnormal accumulation of autophagic vesicles correlates with axonal and synaptic pathology in young Alzheimer's mice hippocampus. Acta Neuropathol. *123*, 53–70.

Saporta, M.A., Dang, V., Volfson, D., Zou, B., Xie, X.S., Adebola, A., Liem, R.K., Shy, M., and Dimos, J.T. (2015). Axonal Charcot-Marie-Tooth disease patient-derived motor neurons demonstrate disease-specific phenotypes including abnormal electrophysiological properties. Exp. Neurol. *263*, 190–199.

Scheinfeld, M.H., Roncarati, R., Vito, P., Lopez, P. a., Abdallah, M., and D'Adamio, L. (2002). Jun NH2-terminal kinase (JNK) interacting protein 1 (JIP1) binds the cytoplasmic domain of the Alzheimer's β-amyloid precursor protein (APP). J. Biol. Chem. *277*, 3767–3775.

Scheuner, D., Eckman, C., Jensen, M., Song, X., Citron, M., Suzuki, N., Bird, T.D., Hardy, J., Hutton, M., Kukull, W., et al. (1996). Secreted amyloid [beta]-protein similar to that in the senile plaques of Alzheimer's disease is increased in vivo by the presenilin 1 and 2 and APP mutations linked to familial Alzheimer's disease. Nat Med *2*, 864–870.

Schon, E.A., and Przedborski, S. (2011). Mitochondria: the next (neurode)generation. Neuron *70*, 1033–1053.

Schroer, T.A. (2004). DYNACTIN. Annu. Rev. Cell Dev. Biol. *20*, 759–779.

Schuster, M., Kilaru, S., Fink, G., Collemare, J., Roger, Y., and Steinberg, G. (2011). Kinesin-3 and dynein cooperate in long-range retrograde endosome motility along a nonuniform microtubule array. Mol. Biol. Cell *22*, 3645–3657.

Scott, C.C., Vacca, F., and Gruenberg, J. (2014). Endosome maturation, transport and functions. Semin. Cell Dev. Biol. *31*, 2–10.

Selfridge, A., Hyun, N., Chiang, C.-C., Reyna, S.M., Weissmiller, A.M., Shi, L.Z., Preece, D., Mobley, W.C., and Berns, M.W. (2015). Rat embryonic hippocampus and induced pluripotent stem cell derived cultured neurons recover from laser-induced subaxotomy. Neurophotonics *2*, 015006.

Shen, D., Wang, X., Li, X., Zhang, X., Yao, Z., Dibble, S., Dong, X., Yu, T., Lieberman, A.P., Showalter, H.D., et al. (2012). Lipid storage disorders block lysosomal trafficking by inhibiting a TRP channel and lysosomal calcium release. Nat Commun *3*, 731.

Sheng, Z.-H. (2014). Mitochondrial trafficking and anchoring in neurons: New insight and implications. J. Cell Biol. *204*, 1087–1098.

Sherrington, R., Rogaev, E.I., Liang, Y., Rogaeva, E. a, Levesque, G., Ikeda, M., Chi, H., Lin, C., Li, G., Holman, K., et al. (1995). Cloning of a gene bearing missense mutations in early-onset familial Alzheimer's disease. Nature *375*, 754–760.

Shi, Y., Kirwan, P., Smith, J., Maclean, G., Orkin, S.H., and Livesey, F.J. (2012). A Human Stem Cell Model of Early Alzheimer ' s Disease Pathology in Down Syndrome A Human Stem Cell Model of Early Alzheimer ' s Disease Pathology in Down Syndrome. *4*.

Shubeita, G.T., Tran, S.L., Xu, J., Vershinin, M., Cermelli, S., Cotton, S.L., Welte, M. a., and Gross, S.P. (2008). Consequences of Motor Copy Number on the Intracellular Transport of Kinesin-1-Driven Lipid Droplets. Cell *135*, 1098–1107.

Simons, M., Ikonen, E., Tienari, P.J., Cid-Arregui, a, Mönning, U., Beyreuther, K., and Dotti, C.G. (1995). Intracellular routing of human amyloid protein precursor: axonal delivery followed by transport to the dendrites. J. Neurosci. Res. *41*, 121–128.

Simons, M., Keller, P., De Strooper, B., Beyreuther, K., Dotti, C.G., and Simons, K. (1998). Cholesterol depletion inhibits the generation of beta-amyloid in hippocampal neurons. Proc. Natl. Acad. Sci. U. S. A. *95*, 6460–6464.

Sinha, S., and Lieberburg, I. (1999). Cellular mechanisms of beta-amyloid production and secretion. Proc. Natl. Acad. Sci. U. S. A. *96*, 11049–11053.

Song, Y., Hustedt, E.J., Brandon, S., and Sanders, C.R. (2013). Competition between homodimerization and cholesterol binding to the C99 domain of the amyloid precursor protein. Biochemistry *52*, 5051–5064.

Spires-Jones, T.L., and Hyman, B.T. (2014). The intersection of amyloid beta and tau at synapses in Alzheimer's disease. Neuron *82*, 756–771.

Sproul, A.A., Jacob, S., Pre, D., Kim, S.H., Nestor, M.W., Navarro-Sobrino, M., Santa-Maria, I., Zimmer, M., Aubry, S., Steele, J.W., et al. (2014). Characterization and Molecular Profiling of PSEN1 Familial Alzheimer's Disease iPSC-Derived Neural Progenitors. PLoS One *9*, e84547.

Stamer, K., Vogel, R., Thies, E., Mandelkow, E., and Mandelkow, E.-M. (2002). Tau blocks traffic of organelles, neurofilaments, and APP vesicles in neurons and enhances oxidative stress. J. Cell Biol. *156*, 1051–1063.

Stamford, A., and Strickland, C. (2013). Inhibitors of BACE for treating Alzheimer's disease: a fragment-based drug discovery story. Curr. Opin. Chem. Biol. *17*, 320–328.

Stein, B.S., and Sussman, H.H. (1986). Demonstration of two distinct transferrin receptor recycling pathways and transferrin-independent receptor internalization in K562 cells. J. Biol. Chem. *261*, 10319–10331.

Steuble, M., Diep, T.-M., Schatzle, P., Ludwig, a., Tagaya, M., Kunz, B., and Sonderegger, P. (2012). Calsyntenin-1 shelters APP from proteolytic processing during anterograde axonal transport. Biol. Open *1*, 761–774.

Stokin, G.B., and Goldstein, L.S.B. (2006a). Linking molecular motors to Alzheimer's disease. J. Physiol. Paris *99*, 193–200.

Stokin, G.B., and Goldstein, L.S.B. (2006b). Axonal transport and Alzheimer's disease. Annu. Rev. Biochem. *75*, 607–627.

Stokin, G.B., Lillo, C., Falzone, T.L., Brusch, R.G., Rockenstein, E., Mount, S.L., Raman, R., Davies, P., Masliah, E., Williams, D.S., et al. (2005). Axonopathy and transport deficits early in the pathogenesis of Alzheimer's disease. Science *307*, 1282–1288.

Stokin, G.B., Almenar-Queralt, A., Gunawardena, S., Rodrigues, E.M., Falzone, T., Kim, J., Lillo, C., Mount, S.L., Roberts, E. a., McGowan, E., et al. (2008). Amyloid precursor protein-induced axonopathies are independent of amyloid-β peptides. Hum. Mol. Genet. *17*, 3474–3486.

Sun, T., Qiao, H., Pan, P.-Y., Chen, Y., and Sheng, Z.-H. (2013). Motile axonal mitochondria contribute to the variability of presynaptic strength. Cell Rep. *4*, 413–419.

Suzuki, T., and Nakaya, T. (2008). Regulation of amyloid ??-protein precursor by phosphorylation and protein interactions. J. Biol. Chem. *283*, 29633–29637.

Svennerholm, L., and Gottfries, C.G. (1994). Membrane lipids, selectively diminished in Alzheimer brains, suggest synapse loss as a primary event in early-onset form (type I) and demyelination in late-onset form (type II). J. Neurochem. *62*, 1039–1047.

Szodorai, A., Kuan, Y.-H., Hunzelmann, S., Engel, U., Sakane, A., Sasaki, T., Takai, Y., Kirsch, J., Müller, U., Beyreuther, K., et al. (2009). APP anterograde transport requires Rab3A GTPase activity for assembly of the transport vesicle. J. Neurosci. *29*, 14534–14544.

Szpankowski, L., Encalada, S.E., and Goldstein, L.S.B. (2012). Subpixel colocalization reveals amyloid precursor protein-dependent kinesin-1 and dynein association with axonal vesicles. Proc. Natl. Acad. Sci. *109*, 8582–8587.

Takahashi, K., Tanabe, K., Ohnuki, M., Narita, M., Ichisaka, T., Tomoda, K., and Yamanaka, S. (2007a). Induction of pluripotent stem cells from adult human fibroblasts by defined factors. Cell *131*, 861–872.

Takahashi, M., Murate, M., Fukuda, M., Satoshi, S.B., Ohta, A., and Kobayashi, T. (2007b). Cholesterol Controls Lipid Endocytosis through Rab11. Mol. Biol. Cell *18*, 2667–2677.

Tamboli, I.Y., Hampel, H., Tien, N.T., Tolksdorf, K., Breiden, B., Mathews, P.M., Saftig, P., Sandhoff, K., and Walter, J. (2011). Sphingolipid storage affects autophagic metabolism of the amyloid precursor protein and promotes Abeta generation. J. Neurosci. *31*, 1837–1849.

Tanaka, Y., Kanai, Y., Okada, Y., Nonaka, S., Takeda, S., Harada, A., and Hirokawa, N. (1998). Targeted Disruption of Mouse Conventional Kinesin Heavy Chain kif5B, Results in Abnormal Perinuclear Clustering of Mitochondria. Cell *93*, 1147–1158.

Tanzi, R.E., and Bertram, L. (2005). Twenty years of the Alzheimer's disease amyloid hypothesis: a genetic perspective. Cell *120*, 545–555.

Tarabal, O., Calderó, J., Lladó, J., Oppenheim, R.W., and Esquerda, J.E. (2001). Long-lasting aberrant tubulovesicular membrane inclusions accumulate in developing motoneurons after a sublethal excitotoxic insult: a possible model for neuronal pathology in neurodegenerative disease. J. Neurosci. *21*, 8072–8081.

Taylor, A.M., Blurton-jones, M., Rhee, S.W., Cribbs, D.H., and Carl, W. (2006). A Microfluidic Culture Platform for CNS Axonal Injury, Regeneration, and Transport. Nat. Methods *2*, 599–605.

Thomann, D., Rines, D.R., Sorger, P.K., and Danuser, G. (2002). Automatic fluorescent tag detection in 3D with super-resolution: application to the analysis of chromosome movement. J. Microsc. *208*, 49–64.

Tienari, P.J., De Strooper, B., Ikonen, E., Simons, M., Weidemann, a, Czech, C., Hartmann, T., Ida, N., Multhaup, G., Masters, C.L., et al. (1996). The beta-amyloid domain is essential for axonal sorting of amyloid precursor protein. EMBO J. *15*, 5218–5229.

Toyn, J.H., and Ahlijanian, M.K. (2014). Interpreting Alzheimer's disease clinical trials in light of the effects on amyloid-β. Alzheimers. Res. Ther. *6*, 14.

Treusch, S., Hamamichi, S., Goodman, J.L., Matlack, K.E.S., Chung, C.Y., Baru, V., Shulman, J.M., Parrado, A., Bevis, B.J., Valastyan, J.S., et al. (2011). Functional Links Between A b Toxicity ,. *334*, 1241–1245.

Udayar, V., Buggia-Prévot, V., Guerreiro, R.L., Siegel, G., Rambabu, N., Soohoo, A.L., Ponnusamy, M., Siegenthaler, B., Bali, J., Simons, M., et al. (2013). A

Paired RNAi and RabGAP overexpression screen identifies Rab11 as a regulator of β-amyloid production. Cell Rep. *5*, 1536–1551.

Ullrich, O., Reinsch, S., Urbé, S., Zerial, M., and Parton, R.G. (1996). Rab11 regulates recycling through the pericentriolar recycling endosome. J. Cell Biol. *135*, 913–924.

Vagnoni, A., Perkinton, M.S., Gray, E.H., Francis, P.T., Noble, W., and Miller, C.C.J. (2012). Calsyntenin-1 mediates axonal transport of the amyloid precursor protein and regulates aβ production. Hum. Mol. Genet. *21*, 2845–2854.

Vassar, R., Kuhn, P.H., Haass, C., Kennedy, M.E., Rajendran, L., Wong, P.C., and Lichtenthaler, S.F. (2014). Function, therapeutic potential and cell biology of BACE proteases: Current status and future prospects. J. Neurochem. *130*, 4–28.

Verdi, J.M., Bashirullah, a, Goldhawk, D.E., Kubu, C.J., Jamali, M., Meakin, S.O., and Lipshitz, H.D. (1999). Distinct human NUMB isoforms regulate differentiation vs. proliferation in the neuronal lineage. Proc. Natl. Acad. Sci. U. S. A. *96*, 10472–10476.

Verhey, K.J., Meyer, D., Deehan, R., Blenis, J., Schnapp, B.J., Rapoport, T. a., and Margolis, B. (2001). Cargo of kinesin identified as JIP scaffolding proteins and associated signaling molecules. J. Cell Biol. *152*, 959–970.

Vincent, L., and Soille, P. (1991). Watersheds in Digital Spaces: An Efficient Algorithm Based on Immersion Simulations. IEEE Trans. Pattern Anal. Mach. Intell. *13*, 583–598.

Wahrle, S., Das, P., Nyborg, A.C., McLendon, C., Shoji, M., Kawarabayashi, T., Younkin, L.H., Younkin, S.G., and Golde, T.E. (2002). Cholesterol-dependent gamma-secretase activity in buoyant cholesterol-rich membrane microdomains. Neurobiol. Dis. *9*, 11–23.

Walter, J., and van Echten-Deckert, G. (2013). Cross-talk of membrane lipids and Alzheimer-related proteins. Mol Neurodegener *8*, 34.

Wang, C.-L., Tang, F.-L., Peng, Y., Shen, C.-Y., Mei, L., and Xiong, W.-C. (2012). VPS35 regulates developing mouse hippocampal neuronal morphogenesis by promoting retrograde trafficking of BACE1. Biol. Open.

Weissmiller, A.M., Natera-Naranjo, O., Reyna, S.M., Pearn, M.L., Zhao, X., Nguyen, P., Cheng, S., Goldstein, L.S.B., Tanzi, R.E., Wagner, S.L., et al. (2015). A γ-Secretase Inhibitor, but Not a γ-Secretase Modulator, Induced Defects in BDNF Axonal Trafficking and Signaling: Evidence for a Role for APP. PLoS One *10*, e0118379.

Welz, T., Wellbourne-Wood, J., and Kerkhoff, E. (2014). Orchestration of cell surface proteins by Rab11. Trends Cell Biol. *24*, 407–415.

Wilson, J.M., de Hoop, M., Zorzi, N., Toh, B.H., Dotti, C.G., and Parton, R.G. (2000). EEA1, a tethering protein of the early sorting endosome, shows a polarized distribution in hippocampal neurons, epithelial cells, and fibroblasts. Mol. Biol. Cell *11*, 2657–2671.

Wisco, D., Anderson, E.D., Chang, M.C., Norden, C., Boiko, T., Fölsch, H., and Winckler, B. (2003). Uncovering multiple axonal targeting pathways in hippocampal neurons. J. Cell Biol. *162*, 1317–1328.

Wolfe, D.M., Lee, J., Kumar, A., Lee, S., Orenstein, S.J., and Nixon, R.A. (2013). Autophagy failure in Alzheimer's disease and the role of defective lysosomal acidification. Eur. J. Neurosci. *37*, 1949–1961.

Wolozin, B. (2004). Cholesterol and the Biology of Alzheimer's Disease. Neuron *41*, 7–10.

Woodruff, G., Young, J.E., Martinez, F.J., Buen, F., Gore, A., Kinaga, J., Li, Z., Yuan, S.H., Zhang, K., and Goldstein, L.S.B. (2013). The Presenilin-1 δE9 Mutation Results in Reduced γ-Secretase Activity, but Not Total Loss of PS1 Function, in Isogenic Human Stem Cells. Cell Rep. *5*, 974–985.

Yagi, T., Ito, D., Okada, Y., Akamatsu, W., Nihei, Y., Yoshizaki, T., Yamanaka, S., Okano, H., and Suzuki, N. (2011). Modeling familial Alzheimer's disease with induced pluripotent stem cells. Hum. Mol. Genet. *20*, 4530–4539.

Yamazaki, H., Nakata, T., Okada, Y., and Hirokawa, N. (1995). KIF3A/B: A heterodimeric kinesin superfamily protein that works as a microtubule plus end-directed motor for membrane organelle transport. J. Cell Biol. *130*, 1387–1399.

Yap, C.C., Wisco, D., Kujala, P., Lasiecka, Z.M., Cannon, J.T., Chang, M.C., Hirling, H., Klumperman, J., and Winckler, B. (2008). The somatodendritic endosomal regulator NEEP21 facilitates axonal targeting of L1/NgCAM. J. Cell Biol. *180*, 827–842.

Ye, X., and Cai, Q. (2014). Snapin-mediated BACE1 retrograde transport is essential for its degradation in lysosomes and regulation of app processing in neurons. Cell Rep. *6*, 24–31.

Yoon, S.Y., Choi, J.E., Yoon, J.H., Huh, J.-W., and Kim, D.H. (2006). BACE inhibitor reduces APP-beta-C-terminal fragment accumulation in axonal swellings of okadaic acid-induced neurodegeneration. Neurobiol. Dis. *22*, 435–444.

Young, J.E., and Goldstein, L.S.B. (2012). Alzheimer's disease in a dish: Promises and challenges of human stem cell models. Hum. Mol. Genet. *21*, 1–8.

Young, J.E., Boulanger-Weill, J., Williams, D.A., Woodruff, G., Buen, F., Revilla, A.C., Herrera, C., Israel, M.A., Yuan, S.H., Edland, S.D., et al. (2015). Elucidating molecular phenotypes caused by the SORL1 Alzheimer's disease genetic risk factor using human induced pluripotent stem cells. Cell Stem Cell *16*, 373–385.

Yuan, S.H., Martin, J., Elia, J., Flippin, J., Paramban, R.I., Hefferan, M.P., Vidal, J.G., Mu, Y., Killian, R.L., Israel, M. a., et al. (2011). Cell-surface marker signatures for the Isolation of neural stem cells, glia and neurons derived from human pluripotent stem cells. PLoS One *6*.

Zhang, X., and Song, W. (2013). The role of APP and BACE1 trafficking in APP processing and amyloid-β generation. Alzheimers. Res. Ther. *5*, 46.

Zhang, M., Haapasalo, A., Kim, D.Y., Ingano, L. a M., Pettingell, W.H., and Kovacs, D.M. (2006). Presenilin/gamma-secretase activity regulates protein clearance from the endocytic recycling compartment. FASEB J. *20*, 1176–1178.

Zhang, Y., Pak, C., Han, Y., Ahlenius, H., Zhang, Z., Chanda, S., Marro, S., Patzke, C., Acuna, C., Covy, J., et al. (2013). Rapid Single-Step Induction of Functional Neurons from Human Pluripotent Stem Cells. Neuron *78*, 785–798.

Zhang, Y., Chen, K., Sloan, S. a, Bennett, M.L., Scholze, A.R., Keeffe, S.O., Phatnani, H.P., Guarnieri, X.P., Caneda, C., Ruderisch, N., et al. (2014). An RNA-Sequencing Transcriptome and Splicing Database of Glia , Neurons , and Vascular Cells of the Cerebral Cortex. *34*, 1–19.